Chemical effects of episodic accretion

Niels Bohr Institute

University of Copenhagen

Written by

Gergely Friss

Supervisor

Jes Kristian Jørgensen

Handed in on

2022-09-28

Abstract

An important problem that molecular astrophysics faces is to understand where, when and how complex organic and prebiotic molecules emerge. To form the basic building blocks of life – for example amino acids or sugars – molecules have to go through many complex chemical reactions between many different species. The origins of these biomolecular precursors are an on-going research field, however observations show that they already arise in star forming regions. Such molecules, including methanol (CH_3OH), methyl formate ($HCOOCH_3$), formamide (NH_2CHO) and other complex organic molecules, are formed through gas- and solid-state chemistry. For instance, methanol is formed from carbon monoxide (CO) on grain surfaces through hydrogenation steps. Keeping CO in the solid state to form more complex species, however, requires a cold environment ($\lesssim$20K). Therefore, temperature and other physical parameters might have an impact on the chemistry in star forming regions. Over the last years a picture has emerged where young stars accrete gas and dust in a highly episodic manner with, e.g., strong bursts of accretion related to the formation of disks and binaries. This may strongly affect the chemistry as the luminosity of the protostar and thus the temperature in the envelope and disk surrounding the young star will vary significantly compared to what one would expect from simple classical infall models. In this project we characterise the chemical effects of a changing environment around a protostar. In our simulations, we couple the chemistry with an underlying physical model of episodic accretion. We explore the significance of, for example, the duration, frequency and magnitude of bursts and the density of the envelope on the formation of chemically interesting molecules. We quantify uncertainty values on the abundances of each species using the uncertainty of the chemical reaction rates and the Monte Carlo method. We find that in case of most species, the effects of episodic accretion on the abundances are beyond the corresponding uncertainties. Comparing our results to observations of various species, one could make assumptions on the history of different protostars and conclude the possible importance of episodic accretion.

Acknowledgement

First and foremost, I would like to thank my thesis supervisor, Jes Kristian Jørgensen for creating and giving me the opportunity to work on such a thrilling project. I am grateful for all the motivation and guidance I have received from him during the last year that kept me pushing further and further and helped me avoid getting lost in sidetracks. He treated me like a colleague and encouraged me to participate in the NBI Student Symposium with a presentation and to join the upcoming Annual Danish Astronomy Meeting for what I am thankful.
I would also like to give my gratitude to the rest of our Starplan group for involving me and treating me as equal. I would like to thank Sacha Gavino for his help with the Pnautilus code and the useful discussions we had to solve issues with the code. I also thank Rebecca Pitts for the amount of knowledge and opinion she shared with me about the KIDA network and that I could be part of the Code&Coffee meetings.
I am thankful to my university friends for going along with me on this journey. I thank Kevin Kumar for his useful opinions on document structuring and plotting, and Vito Tuhtan for his help with HPC and parallelisation.
I am grateful to Tanvi Vyas who comforted me in stressful times and helped improving my thesis by proofreading it. Last but not least, for supporting me and making it possible to pursue a Master degree abroad, I give my gratitude to my family.

Contents

1 Introduction

During the past few decades more than 200 different molecules have been detected in the interstellar space. These observations bear both (bio-)chemical and physical importance. It is assumed that molecules in the interstellar medium (ISM) have a cyclic life (van Dishoeck 2017) that follows the lifecycle of interstellar gas and dust, as illustrated on Figure 1. Atoms are formed inside stars and are released into space upon the death of star. This ejected matter later forms low-density, diffuse clouds in which atoms form bonds and create simple molecules like carbon monoxide (CO). As the density increases, more complex molecules emerge that are important precursors to the building blocks of life. Such a species is, for example, glycolaldehyde ($HCOCH_2OH$), the precursor of ribose that leads to RNA formation (Coutens et al. 2018). We refer to carbon-bearing species that have at least six atoms as complex organic molecules, i.e. COMs (Jørgensen et al. 2020). Though this might not coincide with the standard chemical definition of COMs, it is a general practice in the field of molecular astrophysics. The process of producing more complex species continues as stars and their planetary system are formed inside dense clouds. Consequently, some of the molecules are swallowed by the emerging star (closing the circle of their lives), but other molecules might be incorporated into the material of planets and comets. It is still an ongoing debate whether icy objects like comets carry the (chemical) fingerprint of the time of their formation. However, the composition of comets in our own Solar System show some degree of similarities with protostellar observations (Drozdovskaya et al. 2019).

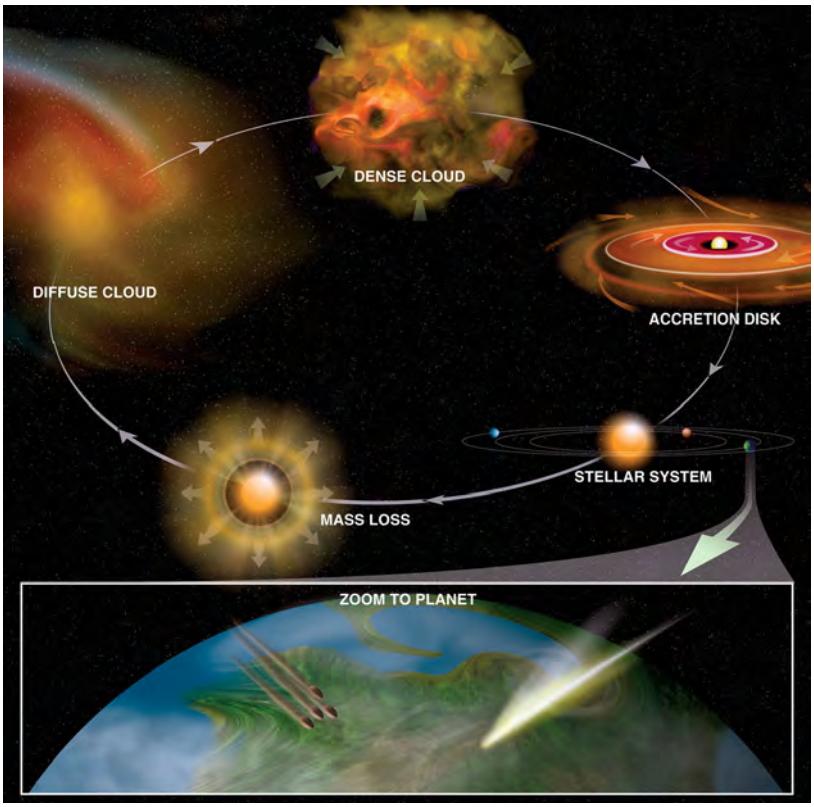

Figure 1: Visual representation of the cyclic life of gas and dust in the interstellar space. Credit: Bill Saxton (NRAO).

There is a significant interplay between the chemistry and the physical environment in the ISM that molecular astrophysics, or astrochemistry, is trying to untangle. The chemistry has an impact on the physical structure as the molecules serve as coolants of the gas by radiating the excess energy. On the other hand, the physical environment can determine what kind of species arise in different regions (van Dishoeck 2017). For example, the presence of certain species may reflect the occurrence of a recent accretion burst or shock wave, or imply the strength of the irradiation field, etc. Species are present in the ISM in two phases: gas and solid phase. Most of the molecules are in the gas phase where they move around freely, colliding with each other and interstellar dust. If the temperature is low enough, upon collision, species will stick to the surface of dust grains and become solid phase species. There are also molecules that form on the grain surfaces (El-Abd et al.

2019; Coutens et al. 2015; Jørgensen et al. 2020; Watanabe et al. 2002). It is possible to observe molecules in both phases according to their rotational (only in the gas phase), vibrational or electronic transitions. However, the required methods differ: gas phase species are studied by their emission lines while solid phase molecules are observed via their absorption lines (Boogert et al. 2015). Due to generally low temperatures, astrochemical observations aim at rotational and vibrational transitions that are located in the sub millimetre (submm)–infra red (IR) regime. Facilities in use are, for example, the Atacama Large Millimetre/submillimetre Array (ALMA), Very Large Telescope (VLT), Submillimeter Array (SMA), Stratospheric Observatory for Infrared Astronomy (SOFIA), Herschel or the recently launched James Webb Space Telescope (JWST), amongst others.

The physics of star formation is still an on-going debate. One of the first theories by Shu (1977) suggest that a newly born protostar gradually accretes material from its surrounding envelope. However, recent observations made by, for example, Kenyon et al. (1990), Evans et al. (2009) and Jørgensen et al. (2015) suggest that this is not the case. A theory that could explain the contradiction between the observations and the predictions made by the simple model of Shu (1977) is episodic accretion. The basis of this theory is that the protostar spends most if its lifetime in a low accretion state that is episodically intercepted by supposedly short accretion burst phases. During these high accretion rate phases, the luminosity of the protostar increases and so does the temperature of the protostellar envelope (and disk) that can potentially alter the chemical reactions in there.

In this thesis we study whether episodic accretion leaves any mark on the chemistry. We aim to identify chemical indicators that could imply the existence of past accretion bursts, for example by their presence or spatial distribution. We do so by running single-point astrochemical simulations in which we couple an episodically changing environment with a chemical network. The outline of this thesis is as follows. In Chapter 2 we give a simplified explanation on star formation. We also summarise the arising issues with star formation theory and how episodic accretion proposes to solve them. Astrochemical processes that can be of help in

unraveling the physical process are also summaries here. Chapters 3 and 4 are dedicated to introduce the simulation software and chemical network used in this project. We also describe here the initial set up of our single-point models. In Chapter 5, we obtain the statistical uncertainty of our chemical network so that we can answer, in Chapter 6, how accretion bursts affect the abundances of various species and which parameters are the most significant. Then, we compare our models with observations in Chapter 7 before extending them with free-fall (Chapter 8). At last, we discuss and conclude our results in Chapter 9.

2 Background

2.1 Star formation and episodic accretion

In order to put this thesis into its physical context, we must understand how stars form. Though it is a complex mechanism that can vary for low- and high-mass stars, the characteristic steps are common and easily understandable (Jørgensen et al. 2020). In this section, we summarise a general and simplified overview on how stars form and what issues arise regarding this simple model. Then we introduce episodic accretion and explain how it addresses the aforementioned caveats.

Stars are formed in the depth of large structures called Giant Molecular Clouds that are mainly composed of molecular gas, making up ∼99% of their mass, and silicate or carbonaceous grains, making up only ∼1% of their mass (Henning 2010). Such molecular clouds usually have masses of $\sim 10^5$ $M_\odot$ and sizes of ∼100 parsecs (Herbst et al. 2009; Neralwar et al. 2022). Molecular clouds break up into long and thin (∼0.1 pc) substructures, called filaments, that represent the first step towards star formation (Ballesteros-Paredes et al. 2020). As gravity contracts parts of the filaments, dense and cold regions emerge that are called dense cores. Such cores are also referred to as prestellar cores and usually have a temperature of $T \approx 10$ K and a Bonnor-Ebert sphere structure (Hartmann 2008). This structure is a centrally concentrated cloud in hydrostatic equilibrium that consists of a homogeneous inner part and an outer part with radially decreasing density that approaches the structure of an isothermal sphere (i.e. $\rho \propto r^{-2}$). The cores must reach certain criteria in order to collapse and form stars. Such criteria, for example, are the Jeans criteria that relates the mass and spatial scales of the core. Satisfying these criteria enables gravity to win against thermal pressure, turbulent motions and magnetic fields (Hartmann 2008) and resulting in the collapse of the core. The concentrated inner region free-falls towards the centre whilst the outer part experiences an inside-out collapse, i.e. matter closer to the centre reaches the centre earlier than matter from higher distances. As the core collapses, the density in the centre increases. Even-

tually, the central dense part becomes opaque to its own infrared radiation. As a consequence, its temperature and pressure increases, slowing down the infalling material. At this stage, this region is referred to as the first hydrostatic core. As the core accumulates more matter, its size stops growing and begins to shrink while its temperature and pressure increases (Stahler et al. 2004). Once the temperature reaches ∼2000 K, instead of increasing the temperate the energy from the infalling matter is used to dissociate molecular hydrogen. Consequently, the core becomes unstable and collapses again resulting in the second hydrostatic core, i.e. the protostar itself (Stahler et al. 2004).

The new born star is deeply embedded in the gas and dust left from the core which structure is called the protostellar envelope. It normally spans $\sim 10^4$ AU in radius and has a radial dependent density profile inherited from the core structure that approaches $\rho \propto r^{-1.5}$ (Hartmann 2008). The temperature also changes radially as the luminosity of the central object introduces a temperature gradient. Close to the star, the density and temperature reach values of 10^{7-8} cm^{-3} and 100 K or above, respectively. Such hot and dense regions are referred to as the hot corino regions that span around 100 AU in size. Due to the high temperature, all species are evaporated from the grain surfaces, leading to a rich gas phase chemistry (van Dishoeck 2017). Protostars in the first $\sim 10^5$ yr of stellar evolution are classified to be Class 0 stars (Evans et al. 2009). As time elapses, the protostar slowly looses its envelope through a gradual accretion mainly onto the protostar (simple infall model by Shu (1977)) or the protostellar disk. The latter one arises due to the conversation of angular momentum of the collapsing cloud (Hartmann 2008). Eventually, the envelope and later the disk disappear leaving behind the star and its planetary system. Planet formation may already start at the earliest stages of stellar evolution as indicated by a few observations (ALMA Partnership et al. 2015; Alves et al. 2020). However, when and how planets are formed is still an on-going research topic. The process of star formation is schematically shown below on Figure 2.

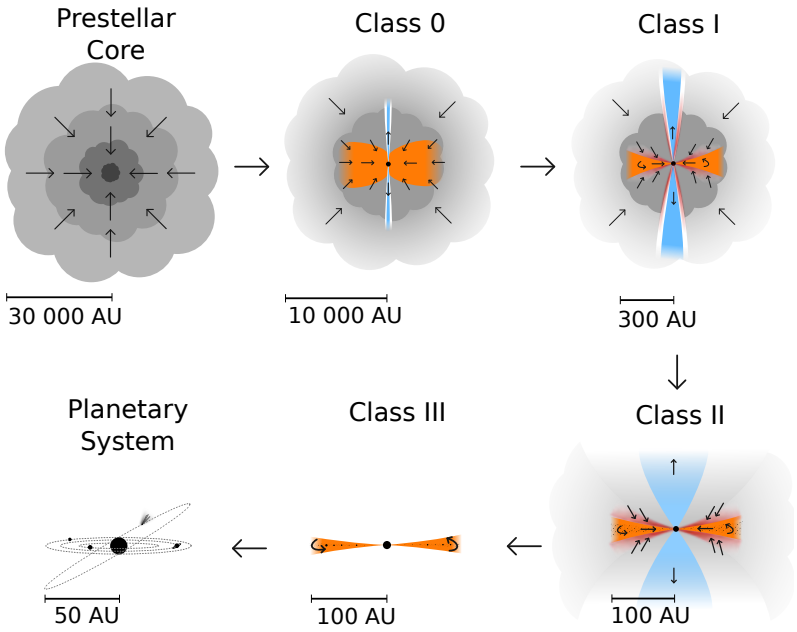

Figure 2: Schematic representation of star and planet formation. Credit: M. V. Persson.

The temperature profile of the protostellar envelope is strongly dependent on the luminosity of the protostar. Accretion is the dominant driver of luminosity during the early stages of stellar evolution until when the temperature of the protostar becomes high enough to start fusing hydrogen, i.e. until the contraction time (Viti et al. 2004). Therefore, it is arguable to take the the total luminosity to be equal to the accretion luminosity, L_{acc}, that is directly proportional to the accretion rate, $\dot{M}$, as written in Equation (1) given by Hartmann (2008). Consequently, accretion is the main physical process that drives the temperature as well.

$$L_{acc} = \frac{GM_*\dot{M}}{R_*} \tag{1}$$

Here G is the gravitational constant, M_* and R_* are the mass and radius of the protostar, respectively. The simple approach is to assume $\dot{M}$ to be constant which implies a constant luminosity and temporally constant temperature profile. However, predictions made upon this simple model have failed to reproduce observations

(Evans et al. 2009; Kenyon et al. 1990) leading to the so called luminosity problem. Evans et al. (2009) showed that most of the observed protostars exhibit lower luminosity values than expected. Besides that, there is also an enormous spread in the observed luminosity distribution that cannot be explained by the simple infall model (Figure 3). The issue is even worse if one considers other sources of luminosity that arise later in the stellar evolution, e.g. deuterium burning or Kelvin-Helmholtz contraction.

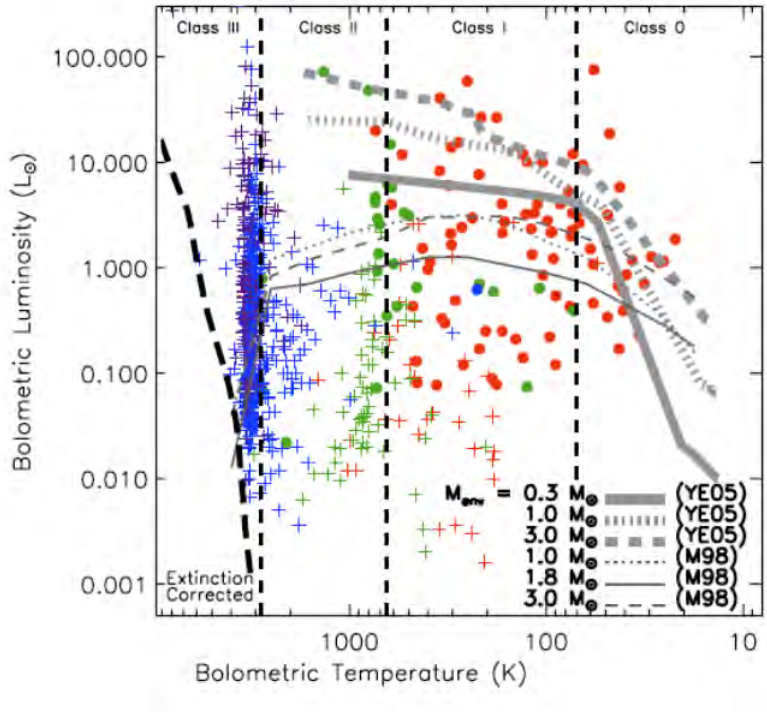

Figure 3: Luminosity problem presented by Evans et al. (2009). Grey lines represent predictions made by simple star formation models. Not only are many stars under-luminous, there is also a wide spread in the luminosity distribution that simple infall models cannot explain.

A plausible explanation could be episodic accretion that has been developed after the ideas by Kenyon et al. (1990). This theory suggests that the protostar exhibits a low accretion rate that is elevated by episodic, short and intensive accretion bursts. The protostar spends most of its lifetime in the so called quiescent phase (i.e. low accretion phase), nevertheless it accretes most of its mass during accretion bursts. During the quiescent phase, the accretion rate is constant and quite low, lower

than what is inferred from the simple model of Shu (1977). This results in low luminosity, hence the problem of under-luminous observations is addressed. However, this might not explain the broad spread in the luminosity distribution due to its simplicity. A working solution is to replace the constant accretion rate with a gradually decreasing one (Frimann et al. 2016). Otherwise one needs to take into account the complexity of star formation and its connection with the surrounding environment (e.g. binarity, other stars and their outflows) to give an answer to why there are such a big variation in the luminosity of protostars.

Another issue present with the simple star formation theory regards snowlines (Frimann et al. 2017; Jørgensen et al. 2015) that are the boundaries between gas and solid phase states of the species. These boundaries are created by the radially decreasing temperature profile of the envelope. Inside the snowline radius, the dust temperatures are high enough to sublimate the species, whereas outside this radius, molecules stick to and stay on the grain surfaces. The evaporation temperature is different for each molecule and therefore so does the snowline radius. A schematic representation can be found on the first panel of Figure 4. As mentioned earlier, the temperature profile is driven by the luminosity of the protostar, therefore the luminosity gives an expected value for the snowline distances for each species. However, many observations – by, for example, Frimann et al. (2017) and Jørgensen et al. (2015) – show disagreements between the measured and expected snowline values. These studies aimed to detect $C^{18}O$ gas in the envelope of Class 0 and I protostars with the SMA and found that $20 - 50\%$ of the sources had extended CO snowline implying that the luminosity of the sources have increased in the past by around $1 - 2$ orders of magnitude. Yet again, the simple infall model cannot give an explanation.

Episodic accretion also gives a viable explanation to the snowline problem that is schematically shown on Figure 4. Let us walk through the example of CO, following Jørgensen et al. (2015). During a low accretion rate phase, the temperature profile creates the CO snowline. If one looks at the CO emission in this phase, one would see a corresponding snowline radius and luminosity. Then, a lumi-

nosity burst happens that results in the heat up of the envelope and thus shifts the CO snowline outwards. The temperature profile follows the luminosity basically instantaneously since it only needs a less than a day to months to adjust (Johnstone et al. 2013) that is negligible compared to the duration of the burst and quiescent phase. This high accretion rate or burst phase is expected to be relatively short, especially compared to the quiescent phase (Johnstone et al. 2013). After this short period, the protostar returns to a quiescent phase with a low accretion rate. Consequently, the envelope cools down and the (expected) snowline radius shrinks. However, the freeze-out process is usually much more slower than the temperature change. The depletion timescale is around 10^4 yr in case of the observed regions by Jørgensen et al. (2015) that had number densities of around 10^6 cm^{-3}. Therefore, CO would remain in the gas phase even in regions with low temperature for a significant amount of time, thus making way for observations with mismatching luminosity and snowline radii. Studies by Jørgensen et al. (2015) and Frimann et al. (2017) suggest that significant accretion bursts (with magnitudes of five or more) happen every $(2-5)\cdot 10^4$ yr. Additionally, Class 0 protostars might experience bursts of smaller magnitudes every few hundreds of years (Zakri et al. 2022).

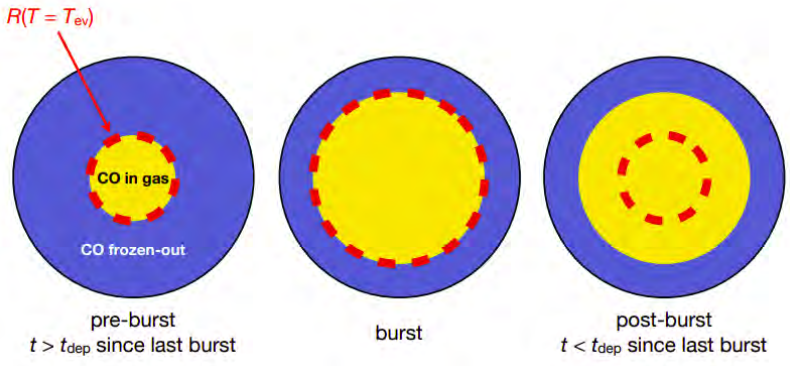

Figure 4: Schematic representation of the effects of periodic accretion on the CO gas and solid phase distribution. A short luminosity burst increases the temperature and shifts the snowline outwards. After the burst, the temperature drops back rather quickly, but the chemistry lags and therefore creates a mismatch between the snowline predicted using the current luminosity and observations. Credit: Jørgensen et al. (2015)

On top of addressing the luminosity and snowline problems, episodic accretion also gives an answer to the observed knots in the outflows of some protostars, since these phenomena are also connected to a varying accretion rate (Arce et al. 2013; Plunkett et al. 2015). Regardless of its effectiveness, the cause of episodic accretion is still under debate. A reasonable solution regards the effects of the emerging disk itself (Jørgensen et al. 2020). The material from the envelope falls onto the disk before the protostar would accrete it. As the disk grows, it develops instabilities, for example viscous-thermal, gravitational or magneto rotational, that lead to episodic accretion by creating huge clumps of material that could be swallowed by the star in short times (Vorobyov et al. 2013). Another reason could be binarity. As the two protostars circles each other they could drag along huge masses of gas and dust that could hit the other star upon their closest approach (Vorobyov et al. 2013). Given that nearly half of the stars are in binary systems (Raghavan et al. 2010) this explanation might be just as viable as the disk instabilities. What more, one could imagine both explanations to be true simultaneously.

2.2 Astrochemistry

The ISM is a harsh environment with many different types of radiation. Therefore the first discovery of molecules in the interstellar space came as a surprise in the late 1930s (McKellar 1940; Swings et al. 1937). To date, already more than 200 species have been observed with many of them towards star forming regions (van Dishoeck 2017). The questions now are rather when and how these different molecules emerge and what interplay the chemistry have with the physical environment. Questions, that astrochemical models have been trying to answer for almost a century. By knowing the chemical network and how it depends on the physical environment and/or its evolution, one is able to use molecules as tracers of the underlying physics. However, getting a complete knowledge on the chemical network is demanding, as the physical characteristics of the ISM (e.g. density, temperature or radiation) are hardly reproducible in laboratories on Earth. Due to these characteristics, chemistry in the ISM is not in thermodynamic equilibrium as

it is on Earth. Two-body reaction are the most significant reactions as the low densities suppress the efficiency of reactions with more reactants (van Dishoeck 1988). Therefore, chemical networks used in studies rely on both experiments and theory and are far from being complete. Nevertheless, on-going network updates contain many useful formation and destruction reactions. A handful of reaction types are proposed to clarify the network of reactions between the numerous molecules. In this section, we summarise the most important mechanisms. Molecules reside in either the gas phase or on the surface of interstellar grains (solid phase). Gas phase reactions could be categorised into three groups: bond forming, bond destructing and bond rearranging mechanisms. First we describe these processes, then we explain how molecules react on the grain surfaces. Finally, we talk about the mechanisms that drive molecules from one phase to the other. We elaborate further on the calculation of the corresponding reaction rates in Section 3.

2.2.1 Gas phase bond formation

The most dominant bond forming process at low temperature is radiative association (van Dishoeck 1988) during which two molecules (A and B) collide and form an intermediate complex that potentially stabilises itself by emitting a photon ($h\nu$):

$$A + B \rightleftharpoons (AB)^* \rightarrow AB + h\nu \tag{2}$$

Another, less efficient mechanism is associative detachment (Chen 1967) during which a negative ion (A^-) collides with a neutral species, resulting in a neutral molecule and and electron (e^-):

$$A^- + B \rightarrow AB + e^- \tag{3}$$

2.2.2 Gas phase bond destruction

In diffuse clouds or at the edges of molecular clouds where the UV radiation from nearby stars (also called as interstellar UV radiation) is high, the most prominent

bond destruction mechanism is photodissociation (Yamamoto 2017):

$$AB + h\nu \rightarrow A + B \tag{4}$$

This process mostly happens directly. The energy of the incoming photon must be above the bond dissociation energy in order to excite the molecule into a dissociative electronic state (van Dishoeck 1988). If the incident photon only excites the molecule into a bound electronic state, dissociation can still happen either without or with photon emission. These are called indirect or spontaneous photodissociation mechanisms, respectively (van Dishoeck 1988). Deeper in clouds, where the UV field is absent, dissociative recombination becomes the dominant bond destruction process for ion molecules:

$$AB^+ + e^- \rightarrow A + B \tag{5}$$

2.2.3 Gas phase bond rearrangement

Two important bond rearranging mechanisms are neutral-neutral and ion-neutral reactions:

$$A + BC \rightarrow AB + C \tag{6}$$

$$A^+ + BC \rightarrow AB^+ + C \tag{7}$$

Ion-molecule reactions might be more important as the long range attraction between the reactants is proportional to R^{-4} that is due to the dipole moment inducing effect of the ion (van Dishoeck 1988). Here, R denotes the distance between the reactants. In comparison, neutral species only attracted to each other by the van der Waals force, that goes with R^{-6} (van Dishoeck 1988). A crucial example for the importance of ion-neutral reactions is the case of H_3^+. This ion is formed from molecular hydrogen due to cosmic ray ionisation. Together with atomic oxygen, it is responsible for the formation of OH^+ that is the backbone of the gas phase formation of water and CO (Yamamoto 2017). Another example could be the for-

mation of NH^+, from N^+ and H_2, as this is the initial step toward more complex, N-bearing species (van Dishoeck 1988).

2.2.4 Grain surface reactions

Even though grains represent a small portion of the interstellar material, they bare a profound importance on the chemistry as the birth place of molecular hydrogen (van Dishoeck 1988) and many COMs, such as methanol or methyl formate (El-Abd et al. 2019; Garrod et al. 2006). The grain acts as a potential third body that absorbs the excess energy released during a reaction (van Dishoeck 1988). There are two leading hypotheses about how surface reactions happen. The Langmuir-Hinshelwood mechanism assumes that both reactants move around on the surface either by thermal hopping or tunneling through potential barriers (Ruaud et al. 2016). The alternative process is the Eley-Rideal mechanism that only requires one of the reactants to be on the surface. The other reactant is in the gas phase that is assumed to hit the already absorbed reactant upon colliding with a grain. Usually, it is neglected due to the low densities, hence low probabilities for a gas molecule to hit an adsorbed one. However, carbon atoms are highly reactive and have a relatively high abundance in the gas-phase, possibly increasing the importance of this mechanism (Ruaud et al. 2015).

Atomic hydrogen is the lightest atom and therefore it is the most mobile on grain surfaces. Besides forming molecular hydrogen, it plays a crucial role in the formation of solid phase water(Yamamoto 2017) which molecule is the main constituent of the ice layer on the grain surfaces. Through hydrogen addition and subtraction reactions, it is also responsible for producing radicals that eventually lead to COMs, e.g. methanol (Chuang et al. 2018; Watanabe et al. 2002; Yamamoto 2017).

2.2.5 Gas-grain reactions

The term gas-grain reactions refers to accretion onto grain surfaces (i.e. freeze-out) and different types of desorption mechanisms. It is assumed that only neutral

species stick to the grains (Wakelam et al. 2012), therefore the mechanisms discussed in this section only involve neutral reactants. The transition from gas to solid phase is a fairly simple process that is called freeze-out. This process needs a cold enough temperature to happen. This temperature varies from species to species according to the strength of their bond with the surface, i.e. stronger bond means that the given species can freeze-out at higher temperatures. This bond can be either chemical, in this case we talk about chemisorption, or physical, in this case we talk about physisorption. The former one is stronger as the molecule that freezes-out establishes some kind of chemical bond with the molecules that are already on the surface while physisorped molecules are only kept on the surface by the weaker van der Waals force (Yamamoto 2017).

There are various processes that drive the species off of the grain surfaces. We distinguish between thermal- and non-thermal desorption mechanisms. Thermal desorption is the exact opposite of freeze-out, e.g. when the temperature of the grain exceeds the freeze-out/evaporation temperature of a species it sublimates. It is well studied both experimentally – by temperature programmed desorption (TPD) experiments – and theoretically (Ferrero et al. 2020). Desorption is still possible even when the dust temperature is too low to allow thermal desorption (Ruaud et al. 2016; Yamamoto 2017). These non-thermal desorption process require some kind of an event that produces enough energy to liberate molecules from the surface. External events are considered to be cosmic rays (CRs) and UV radiation (either CR induced or an external radiation field by, e.g., a nearby star) or sputtering. Sputtering happens when the gas phase molecules collide with grains and have high kinetic energies that could drive molecules off of the surface. This desorption mechanism is characteristic of shocked regions (van Dishoeck 2017). Chemical reactions on the surface could also provide enough excess energy, sublimating the product(s) of the reaction (Yamamoto 2017).

3 The Pnautilus code

Pnautilus is a massive and useful software that has been developed at the Laboratoire d'astrophysique de Bordeaux (Ruaud et al. 2016). It is a gas-grain astrochemical code, i.e. it treats reactions in the gas and solid phases along with processes between the two phases. Chemistry in the ISM is not in equilibrium, therefore reactions are described by differential equations. To put it simply, the change in the density of species i (n_i) is determined by the overall production ($R_{i,p}$) and destruction ($R_{i,d}$) rates:

$$\begin{aligned} \frac{dn_i}{dt} &= R_{i,p} - R_{i,d} = \\ &= \sum_p (k_{i,p} n + \sum_j k_{ij,p} n_i n_j) - \sum_d (k_{i,d} n_i + \sum_j k_{ij,d} n_i n_j) \end{aligned} \tag{8}$$

Here, we distinguish between unimolecular (one reactant) and bimolecular (two reactants) reactions by using i and ij in the subscripts, respectively. The reaction rates are calculated by multiplying the corresponding rate coefficient (k) with the number density of the reactants. We elaborate on how the various rate coefficients are computed later in this chapter.

As each species has its own differential equation on needs to solve a set of differential equations simultaneously. Given the initial conditions, Pnautilus achieves this task. The code gives the opportunity to define an underlying physical environment with many parameters such as density, temperature, visual extinction, cosmic ray ionisation rate, UV irradiation, etc. Thus, one could follow the chemistry during star formation after retrieving these physical parameters from magneto-hydrodynamical (MHD) simulations. Our approach to unravel the effects of episodic accretion is a somewhat different. We use an average protostellar envelope environment but with changing temperature as a result of accretion bursts (detailed later in Section 4.3). Furthermore, as an update to the original version, it is possible to use two solid phases on the grain surfaces, rather than one. The thinner and outer (in the physical sense) layer is the so called surface layer where freeze-out

and evaporation take place. Here the species can move relatively fast. The thicker and deeper layer is called the mantle in which the species move slower and that functions mainly as a reservoir. We briefly study the importance of such a choice in Section 6.1.

3.1 Gas phase reactions

First, we discuss unimolecular reactions that result in ionisation or dissociation. Such reactions are cosmic ray ionisation and dissociation, secondary ionisation induced by cosmic rays and UV photoprocesses. The rate coefficients are calculated as follows (Wakelam et al. 2012):

$$k_{CR} = \alpha_i \zeta \tag{9}$$

for CR ionisation/dissociation,

$$k_{CRP} = \frac{\alpha}{1-\omega} \frac{n(H_2)}{(n(H) + 2n(H_2)} \zeta_{H_2} \tag{10}$$

for secondary ionisation/dissociation induced by cosmic rays and

$$k_{photo} = \alpha e^{-\gamma A_V} \tag{11}$$

for photoprocesses by UV radiation. α and γ are parameters, ζ denotes the cosmic ray flux, ζ_{H_2} is the total H_2 ionisation rate, $\omega = 0.5$ is an average albedo of the grains in the far-ultraviolet (FUV) and A_V is the visual extinction.

In case of bimolecular reaction, the units of the coefficients for these types are cm^3s^{-1} so they are multiplied by the number densities of the reactants (with units cm^{-3} again) in order to get the reaction rates. Rate coefficient are most often calculated by using the Arrhenius-type formula (McElroy et al. 2013):

$$k_{Arr} = \alpha \left(\frac{T}{300K}\right)^{\beta} e^{-\gamma/T} \tag{12}$$

Here, β is a parameter similar to α and γ. In case of ion-neutral reactions the following equations could be used for low and high temperatures, respectively (Wakelam et al. 2012):

$$k_{ionpol,low} = \alpha\beta(0.62 + 0.4767\gamma(300/T)^{0.5}) \tag{13}$$

$$k_{ionpol,high} = \alpha\beta\left(1 + 0.0967\gamma\left(\frac{300}{T}\right)^{0.5} + \frac{\gamma^2}{10526}\frac{300}{T}\right) \tag{14}$$

3.2 Solid phase reactions

The grain surface reaction coefficients are obtained assuming either Langmuir-Hinshelwood or the Eley-Rideal mechanism. Both mechanisms describe bimolecular reactions, thus the reaction rate coefficients have to be multiplied by the reactants' densities to get the reaction rates. In the case of the Langmuir-Hinshelwood mechanism, the rate coefficient ($k_{LH,ij}$) between species i and j is calculated as follows (Ruaud et al. 2016):

$$k_{LH,ij} = \alpha e^{-E_a/T_d}(R_{diff,i} + R_{diff,j})\frac{1}{N_s n_d} \tag{15}$$

Here, E_a is the activation energy of the reaction, T_d is the temperature of the dust particle (i.e. grain), $R_{diff,i}$ is the diffusion rate of the species i, N_s is the number of sites on the surface of a grain and n_d is the number density of the dust grains. There are reactions without an activation energy which means that the exponential becomes one. The diffusion rate is the inverse of the thermal hopping or diffusion time and it is calculated using the vibrational frequency (ν_i) and the diffusion energy barrier ($E_{D,i}$) of the given solid phase species (Ruaud et al. 2016):

$$R_{diff,i} = \nu_i e^{-E_{D_i}/T_d} \tag{16}$$

$$\nu_i = \sqrt{\frac{2n_s E_{D,i}}{\pi^2 m_i}} \tag{17}$$

where n_s is the surface site density of the grain and m_i is the mass of the molecule.

The rate coefficient between species i and j during the Eley-Rideal mechanism, with species j being in the gas phase, is as follows (Ruaud et al. 2015):

$$k_{ER,ij} = \frac{\sigma_d \langle v_j \rangle n_d}{n_s} \tag{18}$$

where σ_d is the cross-section of the grain and $\langle v_j \rangle$ is the thermal velocity of the gas phase species.

3.3 Gas-grain reactions

Freeze-out can only happen when a molecule hits a grain and the temperature is low enough so that the molecule can stick to the surface. Therefore, the accretion rate depends on the number density of the dust grains and the given gas phase molecule (n_i) as well as on the temperature of the gas. Consequently, the rate coefficient is (Reboussin et al. 2014)

$$k_{acc} = \sigma_d \langle v_j \rangle n_d \tag{19}$$

The desorption mechanism can be driven by various effects as summarised earlier. We distinguish between thermal (denoted by T), cosmic ray induced (CR), UV induced and chemical desorption (ch). Furthermore, the UV induced desorption is driven by either external or cosmic ray induced UV radiation (labeled with UV or UV-CR, respectively). The corresponding rate coefficients can be calculated as

(Ruaud et al. 2016; Wakelam et al. 2012)

$$k_{T,i} = \nu_i e^{-E_{b,i}/T_d} \tag{20}$$

$$k_{CR,i} = \frac{\zeta}{1.3 \cdot 10^{-17}\mathrm{s}^{-1}} \nu_i R_{Fe-ion} t_{CR} e^{-E_{b,i}/T_{CR}} \approx \frac{\zeta}{1.3 \cdot 10^{-17}\mathrm{s}^{-1}} \nu_i 3.16 \cdot 10^{-19} \tag{21}$$

$$k_{UV} = \frac{F_{UV} S_{UV} Y_{pd}}{n_s} e^{-2A_V} \tag{22}$$

$$k_{UV-CR} = \frac{F_{UV-CR} S_{UV-CR} Y_{pd}}{n_s} \tag{23}$$

Here, E_b is the binding energy of the species i, $R_{Fe-ion} = 3 \cdot 10^{-14}$ s^{-1} is the standard iron ionisation rate, $T_{CR} = 70$ K and $t_{CR} = 10^{-5}$ s are respectively the increased temperature of the dust upon collision with a cosmic ray and the duration of this elevated temperature. F_{UV} and F_{UV-CR} are the strength of the UV and cosmic ray induced UV radiation while S_{UV} and S_{UV-CR} are the corresponding scaling factors. It is assumed that $F_{UV} = 1 \cdot 10^8$ photons cm^{-2} s^{-1} and $F_{UV} = 1 \cdot 10^4$ photons cm^{-2} s^{-1} and that the chemical desorption is set to have 1% efficiency.

4 Choosing the database for chemical reactions

Pnautilus in itself is not enough to run chemical simulations. It requires a data set that contains all information on the reactions. In this chapter, we compare two online chemical data sets, namely the KInetic Database for Astrochemistry (KIDA) and the chemical database of the University of Manchester Institute of Science and Technology (UMIST). Both databases hold information about the reaction rate coefficients in the form of three parameters: α, β and γ. They also mark the temperature range that these parameters are valid in. Different networks usually differ in their approach of obtaining the included reactions and their reaction rates. For example they might consider different temperature regimes for the same reactions. Therefore, it is important to understand the different networks in order to choose one that contains more relevant information for the study. Naturally, none of the databases are without uncertainties. The magnitude and effect of uncertainties on the simulated abundances of the eventually chosen database is discussed in Chapter 5.

4.1 KIDA

The KInetac Databese for Astrochemistry has been created in order to develop a unique and critical astrochemical database (Wakelam et al. 2012). It aims to gather the most up-to-date and precise reaction rates from other chemical networks and its users. Everyone is allowed to upload new information (for example new reactions or reaction rates) to the network website. These suggestions are carefully being evaluated by the creators and are assigned with different status (e.g. from not recommended to recommended) so that other users can decide whether to use them or not. KIDA is a gas-grain chemical network that overall consists of 10913 reactions between 489 species[1] that are made up from 13 elements. Pnautilus has KIDA implemented by default. The version it uses is from 2016. There are several

[1]Including the ice counterparts of neutral and some additional species the latter number is 962.

reaction types that are included in this network (Ruaud et al. 2016; Wakelam et al. 2012):

1. direct cosmic ray processes
2. photoprocesses
3. neutral-neutral reactions
4. charge exchange reactions
5. radiative association
6. associative detachment
7. electronic recombination and attachment
8. grain surface reactions
9. freeze-out onto and evaporation from dust grains

The first two categories in the list above are unimolecular reactions that result in ionisation or dissociation. Categories 3.-8. consist of bimolecular reactions, i.e. reactions with two reactants. This data set uses the Arrhenius type along with the ion-neutral formulas (Equations (13) and (14)) when needed. The grain surface reaction coefficients are obtained by the Langmuir-Hinshelwood (Ruaud et al. 2016) or the Eley-Rideal (Ruaud et al. 2015) mechanism. Category 9. contains all mechanisms that drive molecules from the gas phase into the solid phase and *vica versa*.

4.2 UMIST

The UMIST database, originally created by Tom Millar in 1991, aims to describe the gas phase chemistry as precisely as possible (McElroy et al. 2013). Grain surface chemistry is left out as the creators argue that the uncertainty of grain surface chemistry prevents the development of a quantitatively accurate model of it.

There is, however, additional information available about the binding energies of the species so the user could expanded the database with freeze-out and evaporation processes. It has 6173 reactions between 467 species that are made up from 13 elements (McElroy et al. 2013). It contains the same types of gas-phase reactions as KIDA and uses the same equations for photoprocesses. However, this database only relies on the Arrhenius-type formula to compute the bimolecular reaction rates.

4.3 Comparison

Visser et al. (2012) studied the effects of episodic accretion around embedded, low-mass protostars. They made single-point, i.e. 0D, chemical simulations of the envelope of an episodically accreting protostar. In this section, we first describe their physical model that we will also implement in our own simulations. Then, we compare the previously described chemical databases using the results of Visser et al. (2012) and ours.

Visser et al. (2012) assumed a protostellar envelope with a total mass of $1 M_{\odot}$, a power-law radial density profile with an exponent of -1.5 and a radial span from 20 AU to 10000 AU. They studied the chemistry at three different radii: 150 AU, 710 AU and 3300 AU that correspond to a molecular hydrogen number density of $n = 10^5$, 10^6 and 10^7 cm^{-3}, respectively. The gas to dust ratio was set to be a 100 and the dust size were chosen to be the average 0.1 μm. Gas and dust temperatures were assumed to be coupled and were 10 K during the quiescent phases and 30 K during accretion bursts, simulating the heating effect of the increased luminosity of the protostar. The temperature increase was considered instantaneous as the gas adjusts to the luminosity on a neglectable timescale (Draine 2003). Other important parameters of episodic accretion are the duration of burst and quiescent phases. The authors chose the burst phase to be 100 yr long in all simulation, whereas they varied the quiescent phase to be $\tau_q = 10^3$ yr or 10^4 yr long. The duration of the quiescent phase determines how much time there is for the molecules to freeze-

out onto the grain surfaces. Furthermore, the cosmic ray ionisation rate was set to $5 \cdot 10^{-17}$ s^{-1}. They did not include any information on the visual extinction, so we set it to be $A_V = 15$ mag.

The chemical database Visser et al. (2012) used was the UMIST database from 2006, namely UDfA06, which they had extended with freeze-out and thermal evaporation processes of neutral species. The initial abundances of the species were chosen as follows: all hydrogen was in H_2; carbon was in gas phase CO (80%), solid phase CO (10%) and solid phase CO_2 (10%); nitrogen was in atomic form (60%), gas phase N_2 (20%), solid phase N_2 (10%) and solid phase NH_3 (10%). Other elemental abundances relative to H_2 are listed in Table 1. They implemented three different, but constant freeze-out rates for CO and N_2 for the three different total gas density simulations.

Table 1: Summary of the initial elemental abundances relative to H_2 used by Visser et al. (2012). Fluorine is additional in our models with a relative abundance given by Ruaud et al. (2016).

	n(X)/N(H_2)
He	$9.71 \cdot 10^{-1}$
S^+	$9.14 \cdot 10^{-8}$
Si^+	$2.74 \cdot 10^{-9}$
Fe^+	$2.74 \cdot 10^{-9}$
Na^+	$2.25 \cdot 10^{-9}$
Mg^+	$1.09 \cdot 10^{-8}$
P^+	$2.16 \cdot 10^{-10}$
Cl^+	$1.0 \cdot 10^{-9}$
F	$6.68 \cdot 10^{-9}$

Their result can be seen on the top panel of Figure 5. In case of low densities and/or short quiescent phases, i.e. figures a), b) and d), the abundances hardly change. This is due to the freeze-out timescale being much longer than the quiescent phase, hence CO and N_2 do not deplete significantly. However, when the freeze-out timescale is comparable to the quiescent phase duration, CO and N_2 abundances fluctuate. This can be seen most prominently on figure f) where the

two timescales are the same. What we see here is actually the shift in the snow-line as CO and N_2 should be frozen out at such a low temperature, but they get released into the gas phase upon every burst. The abundances of CO and N_2 play a significant role in how the abundances of the three other species discussed here change. H_3^+ is the most sensitive towards CO. The reaction of the two said species results in H_2 and HCO^+ which is the main production pathway of HCO^+. H_3^+ is also (solely) responsible for the creation of N_2H^+ by reacting with N_2. A sudden increase in both CO and N_2 abundances depletes the H_3^+, and increases the abundance of HCO^+ and N_2H^+. This scenario happens upon every burst. We intend to reproduce their simulations with both databases of our choice.

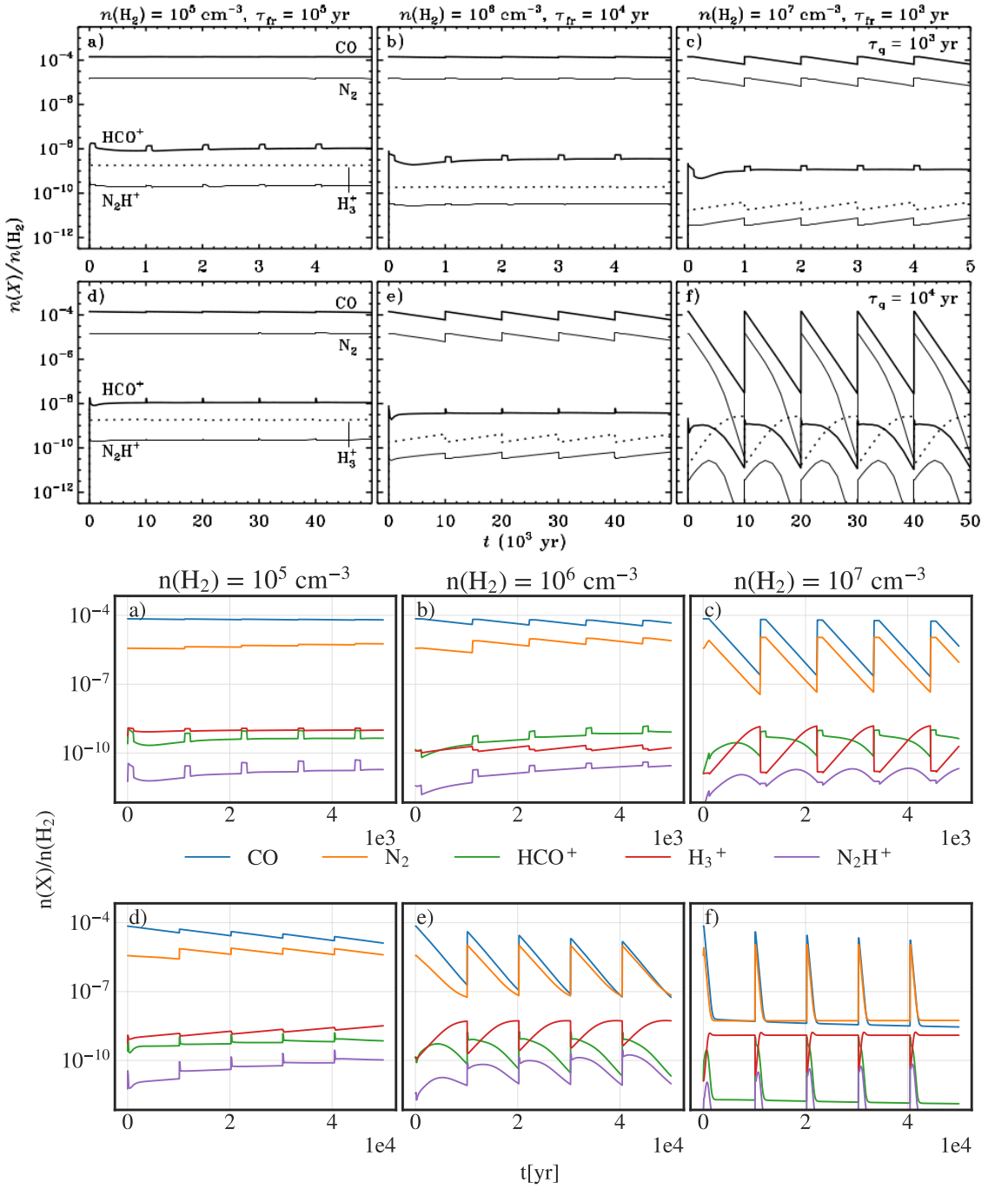

Figure 5: Results of simulating the chemistry around an episodically accreting protostar. **Top:** figure by Visser et al. (2012) showing that the bursts alter the chemistry and even though the physical temperature adjusts to the luminosity in a negligibly short time (Draine 2003) the chemical temperature lags. **Bottom:** Our results using the KIDA database (Wakelam et al. 2012). Similar effects are present as above. The differences are due to the different chemical networks and freeze-out timescales.

As mentioned earlier, KIDA contains grain-surface chemistry in opposition with UMIST. We aim to test how significant this difference is. However, due to incompatibility reasons, we cannot run the simulations using the UMIST database, therefore we make a rather qualitative than quantitative comparison between the results of Visser et al. (2012) and ours. The effects of episodic accretion is clearly visible with both databases, however they already become more prominent for lower densities in our simulations (bottom panel of Figure 5). In our case, only the first one, figure a), with $n = 10^5$ cm^{-3} and $\tau_q = 10^3$ yr has not any significant effects. On the other hand, the simulations of Visser et al. (2012) only show this behaviour in half of the simulations. This difference is most likely due to the difference in the freeze-out timescales. While Visser et al. (2012) uses a constant freeze-out timescale for CO and N_2, Pnautilus calculates the freeze-out rate at every time step according to the current abundance and the binding energy of the given species. This way, our result resembles reality better. Additionally, the HCO^+ and N_2H^+ abundances are $1-2$ orders of magnitude lower that might be due to the different reaction rates. CO ice plays a crucial role in the formation of more complex species like methanol, methyl formate and other complex organic molecules on the surface of grains (Chuang et al. 2018; Garrod et al. 2006; Simons et al. 2020; Watanabe et al. 2002). For this reason, the amount of CO in the gas phase after bursts gradually decreases in our simulations that is mostly visible on figures d), e) and f). The results of Visser et al. (2012) do not indicate such an effect as UMIST lacks grain surface reactions. Even though this difference does not have a significant effect on the behaviour of the five gas phase species studied here, we would like to track complex molecules on the grain surfaces, therefore we decide to use the KIDA database.

5 Chemical uncertainties

It is challenging to create the same environment in a laboratory than that exists in the inerstellar space, therefore chemical databases rely on both theory and experiments to obtain reaction coefficients. A natural question would then be how the uncertainties on these coefficients propagate on to the abundances. Wakelam et al. (2006) aimed to answer this question for the osu.2003 gas phase chemical network. In their models, they had constant temperatures of $\sim$10 K and densities of $\sim 10^4$ cm^{-3}. As both our chemical database (gas-grain network) and physical environment (higher density, episodic accretion) is different we conduct a similar statistical study.

The base of this test is the Monte Carlo method. We run N simulations that have the same physical parameters ($n = 10^5$ cm^{-3}, $\tau_q = 10^4$ yr and everything else is the same as described in Section 4.3) but each of them differ in the rate coefficients for all reactions according to their uncertainties. This means that we have N relative abundances for each species at all given times. To make our analysis simpler, we choose to work with the end-time abundances. Our reasoning is that we expect bigger variations in the abundances after evolving our systems for longer. Therefore, the highest uncertainties are expected to be at the end of the simulations. We choose the parameter set with longer quiescent phases for the same reason. From the N relative abundances we calculate an average, $\langle log(X_i) \rangle$, and an uncertainty, $\Delta log(X_i)$ for the species i. The uncertainties are calculated as follows:

$$\Delta log(X_i) = \frac{1}{2}(log(X_{i,max}) - log(X_{i,min})) \tag{24}$$

where $log(X_{i,min})$ and $log(X_{i,max})$ are defined by the shortest interval ([$log(X_{i,min})$, $log(X_{i,max})$]) that contains 68.3% or 95.4% of the logarithmic relative abundances. This corresponds to 1σ or 2σ uncertainty, respectively. Since we work in log-space, the resulting uncertainties show how many orders of magnitude the abundances of the species vary for the N simulations. The choice of working in the log-space

is encouraged by KIDA mostly using lognormal distribution for its reaction rates. This means that the logarithm of the reaction rate k_i has a normal distribution with a standard deviation of the uncertainty factor F_i. Most of the reactions are assigned such an uncertainty factor, however there are reactions with no estimated uncertainty. For such reactions, we set the uncertainty factor to be $F_i = 2$.

As described earlier in Chapter 3, a number of parameters are used to calculate the reaction rates so that it is in accordance with the temperature. We calculate the uncertainties for $T = 10$ K since our system spends most of the simulation time at this temperature. The parameter α is always multiplicative, in opposition with β and γ that are not present in all equations, so we only change the value of this parameter. The method considering one reaction is as follows: first, we calculate the reaction rate at 10 K using the originally given parameters and the corresponding reaction rate equation. Then, knowing the rate and uncertainty factor we generate the distribution function and draw a value from it. Lastly, we convert this new reaction rate back to a new α parameter. We do these steps for all reactions, let them be gas phase or grain surface reactions, to produce a new set of reaction rates. Then we repeat the process N times.

Wakelam et al. (2006) concluded that an amount of $N = 2000$ simulations was more than sufficient for convergence. Nonetheless, we conduct our own convergence test as our chemical network has more reactions with additional grain surface and gas-grain reactions. Our physical model also has higher density and a varying temperature that strengthens the need for a separate convergence test. We calculate the mean relative abundances for all species as a function of the number of simulations, and then normalise these values by the corresponding overall mean values, i.e. the actual average values of all simulations. All species show convergence, therefore we keep $N = 2000$ as the number of Monte Carlo simulations. Due to the high number of species and their ice counterparts, we only demonstrate this convergence for a handful of relevant species on Figure 6 that are discussed later in Chapter 6.

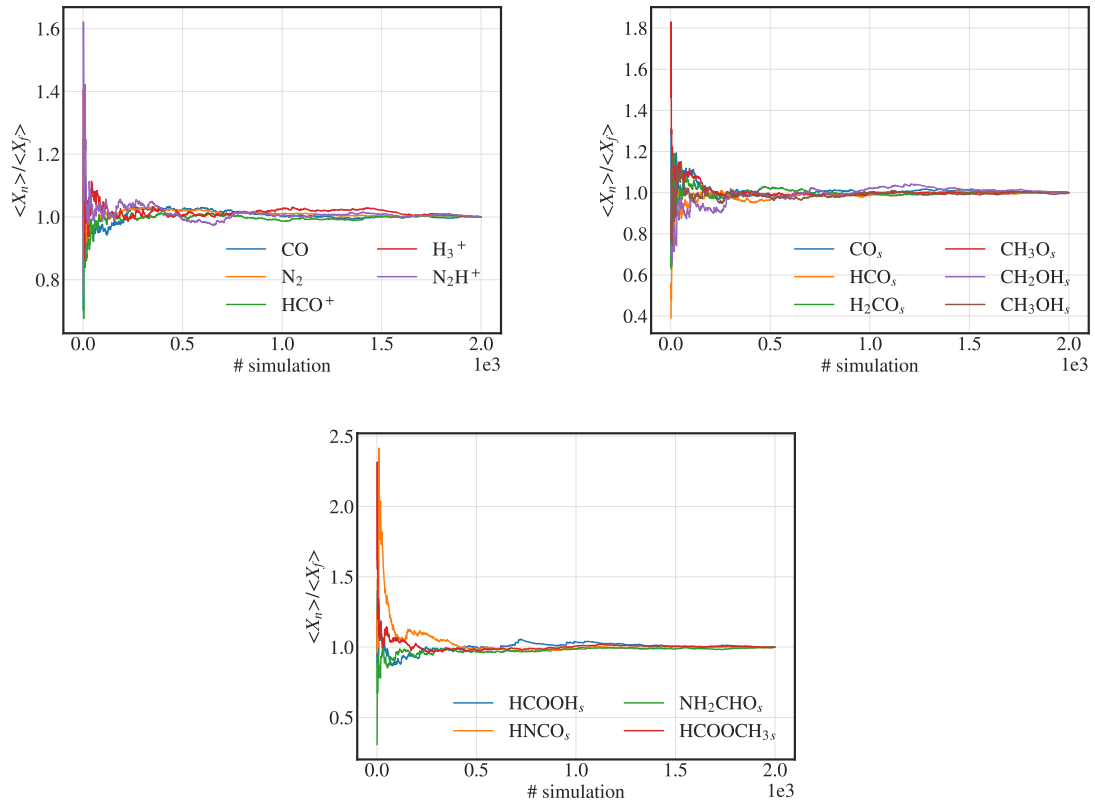

Figure 6: Convergence of the relative abundances for a handful of species in the Monte Carlo simulations. The abundances were normalised by the average abundances of all simulations and shown as a function of the number of simulations. The subscript s refers to species in the surface layer.

The derived 1σ and 2σ uncertainties for the species are shown in a histogram form on Figure 7. Both the mean and median of the 1σ uncertainties are $\sim$1, which means that the general uncertainty of the abundances is less than an order of magnitude. However, there are some outlying data points that are especially visible for the 2σ uncertainties. We suspect this to be a numerical artifact. We make our assumption on the fact that species with highest error values have overall relative abundances lower than 10^{-18} that is already below the observational limit in the millimetre regime (Perotti 2021). Their low abundance might introduce numerical errors. We decide exclude these species from the uncertainty test. To confirm the viability of such an act, we do a simple statistical test on our error values. With an increased number of bins, we simply integrate through our normalised histograms

and reject species with that have a p-value less than 0.01 or 0.05. We do this for both the 1σ and 2σ uncertainties and compare them with the histograms made after the rejection relying solely on physical arguments (see on Figure 8). Rejecting data points with a p-value less than 0.05 produces a very similar result to that of obtained by relying on the physical arguments. However, it excludes slightly more species at the higher end and less species on the lower end of the uncertainties. Nevertheless, excluding outlying or physically irrelevant data points does not really change the median of the uncertainty. The median value of the 1σ uncertainty is roughly 0.75 and 1.5 for the 2σ uncertainty that correspond to a factor of $\sim$6 and $\sim$30, respectively.

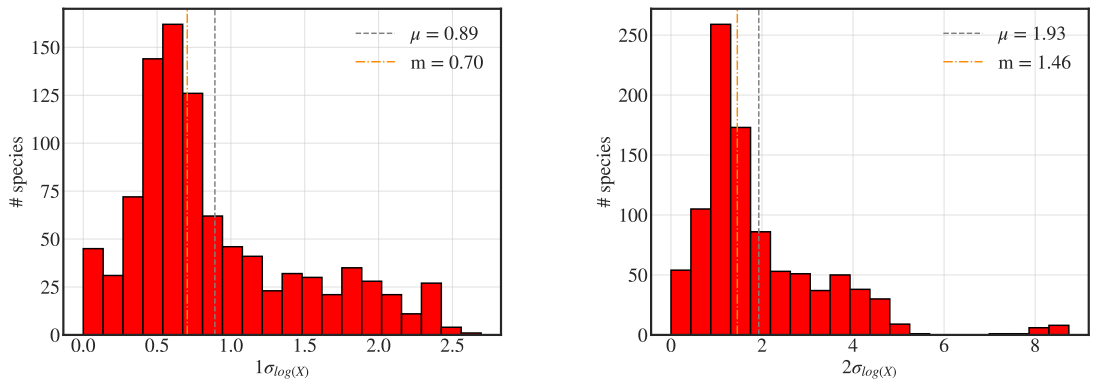

Figure 7: Histogram of 1σ (**left**) and 2σ (**right**) uncertainties for all species with the mean (μ) and median (m) values.

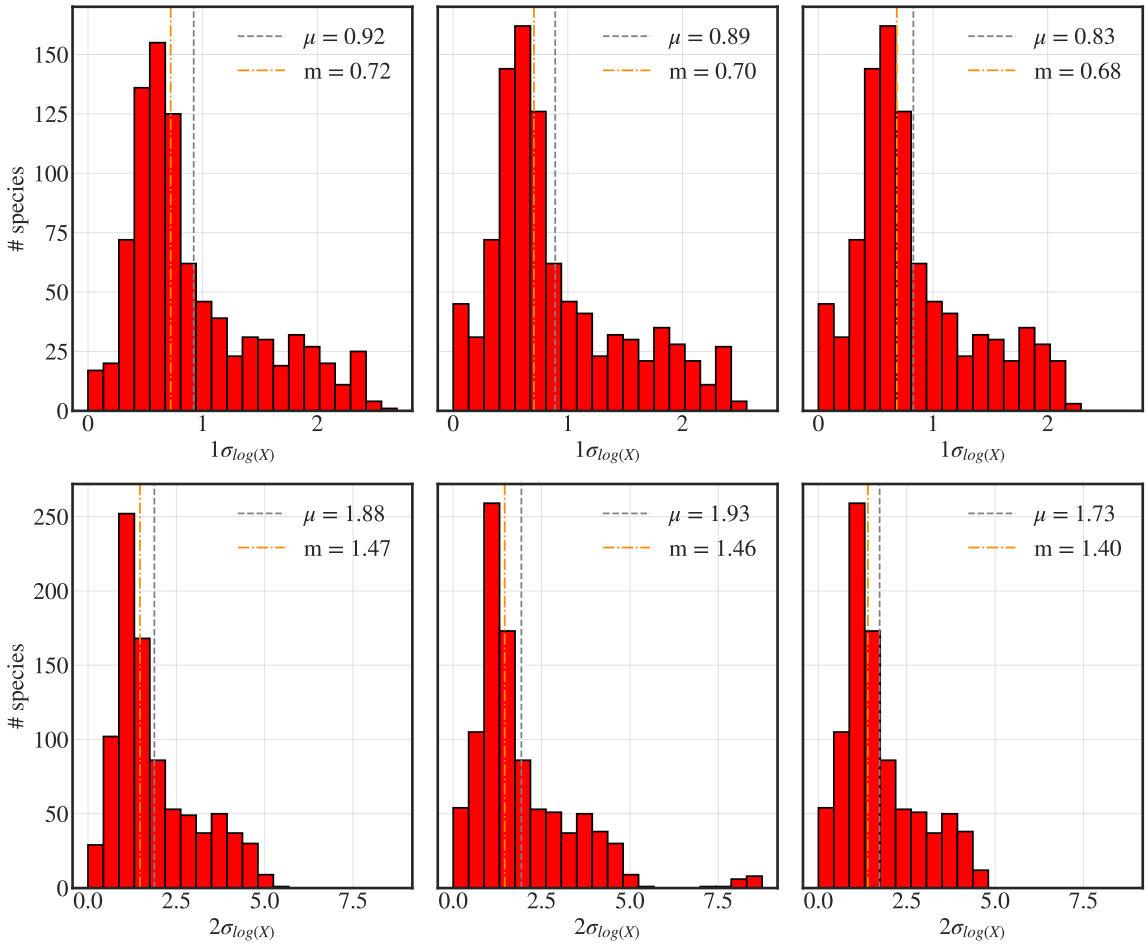

Figure 8: 1σ (**top row**) and 2σ (**bottom row**) uncertainties for all species after rejecting the outlying points with the corresponding mean (μ) and median (m) values. The rejections were either based on physical (**first column**) or statistical reasoning (see text for details). During the latter one, we rejected points with a p-value less then 0.01 (**second column**) or 0.05 (**third column**).

The uncertainties of the solid phase species considered in Chapter 6 are below the previously determined mean values. Even their 2σ values are below one order of magnitude. However, some gas phase counterparts of theirs, such as methyl formate and formic acid, show an above median 1σ uncertainty of $\sim$1.00 and $\sim$0.86, respectively. The uncertainties of other studied COMs in the gas phase do not exceed the median values, but they are closer to them than their solid phase equivalents. Within our temperature range, organic molecules mainly get into the gas phase through non-thermal desorption mechanisms. Thus, the higher uncertainty

for the gas phase COMs makes us believe that the processes that drives molecules from one phase to another are more sensitive than mechanisms happening in only one phase.

We also investigate whether varying the reaction rates have an effect on the relation between the interesting and important species (see on Figure 9). We do so by comparing the average abundances retrieved from the Monte Carlo simulations with the abundances from our original simulation. We also include the abundances corresponding to the 1σ and 2σ uncertainties. We conclude that, for most species, the average abundances match quite well with the original values, making the relations of the studied species physical properties. However, H_3^+, HCO^+ and N_2H^+ behave differently. In the uncertainty test, their average abundances are higher than in the original setup. This is especially true in the case of HCO^+ that experiences a drastic change in its ratio with H_3^+ as it is above unity for most of the simulation time instead of being below one. This might be due to the slightly more CO and H_3^+. Similarly, the slightly higher average abundance of N_2 results in more N_2H^+. The small increase in the gas phase CO and N_2 might be due to the higher sensitivity of the desorption mechanisms. Similarly, the cosmic ray ionisation leading to H_3^+ from H_2 might be a sensitive process too.

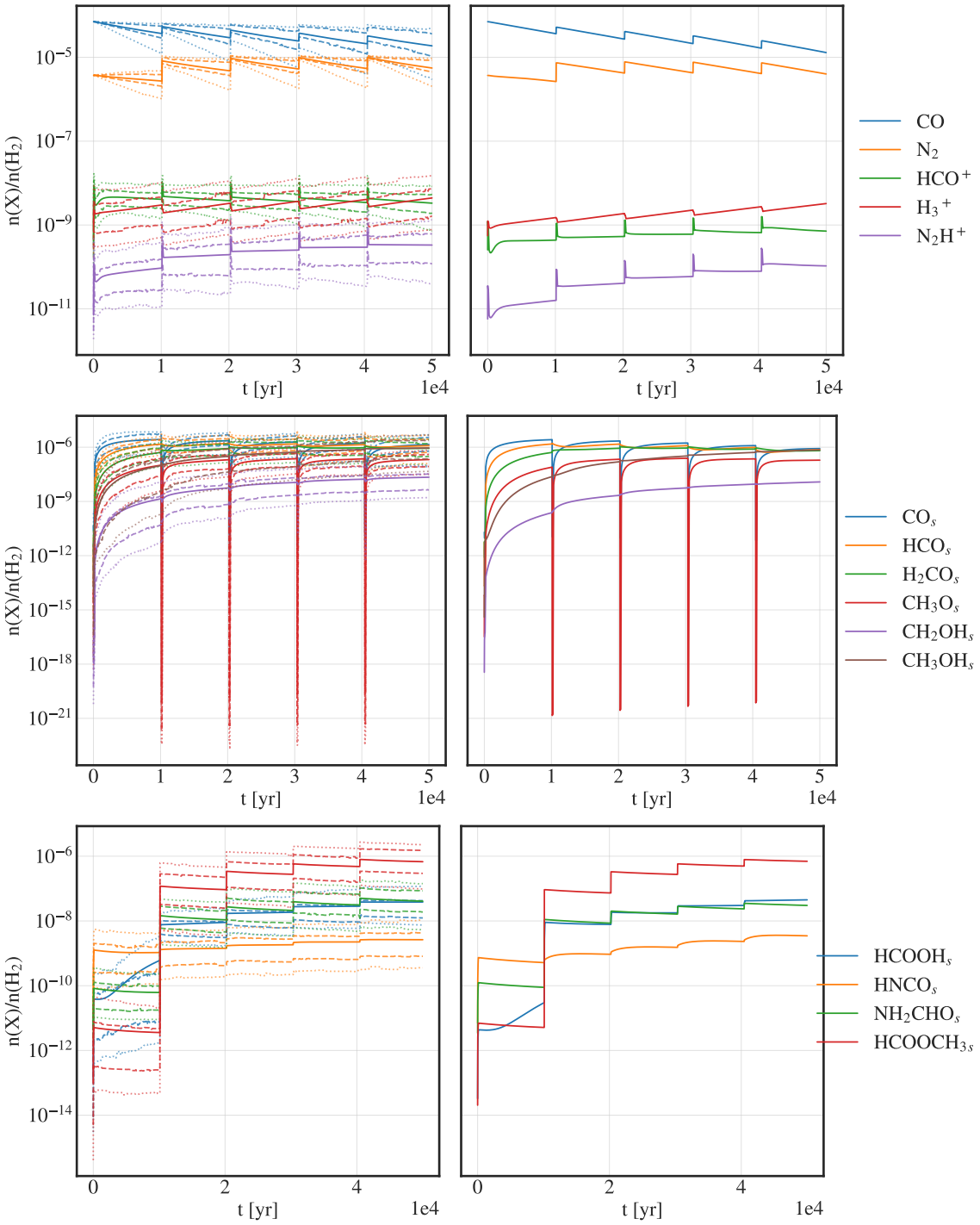

Figure 9: **Left column:** average relative abundances with the corresponding 1σ (dashed lines) and 2σ (dotted lines) uncertainties obtained from the Monte Carlo simulations. **Right column:** relative abundances in our default simulation with $n = 10^5$ cm^{-3}, $\tau_q = 10^4$ yr, $T_b = 30$ K. The subscript s denotes species in the surface layer.

6 Physical properties and their effects

Different physical environments might affect both the physical and chemical evolution of the protostellar system. In this chapter, we explore what effects the different physical parameters in the models have on the chemistry. Such a parameter is the number of phases, i.e. whether the solid phase is divided into a surface layer and a mantle or not. Introducing a phase, the mantle, in which the molecules exhibit lower reaction rates might have some effect on the surface reactions. Another parameter is the existence of episodic accretion itself that is in the centre of this thesis. As discussed earlier in Chapter 4, episodic accretion alters the abundances of five simple and often studied species. Here, we investigate what it does with other molecules. We also explore the effects of the overall gas density as it determines the freeze-out timescales. Another parameter that regards the freeze-out mechanism is the prestellar phase as it offers more time for freezing-out. Last, but not least, the temperature that the envelope is heated to determines what species sublimate. It also changes the temperature dependent reaction rates, therefore we investigate the effects of the burst temperature too.

6.1 Number of phases

As mentioned in Chapter 3, we can choose to have either one or two phases of ice (surface layer and mantle), resulting in two or three phases in total, respectively. We compare the abundances of the five species studied by Visser et al. (2012) along with the simplest complex organic molecule, methanol, in the solid phase. We use the same six simulation parameter sets as in Section 4.3 with either two or three phases implemented.

Considering CO, N_2, H_3^+, HCO^+ and N_2H^+, the abundances differ by a factor of <5 at all times, in all simulations. However, the magnitude of theses differences vary from simulation to simulation as the total density and the length of the quiescent phase also have an impact on them. The higher the density or the

longer the quiescent phase, the bigger the differences are (see on Figure 10 and on Figures 32–35 in Appendix A). Regardless, the effects of these parameters will be studied more thoroughly in Section 6.3. For now, we focus on simulations with a density of $n = 10^5$ cm^{-3} and quiescent phases of $\tau_q = 10^3$ or 10^4 yr. Our reason is that these parameters are the most realistic (Hsieh et al. 2019; Koumpia et al. 2017). With both burst frequencies, the abundances differ by less than a factor of two, but for the longer quiescent phase model we have bigger discrepancies. The most stable species is CO, which is not surprising, since it is the most abundant, i.e. it has to change the most in order to see the relative difference. The most sensitive species are HCO^+ and N_2H^+ as their abundances are highly dependent on CO and N_2. A small change in the abundances of the latter species can significantly alter the relative amount of HCO^+ and N_2H^+ due to their low abundances. The difference in the CO and N_2 abundances could be due to the different freeze-out rate between the two and three phase models. In general, the freeze-out is faster in the more realistic three phase model, so the relative abundances drop after bursts.

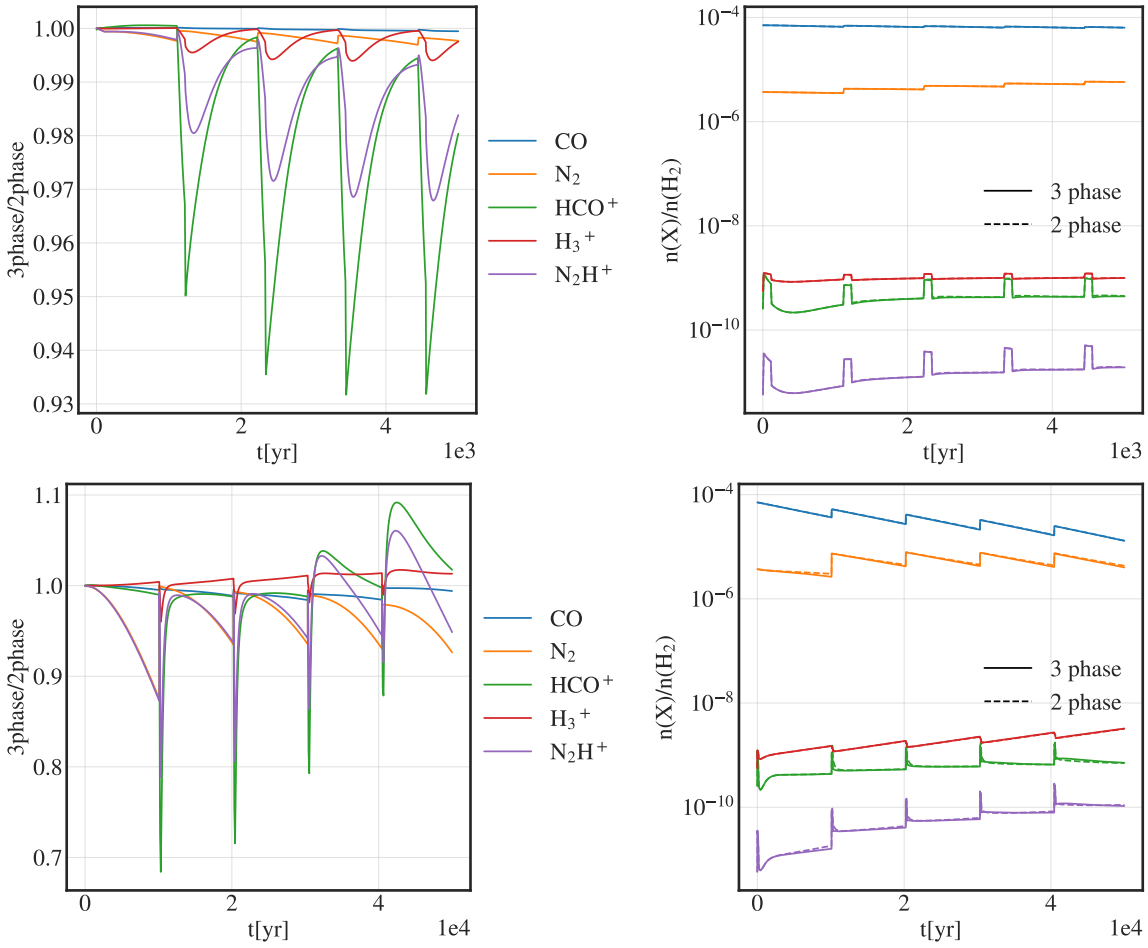

Figure 10: Comparing simulation with two or three phases in total. **Top row:** simulations with density of $n = 10^5$ cm^{-3} and quiescent phases of $\tau_q = 10^3$ yr. **Bottom row:** simulations with density of $n = 10^5$ cm^{-3} and quiescent phases of $\tau_q = 10^4$ yr.

Methanol is around five times more abundant in the three phase model (see on Figure 11 and Figures 36–39 in Appendix A). This could be explained by the higher capacity or rather the better storing capabilities when working with three phase model. This explanation lies in the nature of the surface layer and the mantle. The molecules in the mantle move slower, hence their reaction rate is lower – by a few orders of magnitude – compared to the surface layer. This makes the mantle to function as a kind of reservoir. Another explanation might be that the molecules residing in the mantle cannot go through desorption as they have to reach the surface layer first. This means the general desorption rates are lower in the three

phase model leaving more species in the solid phase to react (or be stored). All in all, methanol reacts or goes through desorption with a lower chance in the three phase model as it is being stored in the mantle. Other, more complex molecules might behave in a similar way. Though the final abundances are not significantly different, we choose to use the more realistic three phase model. This decision is also encouraged by Ruaud et al. (2016) who argued that the three phase model resulted in good agreement with observations for more species in the ice.

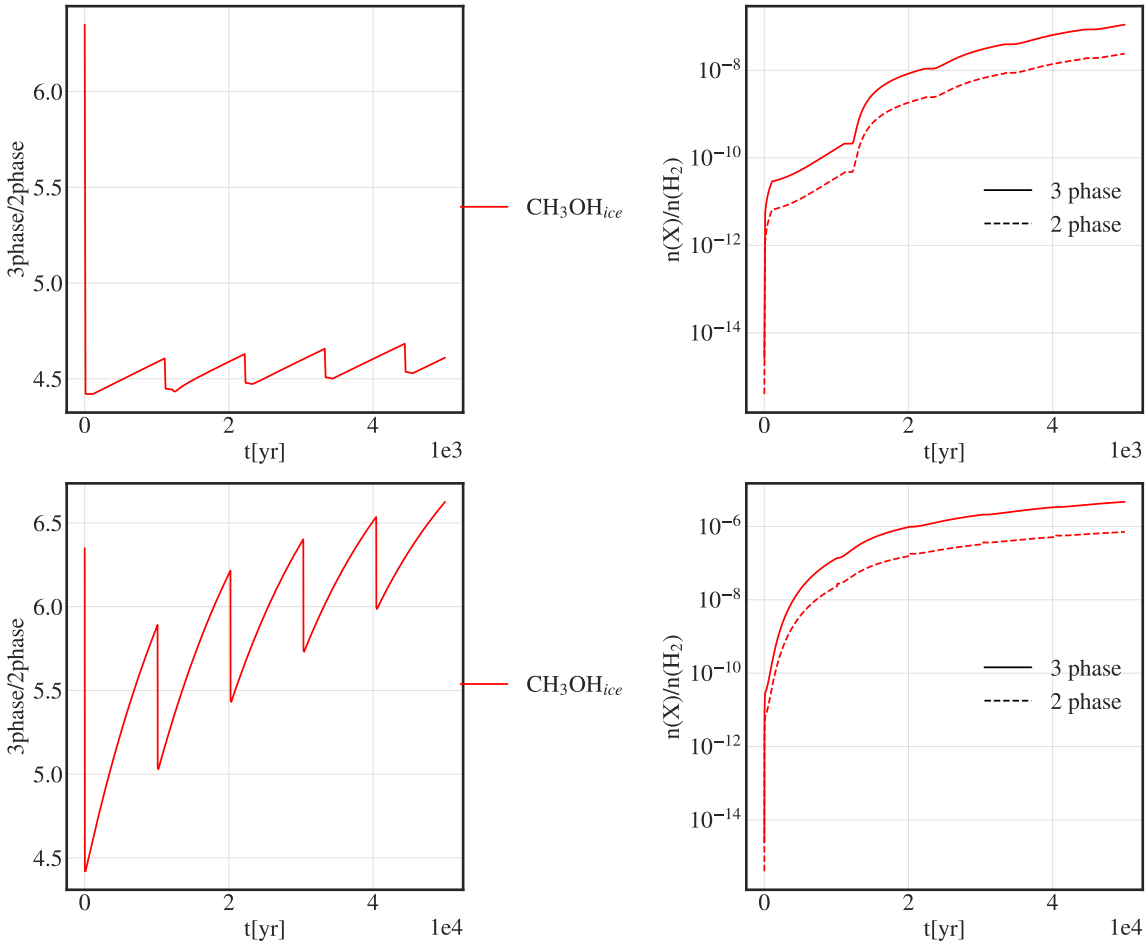

Figure 11: Comparing methanol abundances between simulations with two or three phases in total. **Top row:** simulations with density of $n = 10^5$ cm^{-3} and quiescent phases of $\tau_q = 10^3$ yr. **Bottom row:** simulations with density of $n = 10^5$ cm^{-3} and quiescent phases of $\tau_q = 10^4$ yr.

6.2 Existence of bursts

In this part, we study the soul of this thesis: whether periodic accretion leaves any marks on our simulations as we expect form certain observations (Frimann et al. 2017; Hsieh et al. 2019; Jørgensen et al. 2015) or not. We run simulations with and without bursts and compare the abundances of the same species we worked with in the previous section. Then we study every species, but this time the abundances used for comparison are taken from the end of the simulations.

Taking a look at the five main species (Figure 12) the effect of periodic accretion on CO and N_2 are obvious and expected: the bursts enhance their gas phase abundances, so the simulations with bursts have higher abundances of gas phase CO and N_2 at all times. The increased number of these molecules produce more HCO^+ and N_2H^+ as already described earlier. On the other hand, bursts decrease the abundance of H_3^+ for the same reason.

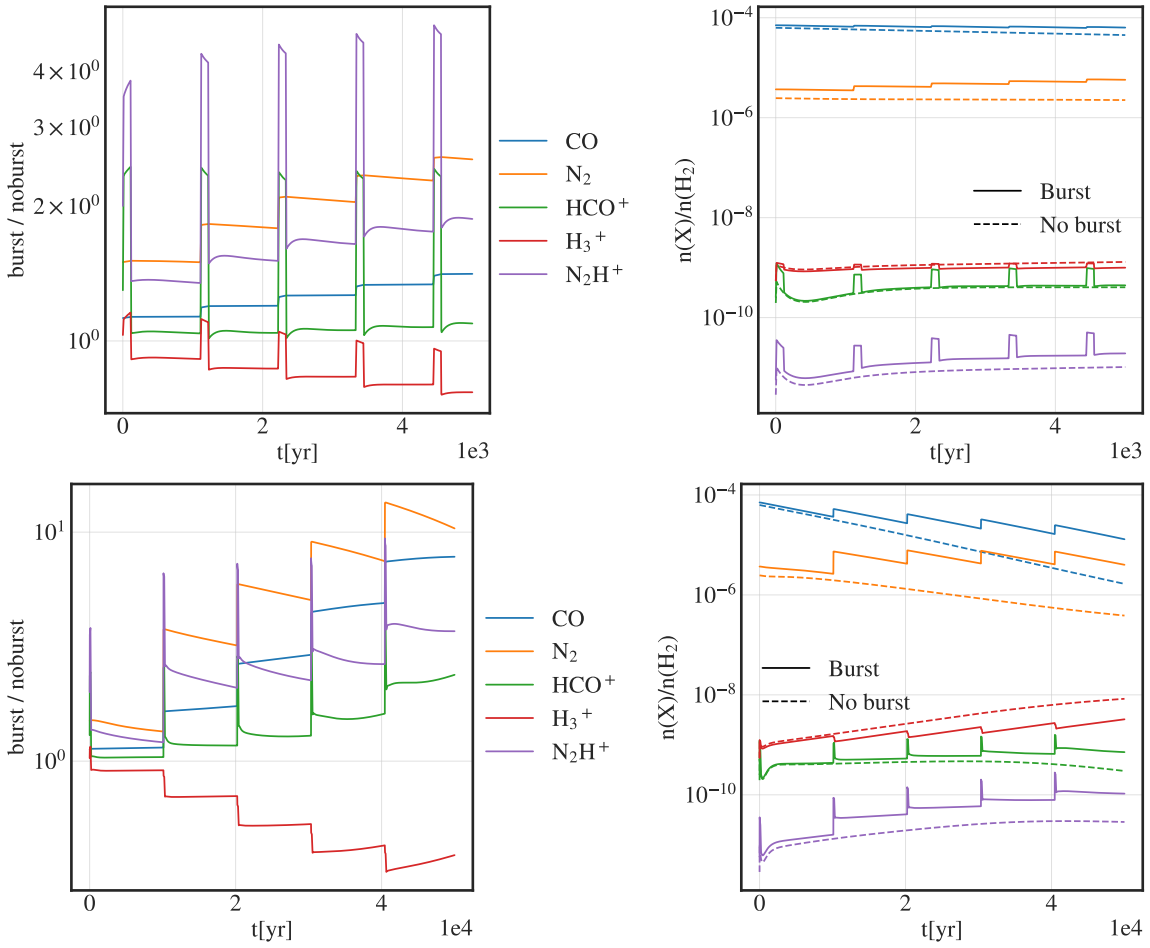

Figure 12: Comparison of the five main species between simulations with and without burst with gas density of $n = 10^5 \text{cm}^{-3}$. **Top row:** quiescent phases of $\tau_q = 10^3$ yr, **Bottom row:** $\tau_q = 10^4$ yr.

Methanol is assumed to be formed on grain surfaces, through several hydrogenation steps (both with and without an energy barrier) starting from CO (Chuang et al. 2018; Garrod et al. 2006; Simons et al. 2020; Watanabe et al. 2002). Therefore, we expect the non-burst model to have more methanol due to the excess amount of CO ice. However, this is not the case in all our simulations. Let us consider the same simulations as before. The simulation with density of $n = 10^5$ cm^{-3} and quiescent phases of $\tau_q = 10^3$ yr seems to be counter intuitive and have more methanol throughout the whole time, whereas the simulation with the same density and $\tau_q = 10^4$ yr has slightly less methanol, but only by the end as shown on

Figure 13. We assume that the increased temperature during bursts enhances certain steps which effect is overcome with time in the non-bursting model simply due to the higher abundance of reactants. Combining this idea with the fact that our simulations start with a burst, it explains the excess methanol at early times.

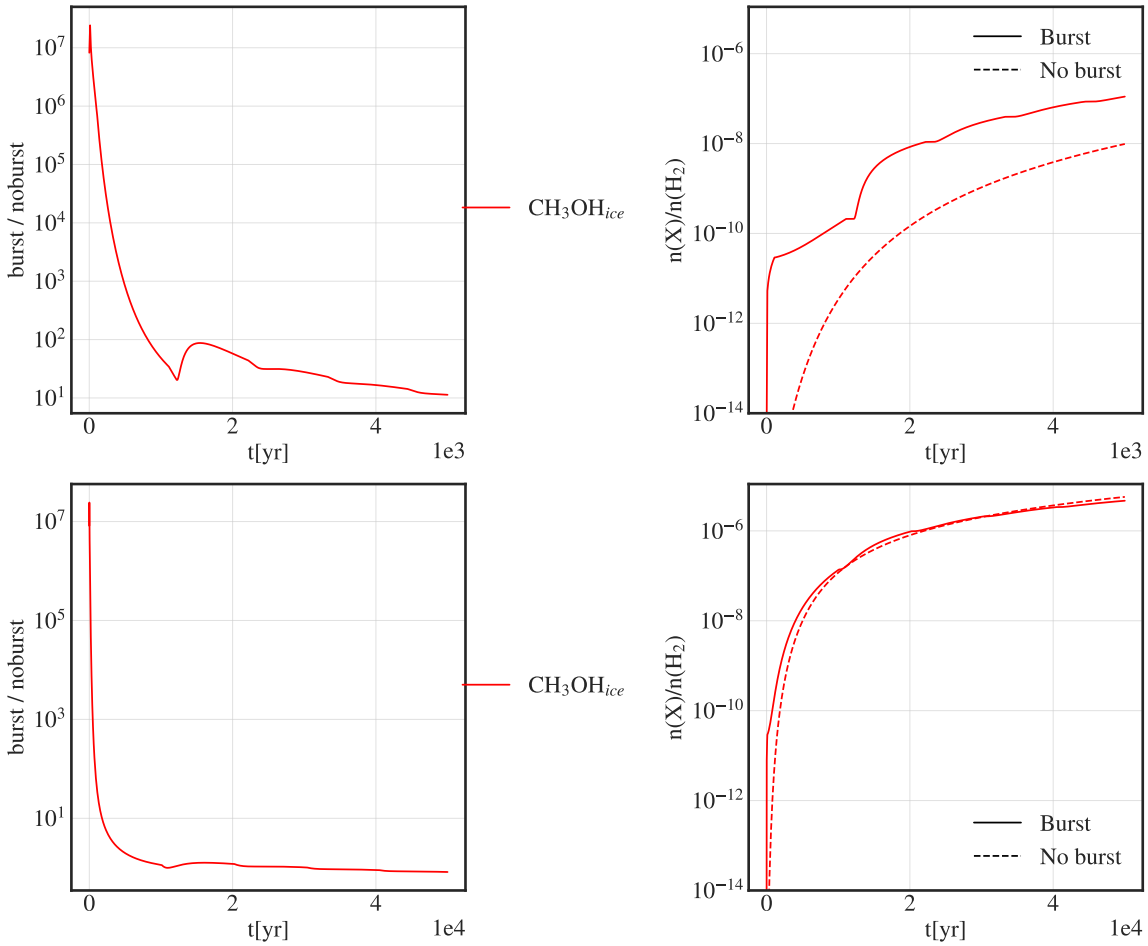

Figure 13: Comparison of methanol ice abundances between simulations with and without bursts. The gas density is $n = 10^5 \mathrm{cm}^{-3}$ with quiescent phase of $\tau_q = 10^3$ yr (**top**) or $\tau_q = 10^4$ yr (**bottom**). The mantle and surface layer abundances are added together.

In order to shed more light on this behaviour we study the hydrogenation steps that lead to methanol formation in more detail. The overall production and destruction rates, along with the abundances, are shown on Figure 14 whereas the more detailed rates, showing the most significant reactions, are shown in Ap-

pendix B. We argue that most of the time, the reaction rates in the mantle are at least around $1-2$ orders of magnitude lower than in the surface layer. Additionally, we find that the mantle only has around four times more of the relevant species. Therefore, we focus on the surface layer and the figures only contain reaction rates in this phase.

The first step is to form HCO from CO ice. This is the most significant destruction reaction of CO ice during the quiescent phase. However, the rate plummets drastically during bursts. This is most likely due to the loss of solid phase CO due to evaporation. Its abundance decreases as well during bursts that is due to the enhancement of the next hydrogenation step and hydrogen abstraction (back to CO ice). This enhancement is caused by the faster movement of molecules in the ice which allows them to meet and react more often. The two destruction reactions with H share the same rate at all times which makes the looping relevant. Next, HCO turns into H_2CO (formaldehyde). As mentioned before, this step is enhanced during bursts. However, the destruction of formaldehyde is enhanced during the quiescent phase. This results in lower abundance of H_2CO in total, especially for longer quiescent phases. The enhanced destruction might be simply due to the excess amount of H_2CO that is produced during bursts. The overall destruction rate decreases but stays higher than in the non-burst model until the latter catches up (there is not enough time for the two rates to converge before the next burst at the beginning). The two most prominent destruction reaction pathways of H_2CO are hydrogen addition and abstraction that share the same rate again. These rates drop by a few order of magnitude during bursts. Hydrogenation of H_2CO mostly leads to CH_3O, i.e. methoxide radical. Pairing this with the increased production of $HCOOCH_3$ (methyl formate) during bursts from CH_3O and HCO means that the tendency of the abundance of CH_3O mostly follows that of H_2CO, but instead of increasing during bursts, it plummets. The other hydrogenation reaction of H_2CO leads to CH_2OH, i.e. hydroxymethyl radical, but it has a higher energy barrier than forming CH_3O, therefore it is less probable (Simons et al. 2020). This is reflected in its abundance being around an order of magnitude lower. It is rather

formed via the hydrogen abstraction reaction of methanol. Its destruction has the same looping behaviour as every other species in the chain when reacting with H. Both reactions peak during bursts, hence bursts decreases the amount of CH_2OH compared to the non-burst scenario. At the end, we reach methanol. Following the previous statements, it is mostly formed from CH_3O during the quiescent phases and from CH_2OH during bursts. The latter reaction still has 2 orders of magnitude lower rate, thus the methanol abundance rather follows the pattern of the abundance of CH_3O. We note that according to a new study by Simons et al. (2020), the CH_3O + H_2CO reaction is a more dominant production pathway of methanol, along with the dissociation of more complex species. This is not the case in our network.

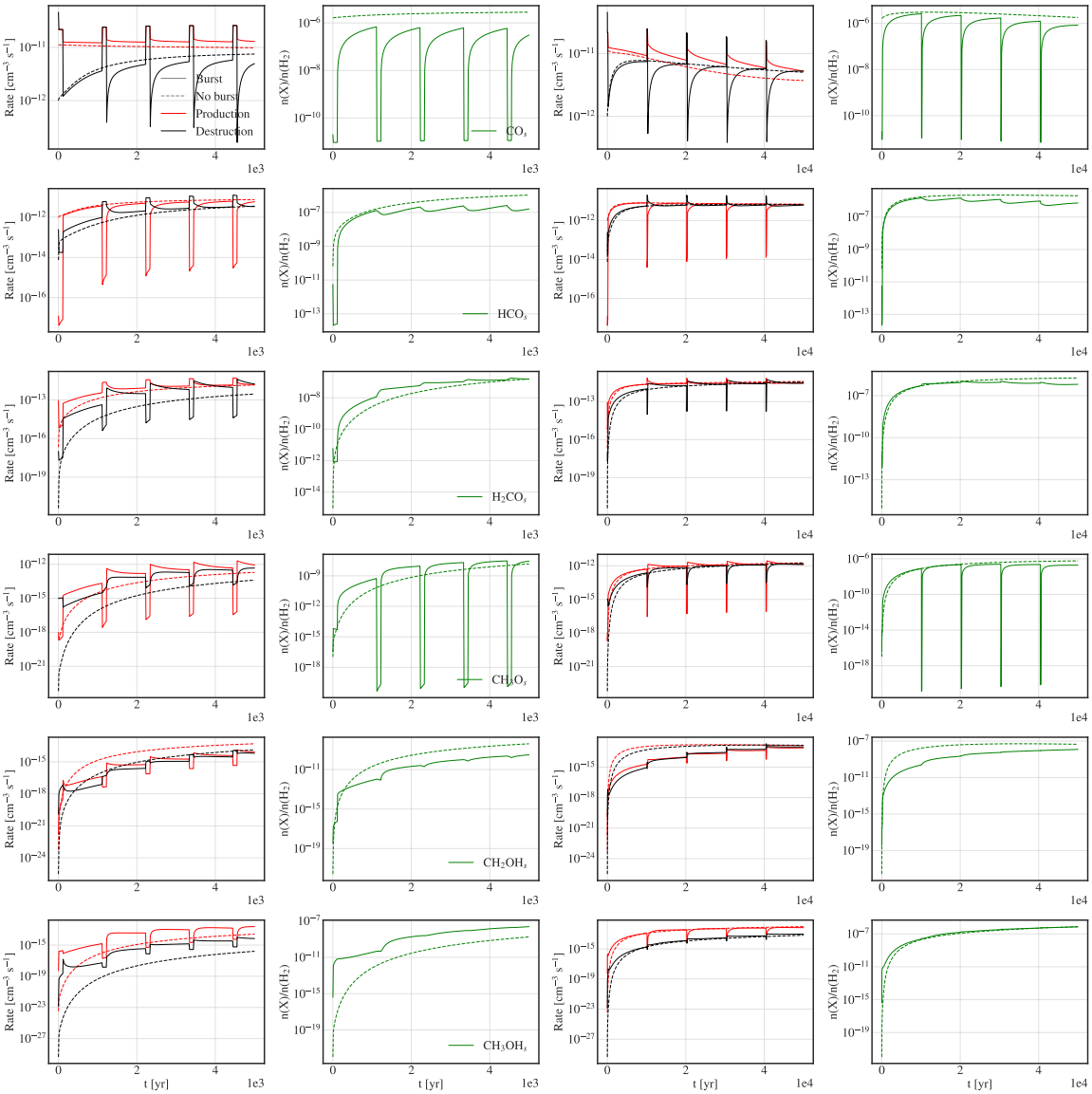

Figure 14: Overall production (red) and destruction (black) rates for the members of the methanol chain with (continuous line) and without bursts (dashed line). The species are: CO, HCO, H_2CO, CH_3O, CH_2OH and CH_3OH, starting from the top row. The first two columns are results from the simulation with $n = 10^5$ cm^{-3} and $\tau_q = 10^3$ yr, whereas the last two columns show the results of the simulation with $n = 10^5$ cm^{-3} and $\tau_q = 10^4$ yr.

Now, we turn our attention towards every species present in our network and investigate how much they are affected, if they are at all, by episodic accretion. We use the same simulations as before. We focus on the abundances at the end of the

simulations with and without acccretion bursts and consider the species that has more that a factor of 100 difference in their abundances between the two models.

As it is shown on Figure 15, $HCOOCH_3$ and NH_2CHO (formamide) go through the most significant alterations. They are more than $\sim 10^6$ times more abundant in the solid phase in simulations with bursts. This factor is reduced to $\sim 10^4$ in the gas phase for $\tau_q = 10^3$ yr, probably due to the low temperature as complex organic molecules undergo mainly chemical desorption. COMs would need around $50 - 100$ K in order to thermally desorp (Jørgensen et al. 2018). Other species like HCOOH (formic acid), HNCO (isocyanic acid) and CH_3OCH_3 (dimethyl ether) are enhanced by a factor of $\sim 10^3$. Species with lower ratios between the simulations are formed a bit faster at 10 K than the species with high ratios, therefore they likely catch up with the effect of the bursts more. The overall differences are reduced for the longer quiescent phase model. Every ratio is lower and hence fewer species pass our filter. This is most likely due to the longer time available for freezing-out (if it is in the gas phase) or reacting. Nevertheless, methyl formate and formamide still have significantly high ratios indicating their sensitiveness towards the physical environment. One could think that comparing the short and long quiescent phase simulations might not be valid, since the length of the simulations differ. Therefore, we run the $\tau_q = 10^3$ yr model for $5 \cdot 10^4$ yr. Now we have a similar result to the $\tau_q = 10^4$ yr model: methyl formate and formamide ices are still more than 10^5 times more abundant compared to the non-burst simulations. However, gas phase cyanamide takes over and has the highest ratio of $\sim 10^8$ along with NH_2CNH^+.

Interestingly, there is no significant difference in the other direction[2]. It seems like the bursts do not reduce any species' abundance that much. This might be surprising since if one species is enhanced, the abundance of another one – at least one of the reactants – should be lowered. However, both methyl formate and for-

[2]This is only true if we include the Eley-Rideal mechanism, otherwise the species containing a C-C bond have lower ratios of $\sim 10^{-4}$. The mechanism does not have an effect on species with higher ratios.

mamide starts to be formed from CO which we have an infinite supply of, relatively speaking. This idea possibly explains why there is no significant losses for the intermediate species.

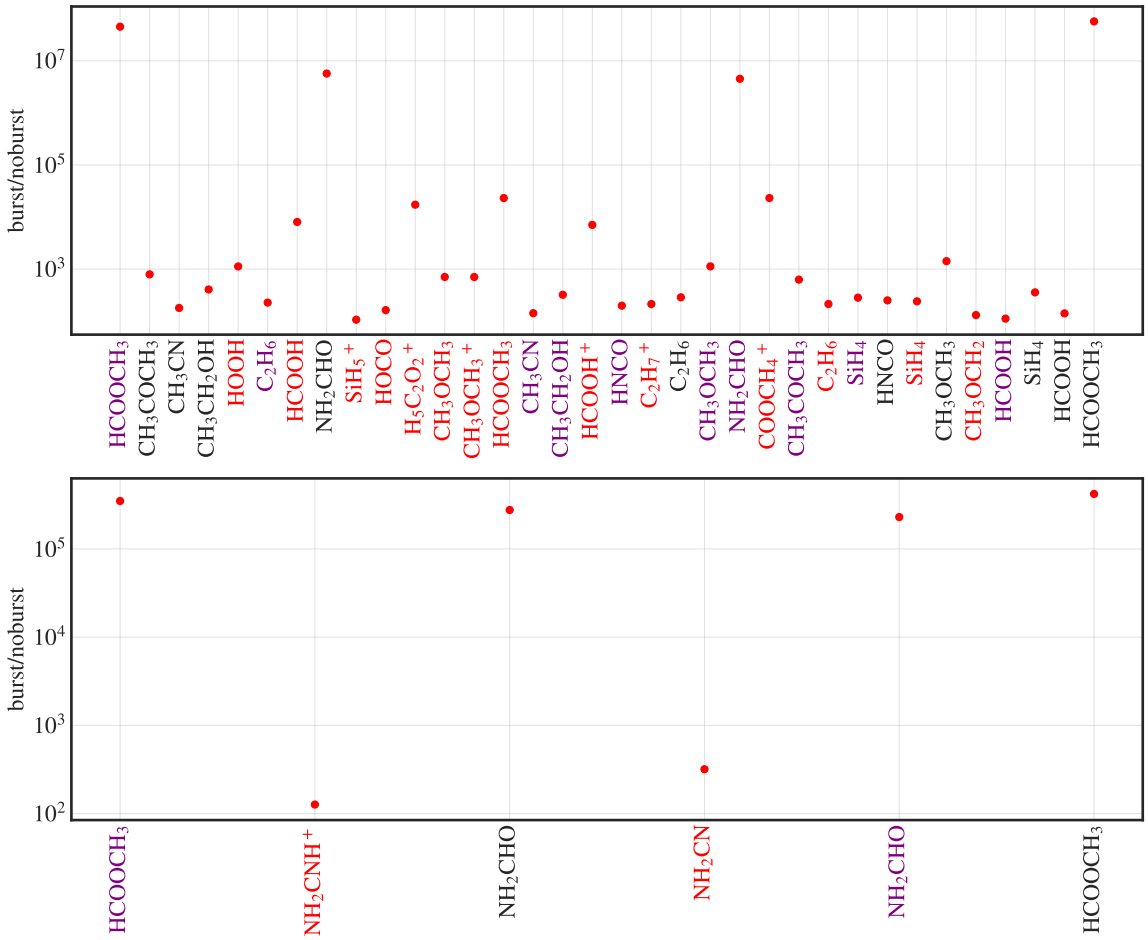

Figure 15: Ratio of the species at the end of the simulation with and without bursts. Only species that are altered by at least a factor of 100 are shown. Gas phase molecules are shown in red whilst species in the surface layer and mantle are written in black and purple, respectively. The simulation parameters are $n = 10^5$ cm^{-3} and $\tau_q = 10^3$ yr (**top**) or 10^4 yr (**bottom**).

Other members of the chemical network of methyl formate (Simons et al. 2020) are not present on our plots. We might ponder on the question: why is this the case? The answer is simple yet not so appealing. The branch containing those reactions is missing from KIDA. Given that glycolaldehyde (HCOCH$_2$OH) and ethylene glycol ((CH$_2$OH)$_2$) are important prebiotic species that have been observed in hot corino

regions with a variety of ratios (El-Abd et al. 2019; Coutens et al. 2015), this might be a serious defect of the database. Improving on this branch would allow us to test whether the versatility of the ratio of these species could have been caused by episodic accretion.

If formamide is so much more abundant in the simulations containing bursts, then it might be a good tracer. However, we detect gas phase molecules in general, this means that the single point we are looking at has to get closer to the protostar and heat up enough to evaporate the formamide. During the heat up, many reaction could be enhanced that potentially alters the ratio of formamide with respect to other species. Nonetheless, we assume that its ratio with HNCO is not affected significantly during the infall in order to make predictions. HNCO is the species formamide is compared to most often (López-Sepulcre et al. 2019) even though their chemical connection is still debated (Quénard et al. 2018). Nevertheless, their abundance ratio is well studied and any alteration due to burst could be detected. In our simulations, the abundances of this two species are shifted towards higher values as the first burst increases the abundances of both species close to the value they would otherwise have reached by the end of the simulation without any bursts. It is clearly visible, however, that bursts have a bigger effect on the formamide abundance in general (Figure 16). Therefore, the formamide to isocyanic acid ratio increases. What is more, their ratio reaches values above unity. This could imply that after the infall and sufficient heating up, more formamide would be observed than isocyanic acid. According to the collection of observations in López-Sepulcre et al. (2019) this is not the case. This can be explained in different ways: there are other reactions that take over at higher temperatures or our network misses some reactions or a mixture of them.

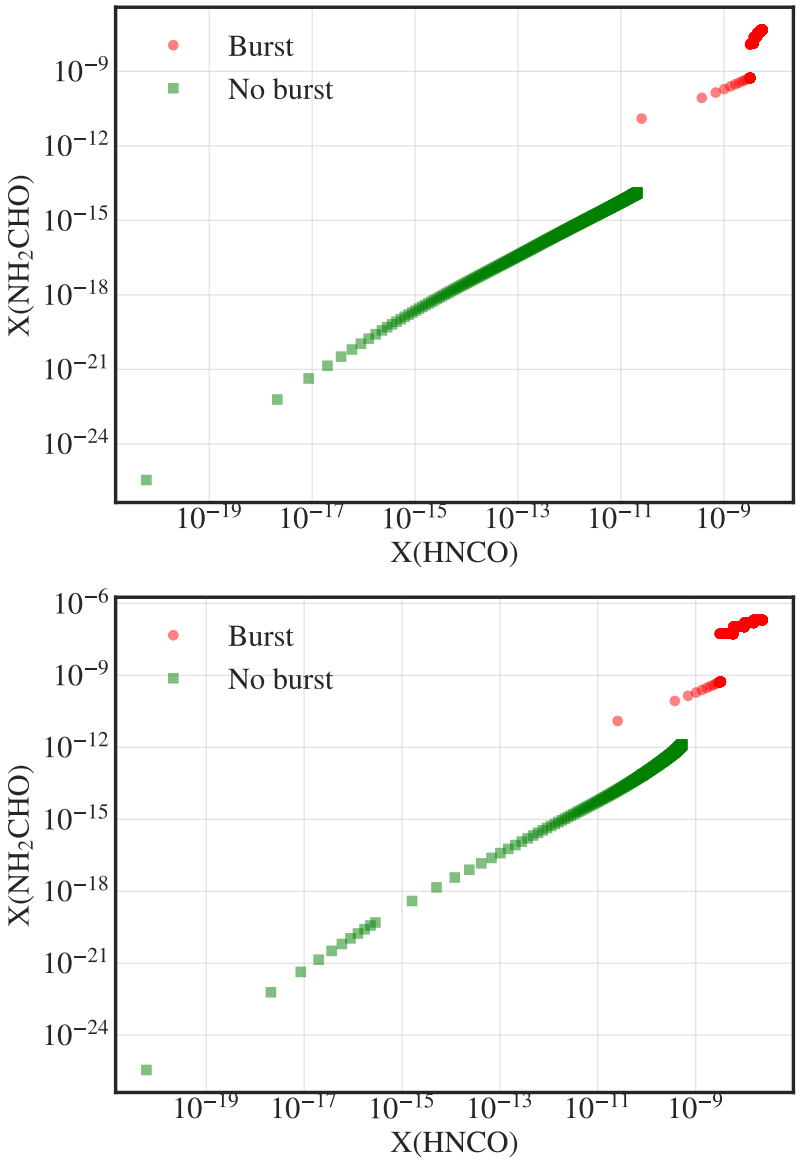

Figure 16: Formamide (NH_2CHO) and isocyanic acid (HNCO) relative abundances to H_2 throughout our simulations. The simulation parameters are as follows: $n = 10^5$ cm^{-3} and $\tau_q = 10^3$ yr (**top**) or 10^4 yr (**bottom**).

According to our chemical network, they are not related chemically. Formamide is formed from the reaction of NH_2 and HCO on the grain surface, during bursts. A small portion ($\lesssim$1%) goes through chemical desorption. During the quiescent phase, its production on the surface basically halts and there is only a slow pro-

duction (with a $2-3$ orders of magnitude lower rate than on the surface during bursts) in the gas phase from the reaction NH_2 + $H_2CO \rightarrow$ H + NH_2CHO. A portion of the gas phase formamide freezes-out, but its reactions with H_3^+ or C^+ are more significant. As for HNCO, it is formed through the hydrogenation of OCN on the surface. This process goes on in both the quiescent and burst phases but is enhanced during the latter. Similarly to formamide, a small portion is being chemically desorped into the gas phase. This is the only formation route for gas phase HNCO at temperatures we use. A small amount of the gas HNCO freezes-out again, but reactions with H^+ or He^+ are more significant.

6.3 Other crucial parameters

In this section, we explore what differences changing the physical environment causes. We make simulations with various gas densities, burst temperatures, burst frequencies and prestellar phases. We choose the standard parameters to be as follows: $n = 10^5$ cm^{-3}, $T_b = 30$ K and $\tau_q = 10^4$ yr. T_b means the burst temperature. The quiescent phase temperature is held at 10 K like before. We compare the abundances of previously discussed species at the end of the simulations. In case of solid phase species, we now sum their abundances in the surface layer and in the mantle.

6.3.1 Density

The freeze-out timescales of different species depend on the density such that the freeze-out timescales decrease with increasing density. Therefore, we expect the abundances of gas phase molecules to drop towards higher densities. We make simulations with densities of $10^4 - 10^7$ cm^{-3}. As it is shown on Figure 17, the gas phase abundances generally decrease with increasing density, as expected. However, there are species that show a peak in their abundances prior decreasing. Such species are for example HCO, H_2CO, NH_2CHO and $HCOOCH_3$. Most likely, their production is enhanced with increasing density, let it be in the gas or solid phase.

Reaching a certain density, around a few times 10^5 cm^{-3}, in general, shortens their freeze-out timescale sufficiently to counteract this mechanism and thus their gas phase abundances drop. One result that might have its implication is the ratio of methanol ice with other members of the methanol chain. This ratio is above unity at lower densities but goes below one at densities higher than around 10^5 cm^{-3}. Therefore, these ratios could suggest the density in observed regions. However, one needs to be careful with such implications as there are many other parameters that could potentially alter the ratios, e.g. burst temperature or even a simple outflow.

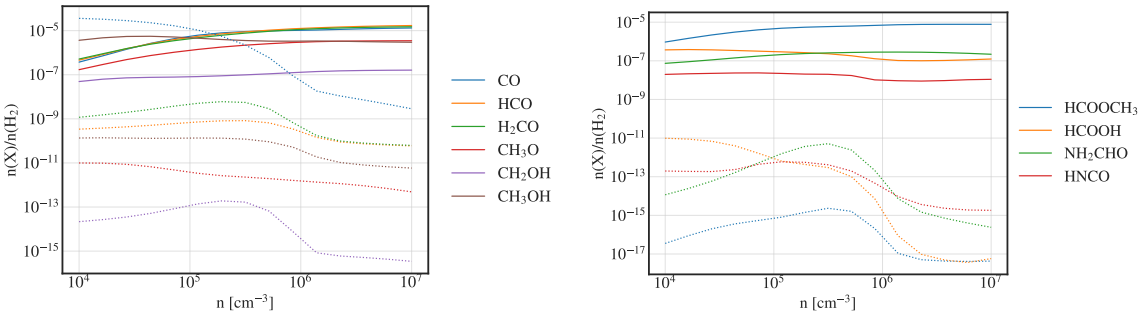

Figure 17: End of simulation abundances for species discussed earlier for different gas densities. The solid phase abundances (surface layer and mantle is added together) are plotted with solid lines whereas dotted lines are used for gas phase abundances.

6.3.2 Burst temperature

Different burst temperatures can enhance different reactions. A simple example would be thermal desorption. If we had a stronger and a weaker burst that increase the temperature, e.g., to 30 and 20 K respectively, then we would evaporate the CO ice in the first case but not in the second. Having less CO ice could result in lower abundances for species related to its presence, for example the methanol chain. The higher temperatures, as discussed earlier, could also enhance certain reactions. The combination of these ideas could be the reason for what we see on Figure 18 that was obtained after running several simulations with temperatures ranging from 10 K to 50 K. The species formed via hydrogenation steps from CO on the surface have lower abundance for higher burst temperatures, but methanol seems to behave the other way around. Consequently, the relative abundance of

these species compared with methanol could be an indicator of the burst temperature. On the other hand, the grains still need to heat up to evaporate methanol into the gas phase which could have another altering effect. Interestingly, the abundance of formaldehyde in the gas phase is independent of the burst temperature. This shows that it is rather formed in the gas phase than on the surface and then being desorped afterwards. Methyl formate production kicks in after the burst temperature reaches around $13 - 15$ K which is in agreement with experiments (Chuang et al. 2016). Once their production is efficient, they are more or less indifferent towards the burst temperature.

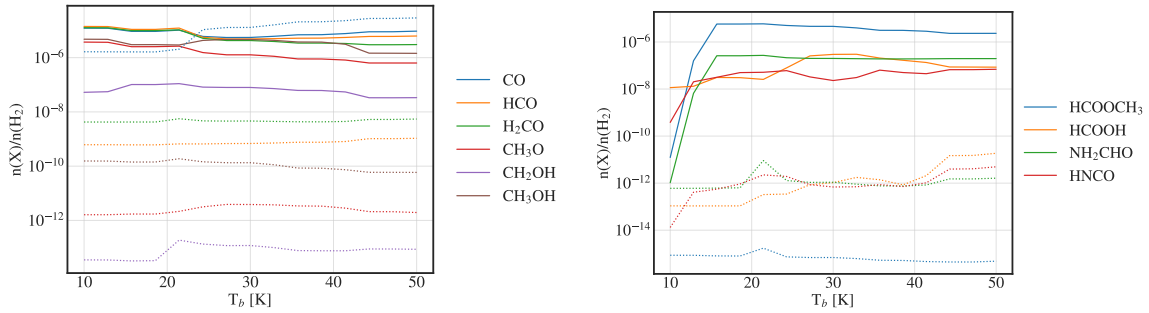

Figure 18: End of simulation abundances for species discussed earlier for different burst temperatures. The solid phase abundances (surface layer and mantle is added together) are plotted with solid lines whereas dotted lines are used for gas phase abundances.

6.3.3 Frequency of bursts

The frequency of bursts, or equivalently the duration of the quiescent phase, plays a role in the freeze-out processes. The rarer the bursts, the more time there is for the gas phase molecules to freeze-out. There is also more time for other processes to take place (e.g. hydrogenation of CO on grain surfaces). We study the effects of the burst frequency by running simulations with burst frequencies of $10^{-4} - 10^{-2.7}$ yr^{-1}. Since we are comparing end of simulation abundances we keep the simulation times equal, i.e. there are more bursts for higher burst frequencies. The members of the methanol chain have an increasing abundance with longer quiescent phase. This is probably due to the higher amount of CO ice that can be hydrogenated. The solid phase abundance of methanol is higher than the abundance of

other members of the chain. Their ratios gets closer to unity with decreasing burst frequency. Therefore, these ratios might imply the frequency of bursts. However, the density alters the ratios significantly too, so one would need to combine these effects to draw viable conclusions. Surprisingly, the gas phase counterparts of the methanol chain members seem to be indifferent to the burst frequency. Solid phase methyl formate and formamide also seem not to be affected by the length of the quiescent phase. This is at least true at the end of the simulations. More frequent bursts fasten up the formation of these species. This leads to them reaching higher abundances and "equilibrium" quicker as shown on Figure 20. In other words, a young protostar with frequent bursts could produce the same amount of methyl formate as an older one with less frequent bursts. The big fluctuation in the gas phase abundance of methyl formate suggest that its gas phase reactions are dominated by destruction reactions, therefore the duration between the last burst and the end of the simulation matters in its end-time gas phase abundance. Formic acid again shows its preference for warmer environment as its abundance goes down with longer quiescent phase.

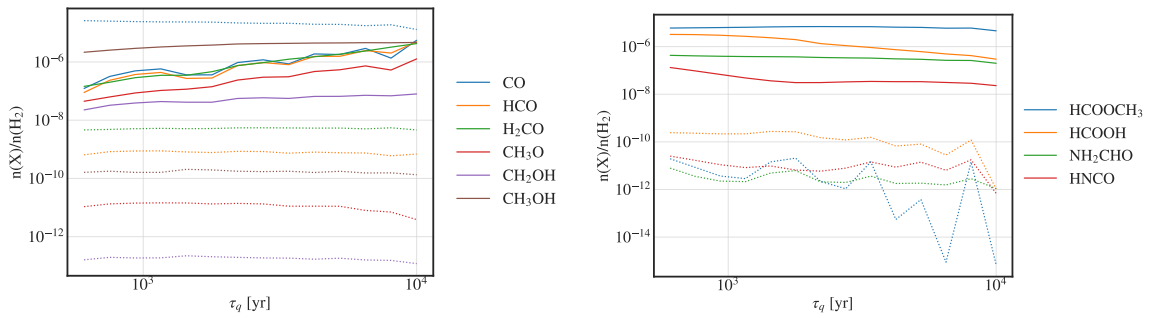

Figure 19: End of simulation abundances for species discussed earlier for different quiescent phase duration. The solid phase abundances (surface layer and mantle is added together) are plotted with solid lines whereas dotted lines are used for gas phase abundances.

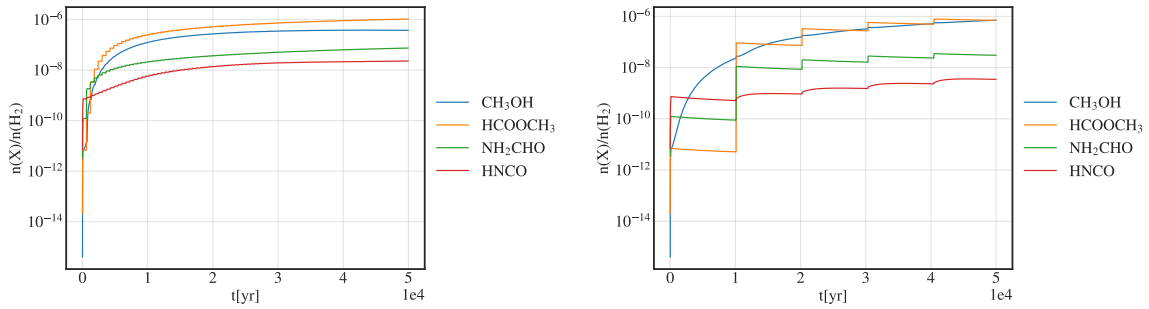

Figure 20: Abundances for a few species with regards to time in simulations with the shortest (**left**) and longest (**right**) quiescent phase duration. The solid phase abundances (surface layer and mantle is added together) are plotted with solid lines whereas dotted lines are used for gas phase abundances.

6.3.4 Prestellar phase

Following Visser et al. (2012), we initiated bursts, and therefore the protostellar phase, right at the beginning of our simulations. However, the chemistry is just as active and interesting during the prestellar phase as it is during the protostellar phase. Many observations have revealed the presence of large O- and N-bearing COMs in dark clouds and prestellar cores (Agúndez et al. 2019; Bacmann et al. 2012; Jiménez-Serra et al. 2016) suggesting efficient COM formation and desorption processes at low temperatures. Such molecules are, for example, CH_3CHO, CH_3OCH_3, $HCOOCH_3$, CH_2CHCN or CH_2CHCH_3 (Jiménez-Serra et al. 2021). We study the effects of the duration of the prestellar phase. It is considered to have a density of $n = 10^4$ cm^{-3} and a temperature of 10 K. The initial abundances and the cosmic ray ionisation rate are the same for the prestellar phase as in the case of models without a prestellar phase (see description in Section 4.3). At the end of the prestellar phase, we initiate the protostellar phase instantaneously, propagating the relative abundances of the species. To put it simply, the prestellar phase is a quiescent phase with lower density that takes place prior to our standard simulation. We study the effects of prestellar phases ranging from $10^2 - 10^6$ yr.

Only prestellar phases longer than $\sim 10^4$ yr have an effect on the chemistry. The solid phase abundances of all members but methanol and CH_2OH of the methanol chain start to decrease after this point. The abundances of these two species in-

crease before they would decrease. The increment might be due to the excess CO ice. CO also has a freeze-out timescale comparable to 10^4 yr in case of the density used, strengthening our explanation. However, methanol goes through reactions too, which could be the cause of its decreasing solid phase abundance in the simulations with a prestellar phase longer than $\sim 10^5$ yr. The solid phase abundances of methyl formate, formamide and isocyanic acid ices decrease with longer prestellar phases once that reaches $\sim 10^4$ yr. These species more or less keep their ratios, meaning that they cannot be used as tracers of the prestellar phase duration. On the other hand, the solid phase abundance of formic acid grows over all these three species' with longer prestellar phases, making its ratio with them a possible information carrier about the past.

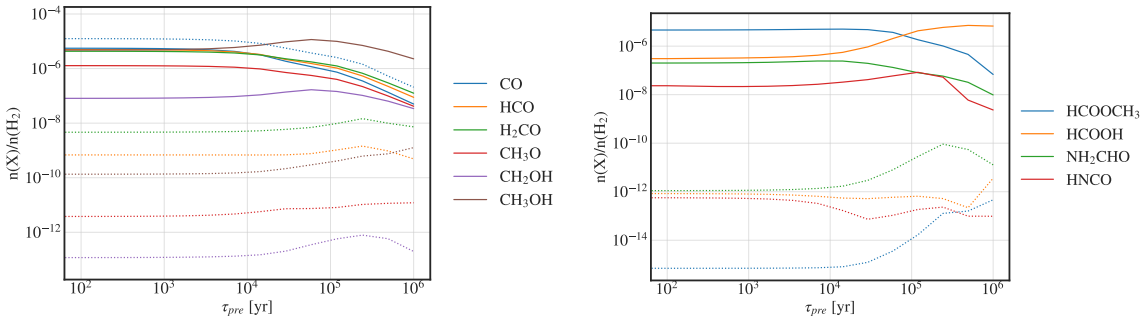

Figure 21: End of simulation abundances for species discussed earlier for different prestellar phase duration with a prestellar core density of $n = 10^4$ cm^{-3} and temperature of $T_{pre} = 10$ K. The solid phase abundances (surface layer and mantle is added together) are plotted with solid lines whereas dotted lines are used for gas phase abundances.

The lower density of the prestellar phase could result in higher temperatures due to the increased amount of interstellar irradiation that can penetrate the core. For a density of $n = 10^4$ cm^{-3} the temperature could reach 12 K (Chacón-Tanarro et al. 2019). Running simulations with that condition does not change the results significantly (Figure 22). It is plausible, that the temperature fluctuates during the prestellar phase either due to external or internal effect. For example, an external cause could be a nearby supernova or a shock wave launched by a nearby star. The motion of the gas and dust could be considered as an internal effect. One could imaginethat a clump of material at gets closer to the edge of the cloud or

to a less dense region and then back to a similar region where it originated from. This would temporarily change the physical parameters, and might look like a weakened episodic accretion. However, this question is beyond the scope of this thesis.

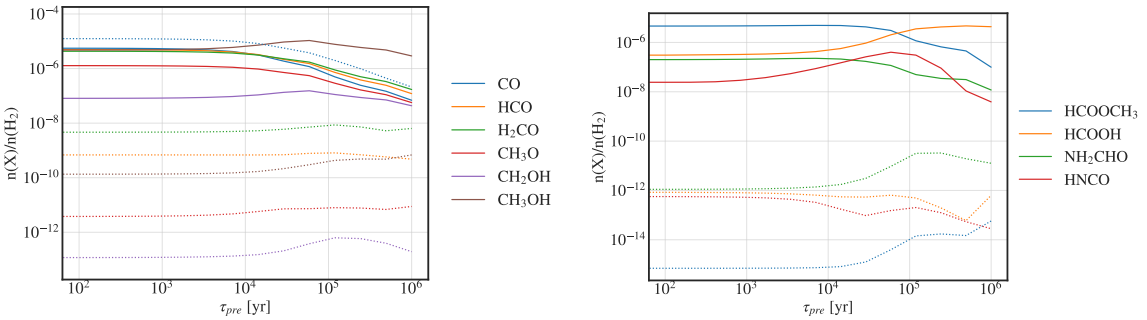

Figure 22: End of simulation abundances for species discussed earlier for different prestellar phase duration with a prestellar core density of $n = 10^4$ cm^{-3} and temperature of $T_{pre} = 12$ K. The solid phase abundances (surface layer and mantle is added together) are plotted with solid lines whereas dotted lines are used for gas phase abundances.

6.4 Summary

In this chapter, we investigated what and how significant effects different physical parameters of the models have on the chemistry. First we studied the difference between models with species occupying two and three phases. Though the difference between the abundances of CO, N_2, H_3^+, HCO^+, NH_2^+ and CH_3OH were $\lesssim$5, we put our finger on the importance of the mantle as a reservoir.

Then, we explored whether episodic accretion alters the abundances of the species. Even though we had already seen that this was the case for some simple molecules, we were interested to see the effects – if any existing – on other molecules as well. We unraveled the mysteries of the methanol chain and learnt that episodic accretion decreases the amount of methanol formed in the long run when compared to models without accretion bursts. We found that episodic accretion did affect the formation and destruction of many molecules with methyl formate and formamide being affected most prominently. We also discovered that our chemical database lacks important reactions that future works should account for.

At last, we studied the importance of density, burst temperature, burst frequency and duration of a prestellar phase. Density and burst frequency both affects the freeze-out processes. They altered the relative solid phase abundances of methanol and other members of the methanol chain in a similar way: their ratios decreased with increasing density or quiescent phase duration. We also showed that the burst temperature played a crucial role in the abundance of methyl formate and formamide as their formation kicked in at $\sim$13 K. Regarding the prestellar phase, we noted that HCOOH could be a good tracer of the prestellar history. However, we conclude that treating these parameters separately could give false potential tracers and we argue that a parallel study on the effects of burst temperature and frequency would be beneficial.

7 Comparison with observation

This chapter is dedicated to compare our models with real life values taken from various observations. The main interest is to see whether introducing episodic accretion into our simulations brings our results closer to or further away from observations compared to the simple models without accretion bursts. Additionally, we again test the effects of different physical parameters.

Given the temperature range of our simulations, the complex organic molecules we study are mainly in the solid phase. Therefore, the straightforward way would be to compare our results with observations of ice compositions in protostellar envelopes. However, such measurements are far from being easily and frequently done. The challenge in detecting solid phase molecules is that they are prevented from rotation and hence vibrational transitions must be used that lie in the near- to far-infrared part of the spectrum. The issue is that infrared observations have relatively low sensitivity (with a lower relative abundance limit of $10^{-6} - 10^{-5}$ with respect to H_2) and that blended absorption bands make it demanding to distinguish between the contributing species (Perotti 2021). The ice features are revealed by absorption lines against infrared background sources, for example bright infrared stars (Boogert et al. 2015). A condition like this is rare, thus making such observations challenging, but it can be found towards dense star forming regions, e.g. Serpens, B35A cloud and Coronet Cloud (Perotti 2021). On the other hand, gas phase detections of COMs are common towards the warmer ($\gtrsim$100 K) regions of the protostellar envelope also referred to as hot corinos. Such high temperatures are enough to sublimate all species from the grain surfaces resulting in a rich and more easily observable gas phase chemistry. Observations of gas phase molecules in the millimetre regime are possible for species with relative abundances as low as $\sim 10^{-12}$ with respect to H_2 (Perotti 2021). With some simple assumptions, we make predictions of what our simulation results could suggest of the observable chemistry in hot corino regions. We make use of both solid and gas phase observations.

7.1 Solid phase comparison

Due to the difficulties of detecting solid phase species, observations have only been made towards a few sources with few molecules detected in the ices. The most complex solid phase species that has securely been observed is methanol (Boogert et al. 2015). Abundances are usually compared to water ice, CO ice or the gas phase counterpart of the same molecule. We focus on four species: CO, CO_2, H_2CO and CH_3OH. All of them show a wide variety of relative abundances in the observations. For example, the methanol to water ice ratio ranges from $\lesssim$3 % (Chu et al. 2020) to $\sim$32 % (Perotti et al. 2020) whilst the methanol to CO ice ratio is observed to be $12 - 317$ % (Chu et al. 2020). Gas to ice ratio of methanol also spans over an order of magnitude, from $1.4 \cdot 10^{-2}$ to $3.7 \cdot 10^{-1}$ (Perotti et al. 2020).

In order to evaluate the effects of episodic accretion, we start by comparing the results of our standard models (with and without episodic accretion) with observed relative abundance ranges (gray areas) with respect to water ice on Figure 23. The observational value intervals are given by various measurements of interstellar envelopes (An et al. 2017; Boogert et al. 2015; Chu et al. 2020; Perotti 2021; Pontoppidan et al. 2004). We also include data for comet compositions (brown areas) tabulated by Boogert et al. (2015). Taking a look at the fractional abundances, we see that different species behave differently. In the case of CO ice, the non-burst scenario gives a better match with observations. As also seen before, CO ice has a lower abundance for the simulation that episodic accretion is incorporated into. Its ratio with water almost leaves the observed range by the end of our simulation, being closer to the mean of the comet values. On the contrary, H_2CO is kept in the range of ice observations by episodic accretion while it overgrows that interval in the non-burst model. In the case of CO_2, even though the burst model pushes its fraction somewhat closer to the mean observed ice ratio, our results are still only on the lower end of the observed range and shows no significant difference between the two simulations. Lastly, methanol ratio with regards to water is also not too much altered for the two models, therefore it does not contain significant

information about the effects of episodic accretion. The results are in between the measured ice and comet compositions.

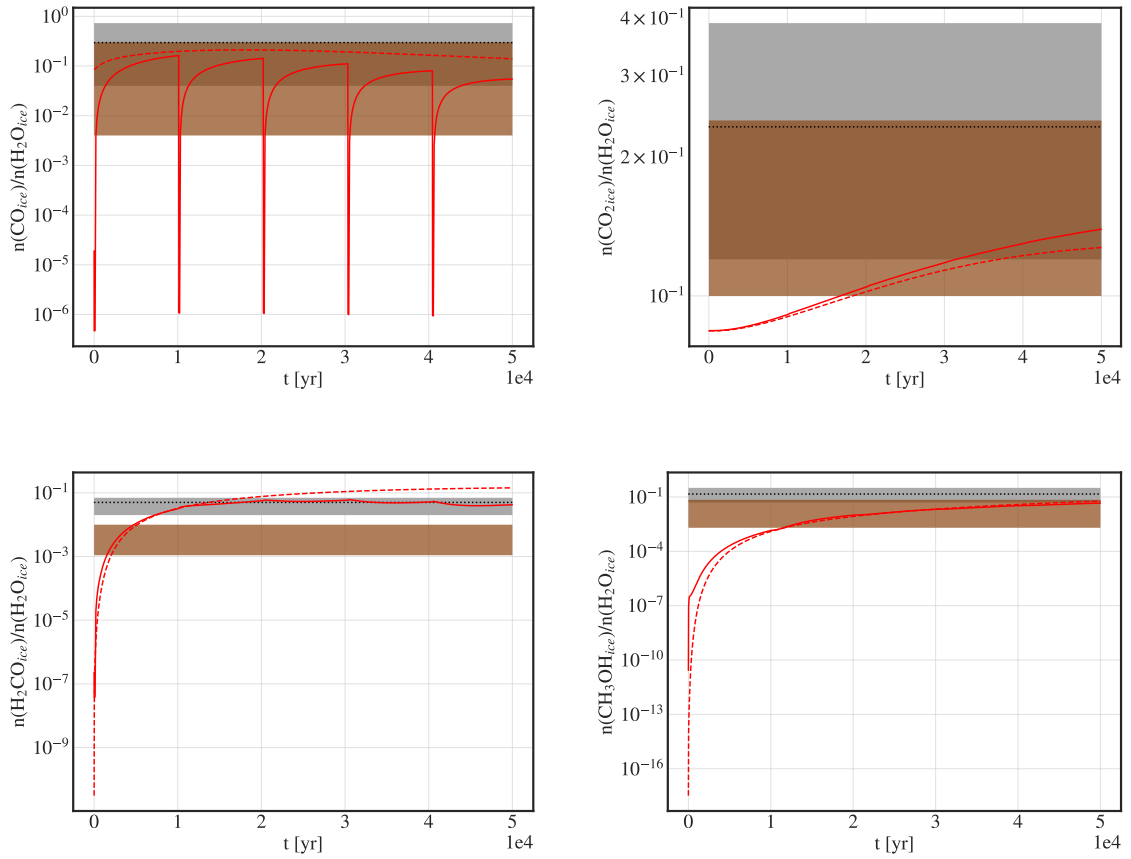

Figure 23: Fractional abundances of different solid phase species with respect to water ice both for simulations and observations. Solid and dashed lines represent our results with and without accretion bursts, respectively. The shaded gray area shows the observed ranges in protostellar envelopes and brown areas represent the range of measured values in comets (An et al. 2017; Boogert et al. 2015; Chu et al. 2020; Perotti 2021; Pontoppidan et al. 2004). Overlapping intervals of protostellar and cometary values exhibit a darker shade of brown.

Water ice is not the only reference used in measurements. There are a few observations comparing gas to ice ratios (Perotti 2021) or taking CO ice as reference (Chu et al. 2020). However, these are only done for CO and methanol in the former case and for methanol in case of the latter. As it is shown on Figure 24, the gas to ice ratio of CO is better reproduced with the episodic accretion model. The

same cannot be said for methanol which means that our model did not produce enough gas phase methanol. A reason for this could be that our temperature range is below the evaporation temperature of methanol, thus it can only get to the gas phase through non-thermal desorption. The observational gas-to-ice ratio values of methanol were taken from Perotti (2021) who argued that, in the past, a shock wave or outflow had crossed the observed regions in the SVS4 and B35A clouds. These past events increased the dust and gas temperatures significantly, thus releasing more methanol into the gas phase and consequently increasing the gas-to-ice ratio of methanol. To put this idea to a test, we make a simulation in which we set the burst temperature to be 150 K. This might be unrealistically high, however our purpose is to demonstrate that the observations could be explained by an event that enables the methanol ice to evaporate. 150 K is more than enough to do so and indeed, the gas-to-ice ratio of methanol is increased, even above the observed range as shown on Figure 25. The overshoot is probably due to the high temperature or rather by the too short time between bursts. Nevertheless, it shows that the idea of a past shock wave is viable. Perotti (2021) also measured similarly high gas-to-ice ratio values for methanol in a different physical environment towards the Coronet Cluster. Here, the main reason for the sublimation of methanol ice is probably its enhanced photodesorption caused by a high external irradiation field. In our models, the too low gas-to-ice ratio of methanol could also be explained by generating more methanol ice than is present in reality. We rule out this reasoning due to the relatively good matches of the fractional abundances of methanol with respect to both water and CO ice. As for the latter one, we note that the simulation with episodic accretion reaches the observed range earlier in time, but by the end it has similar agreement as the non-burst simulation does.

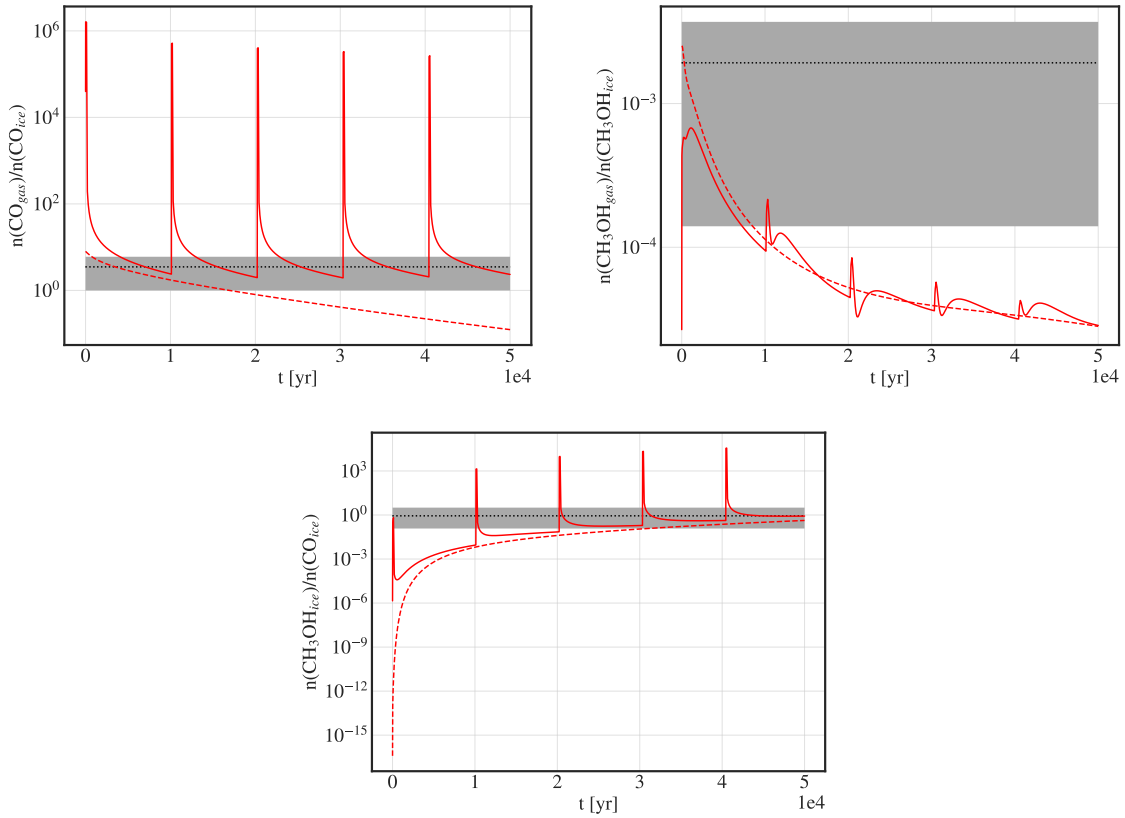

Figure 24: **Top row:** Simulated and observed (Perotti 2021) gas-to-ice ratio of CO (left) and methanol (right). **Bottom row:** simulated and observed (Chu et al. 2020) methanol to CO ice ratio. The gray area shows the observations while the solid and dashed lines represent our simulations with and without episodic accretion, respectively. The too low methanol gas-to-ice ratio along with agreeing CO gas-to-ice and methanol to CO ice ratios suggest that there might have been an extreme event in the past or an enhanced irradiation field in the observed regions that enhanced the gas phase abundance of methanol.

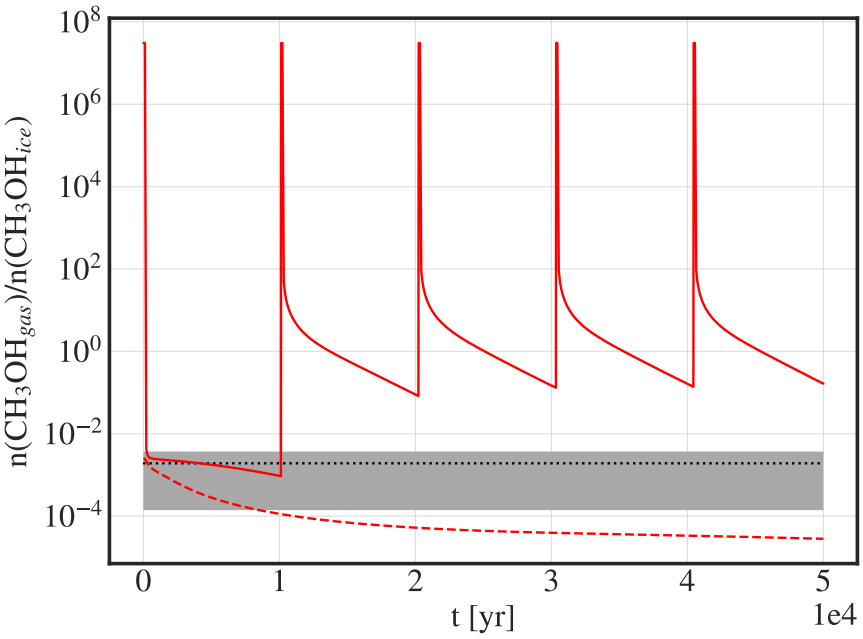

Figure 25: Comparison of our simulation with temperature bursts of 150 K (solid line) with observations (gray area). The burst temperature is enough to evaporate methanol, therefore raising its gas-to-ice ratio, suggesting the viability of the argument about extreme past events, for example a shock wave, in the SVS4 region.

7.2 Gas phase comparison

As in the case of ice composition measurements, gas phase observational values often use a reference molecule. We adapt methanol for O-bearing and isocyanic acid for N-bearing complex organics as a reference following Jørgensen et al. (2020). For example, methyl formate, one of the aforementioned important molecules with high sensitivity regarding the environment, is compared to methanol. Its observed fractional abundance is often not reproduced by previous models. Another common issue with earlier models regards the ratio of the structural isomers of methyl formate (El-Abd et al. 2019; Garrod 2013). For example, glycolaldehyde is often overabundant in the simulations. These issues might be addressed by changing the chemical network used or by changing the underlying physical model itself, e.g. with the introduction of luminosity bursts. We investigate whether the latter option could solve for the present issues.

Our simulations do not contain infall therefore they do not reach temperatures, nor densities, common for hot corino regions. However, assuming that the fractional abundances are not altered significantly during the transition from the outer to the inner envelope allows us to use our results as prediction and thus making our comparison viable. We make this assumption on how, for example, the end-time methyl formate–methanol or formamide–isocyanic acid ratios remain more or less the same when increasing the density or the burst temperature as shown on Figures 17 and 18 in Sections 6.3.1 and 6.3.2. We compare the overall end-time abundances of the chosen species, i.e. we sum the gas and solid phase abundances which is in accordance to the fact that all solid phase molecules are evaporated in hot corino regions. We compare the two models with and without episodic accretion (full and empty black circles, respectively) to observations on Figure 26. Observational values contain information on hot corino regions around low- and high-mass protostars (down or up facing triangles, respectively) as well as comets (diamonds) tabulated in Jørgensen et al. (2020). As discussed earlier, methyl formate and formamide is the two species that is affected the most by luminosity bursts. Not only are their abundances affected by episodic accretion, but their fractional abundances show a much better agreement with observations. Other O-bearing species show a somewhat similar agreement in both models, whereas other N-bearing species show some differences. Even though N-bearing species seem to favour the non-burst model, the differences in the fractional abundances are not more than approximately an order of magnitude which is actually close to their chemical uncertainty ($\sim$0.8 orders of magnitude). Therefore distinguishing between the models might be only viable for methyl formate and formamide. We wonder whether a different physical environment (e.g. with different density or burst parameters) would change this conclusion one way or another.

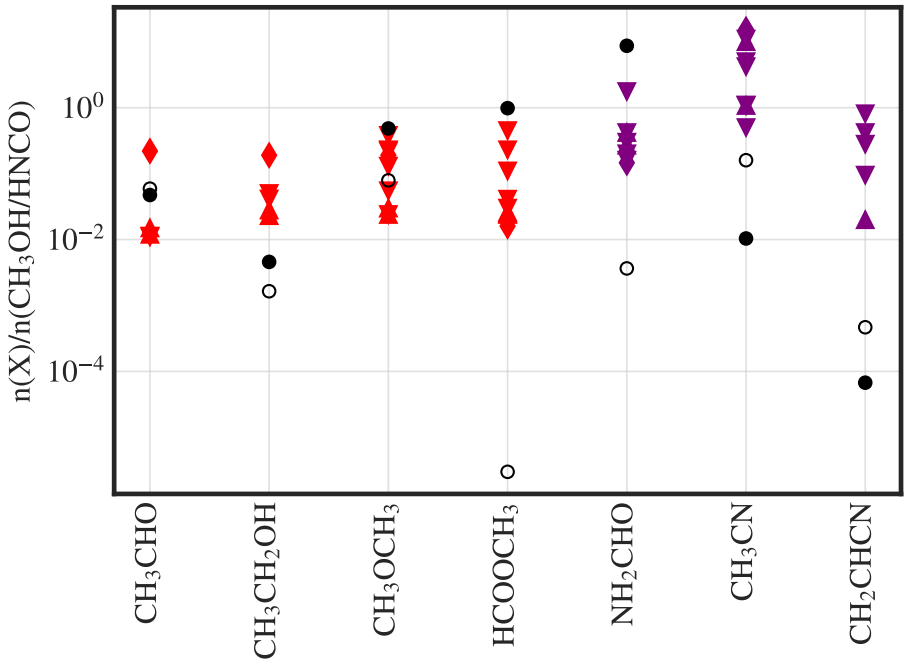

Figure 26: Fractional abundances with respect to methanol (red) or isocyanic acid (purple) for various species. Observational values are represented with down facing triangles for hot corino regions around low-mass protostars, up facing triangles for hot corino regions around low-mass protostars and diamonds for comets as tabulated in Jørgensen et al. (2020). Full circles denote end-time values in our model with episodic accretion, while empty circles do the same for the model without luminosity bursts.

In order to visualise the effects of different environments (Figure 27), we make simulation with various densities, burst temperatures or burst frequencies the same way and with the same ranges as in Section 6.3. Different species are effected differently by density and burst frequency. However, there is a general tendency regarding the burst temperature: the higher the burst temperature, the better the agreement is with observations, although there are molecules, e.g. acetaldehyde (CH_3CHO), that matches the observations just as well for lower burst temperatures. This tendency might suggest that the discrepancy present for the N-bearing species might disappear during infall due to the warm up of gas and dust. To keep our figures as simple as we can, we do not include simulations without episodic accretion.

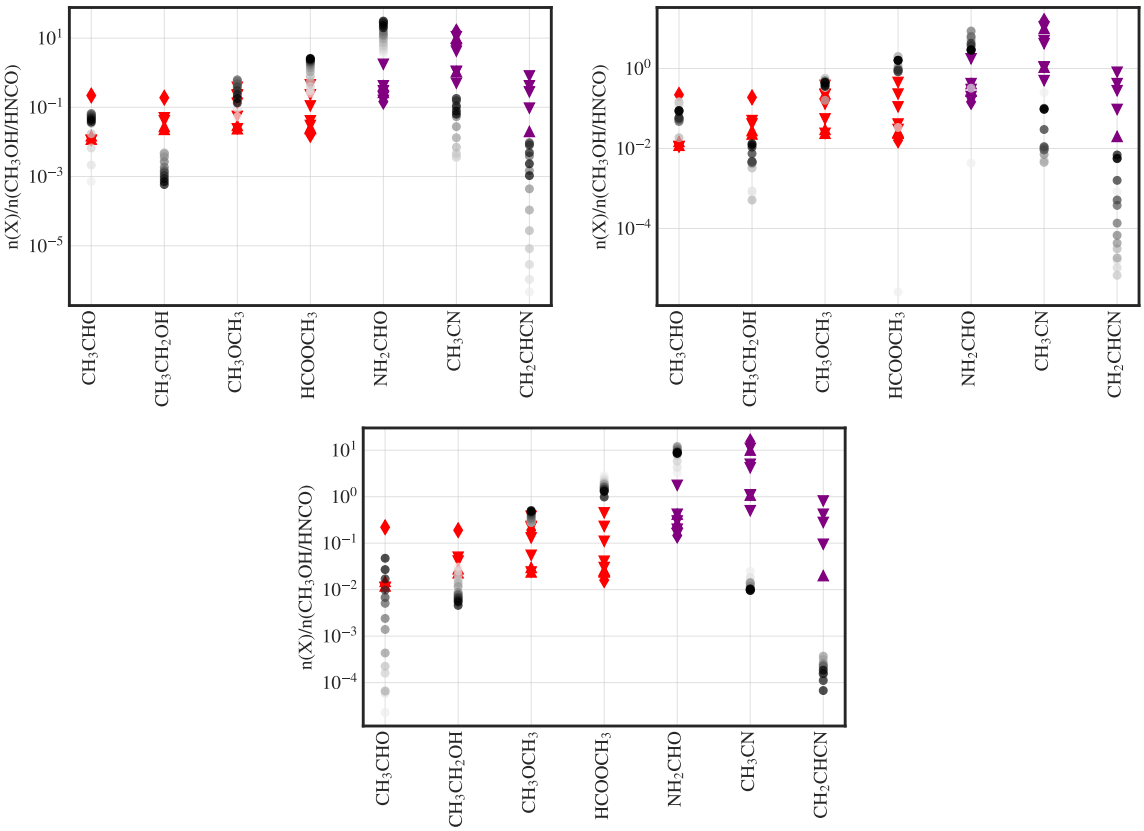

Figure 27: Effects of different physical environments. One physical parameter has been changed for the simulations in agreement with Section 6.3. End-time fractional abundances are plotted with full gray circles. The higher the given parameter, the darker the filling is. Observational values are represented as on Figure 26. The changing parameters are density (**top left**), burst temperature (**top right**) and burst frequency (**bottom**). The density and burst frequency is sampled uniformly in the logarithmic scale while the burst temperature is sampled uniformly in the linear scale.

7.3 Summary

In this chapter, we aimed to compare our simulation results with observations. The characteristic physical environment of our models were that of the outskirts of a protostellar envelope, e.g. low temperature and relatively low density. As a consequence, COMs resided mostly in the solid phase and only went through non-thermal desorption. We made use of the few solid phase observations available in the literature (Boogert et al. 2015; Chu et al. 2020; Perotti 2021). We showed on Figures 23 and 24 that the model with episodic accretion gave, in general, better

agreements with observation than the model without accretion bursts. However, the methanol gas-to-ice ratio, that our models did not succeed to reproduce, indicated the importance of the physical environment, e.g. the presence of an outflow or the strength of the irradiation field.

We made additional comparisons with gas phase observations towards hot corino regions. In order to do so, we assumed that the relative abundance of COMs with respect to the reference molecule (either methanol or isocyanic acid) were not changed significantly during infall. We showed, on Figure 26, that methyl formate and formamide (the two species that are affected the most by episodic accretion) gave much better agreements with observations with the burst model. However, other COMs gave either similar or somewhat worse matches with observations. We studied how the comparison changed for different physical parameters. Though density and burst frequency seemed to have different effects on different molecules while varying the burst temperature altered the end-time abundances with the same tendency. Models with higher temperature bursts gave better agreements with observations, therefore we conclude that a model that couples episodic accretion and infall (during which the temperature rises) could reproduce observed values better. We continue our project with developing such a model.

8 Simple infall model

So far, we have neglected the infalling motion of material due to the relatively short time span of our simulations when compared to the free-fall time. We focused on one volume in an average envelope environment. When comparing results with hot corino observations, we assumed that the ratio of related species would not be altered significantly on their journey towards the warmer inner regions. In this chapter, we make an attempt to improve our model by introducing infall. To keep our model simple, we neglect any motions other than free-fall, e.g. orbital motion. We start by obtaining the density, visual extinction and temperature as functions of time. Then, we vary the temperature according to the effect of an episodically accreting protostar. Finally, we append a prestellar phase to the beginning of our model. In order to analyse the results, we again compare models with and without luminosity bursts to each other and with observations.

8.1 Physical structure

We assume that the volume we are sitting in is free-falling towards the protostar. The free-fall time (t_{ff}) for a cloud with a constant density (ρ) is described as follows:

$$t_{ff} = \sqrt{\frac{3\pi}{32G\rho}} \tag{25}$$

This equation also holds for an envelope with radially changing density profile that results in the so-called inside-out collapse (Hartmann 2008), i.e. matter closer to the centre falls in earlier then matter further outside. Given a radial density profile, one can relate the free-fall time to the radius itself. We can assume that the gas is solely made out of molecular hydrogen and therefore $\rho(r) \approx m_{H_2} n(r)$. Here m_{H_2} is the mass of molecular hydrogen and n is its number density. The radial

number density profile of a protostellar envelope can be described by a power-law:

$$n(r) = n_0 \left(\frac{r}{r_0} \right)^{-p} \tag{26}$$

where n_0 is an initial density at the outskirts of the envelope (r_0). Once the protostar is born, the density profile converges to that of an envelope in free-fall, i.e. $p = 1.5$ (Hartmann 2008). In case of a spherical envelope that spans from r_{in} to r_0, its mass is calculated by

$$M = \int_{r_{in}}^{r_0} dr \; 4\pi r^2 \rho(r) \tag{27}$$

We assume that the total mass is $1 M_\odot$ inside the inner and outer radii that are 10 and 10000 AU, respectively. The outer radius of 10000 AU corresponds to the observed size of a prestellar core. We chose $r_{in} = 10$ AU considering an approximate size of a young protostellar disk (Hartmann 2008; Stahler et al. 2004). Combining Equations (26) and (27) with these values gives us an initial number density of $n_0 = 4.25 \cdot 10^4$ cm^{-3}. After substituting Equation (26) into Equation (25) and inverting the equation we obtain the radius as a function of time:

$$r(t) = r_0 - r_0 \left(\frac{32 G m_{H_2} n_0}{3\pi} \right)^{1/p} t^{2/p} \tag{28}$$

We make use of the density profile (Equation (26)) again in order the calculate the visual extinction as a function of the radius (and consequently time given Equation (28)). The visual extinction is proportional to the atomic hydrogen column density (N_H) as given by Güver et al. (2009):

$$A_V(r) = A_{V,0} + \frac{N_H(r)}{2.21 \cdot 10^{21} \text{cm}^{-3}} \tag{29}$$

where $A_{V,0} = 10$ is the visual extinction at r_0 that accounts for the rare material

further out. The column density is simply obtained by integrating the number density profile along the radius. The radial temperature profile follows a power-law too (Hartmann 2008):

$$T(r) = T_0 \left(\frac{r}{r_0} \right)^{-q} \tag{30}$$

Here, $T_0 = 10$ K is the temperature at r_0 and $q = \frac{2}{4+\beta} \approx 0.4$ for an optically thin dust envelope. We assume that the gas and dust temperatures are coupled at all time that is reasonable for the high density regime ($\gtrsim 10^5$ cm^{-3}) we deal with (Doty et al. 1997; Jørgensen et al. 2006). During a luminosity burst the temperature is elevated. We keep the intensity of the accretion bursts to be a factor of $\sim$240 as in Visser et al. (2012) that corresponds to changing T_0 from 10 K to 30 K. Substituting the elevated T_0 into Equation (30) gives us the burst temperature at any radii that we can relate to time using Equation (28). We choose the burst frequency and duration to be the same as before, i.e. a 100 yr long accretion burst happens every 10^4 yr. Therefore, we know at what times we have a quiescent or burst phase, and consequently when to use $T_0 = 10$ K or $T_0 = 30$ K to compute the temperature. We append a prestellar phase to the beginning of our simulation with $T_{pre} = 10$ K, $n_{pre} = n_0$ and $\tau_{pre} = 10^6$ yr. The obtained physical structure of our model is shown below on Figure 28.

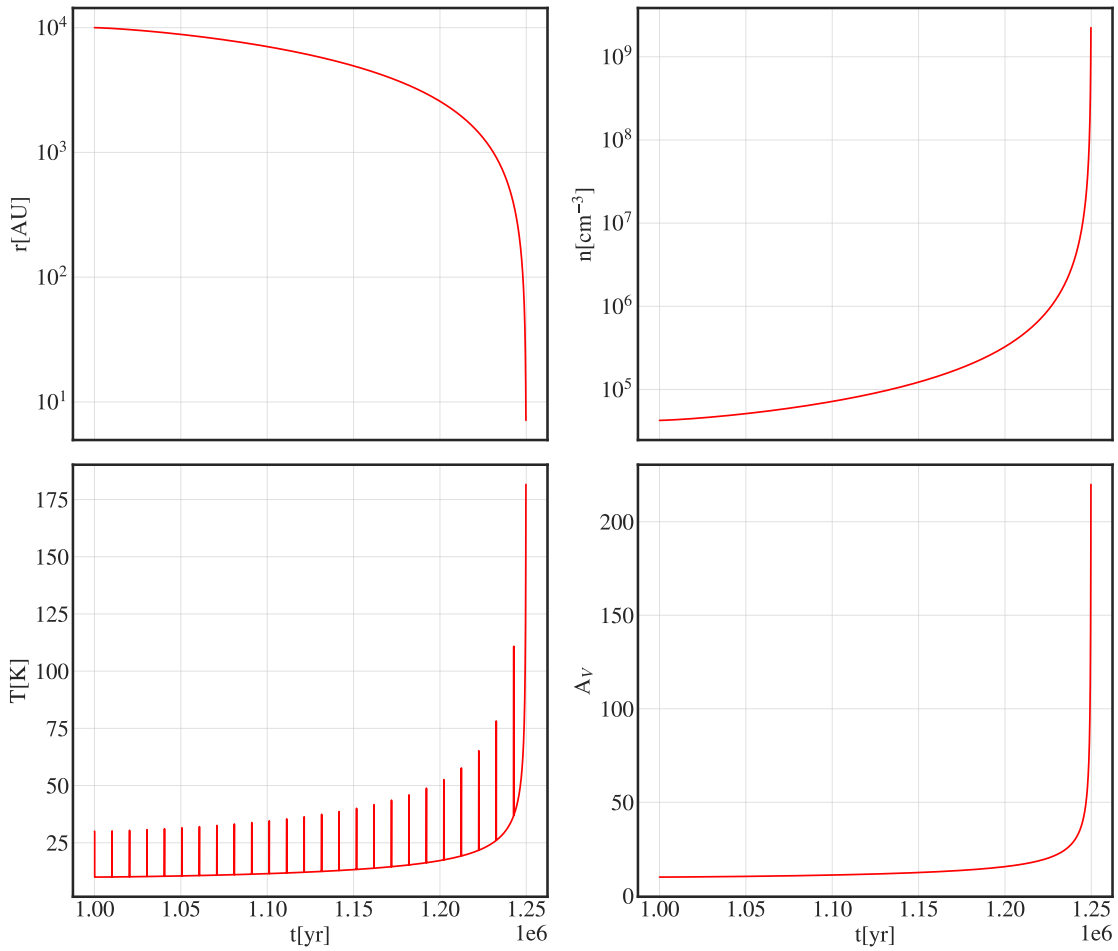

Figure 28: Radius, density, temperature and visual extinction as a function of time during free-fall. The first 10^6 yr of prestellar phase is not shown as all parameters are constant in that epoch.

8.2 Results

After running two models, with and without episodic accretion, we compare the end-time abundances similarly to what we did in Section 6.2. In order to focus on potentially important species, this time, we only show molecules that reach relative abundances over 10^{-14} with respect to H_2 in the bursting model. Our reasoning is that this value matches the observational limit in the millimetre regime (Perotti 2021). Previously, in the case of our static models without infall, methyl formate and formamide were $\sim 10^6$ times more abundant in the bursting model

at the end of the simulations (Figure 15). This time, there is not any species with such prominent ratios, however there are still a handful of species that are $\gtrsim 10^3$ more abundant in the bursting model (Figure 29). Episodic accretion still seems to favour methyl formate formation, however, instead of having a ratio of $\sim 10^6$, it is only more abundant in the episodic accretion model by a factor of $10^2 - 10^3$. This is probably due to the longer simulation times, so the non-burst model can produce more methyl formate, lowering the ratio. The two molecule with the highest ratios, C_{11} and NC_8N, are not detected in the ISM. These species would not be observed even if they did have sufficiently high abundances as they are symmetric molecules that lack a permanent electric dipole moment. An asymmetric and detected species, however, exhibits a relatively high difference between the two models: HC_9N. Its observed relative abundance with respect to molecular hydrogen is $1.05 \cdot 10^{-9}$ towards the Taurus Molecular Cloud, i.e. TMC-1 (Gratier et al. 2016), $7.7 \cdot 10^{-9}$ towards IRC+10216 and $5.3 \cdot 10^{-8}$ towards CRL2688 (Truong-Bach et al. 1993). The latter two sources are the envelopes of asymptotic giant branch (AGB) stars. Our model is only able to reproduce such high abundance in the first half a million years after the protostar is born (Figure 30). Considering that AGB stars are in a late phase of their evolution, the physical conditions in our models resembles the conditions in TMC-1 better. This is especially true during the time our result matches the observations as the quiescent phase temperature and density are low.

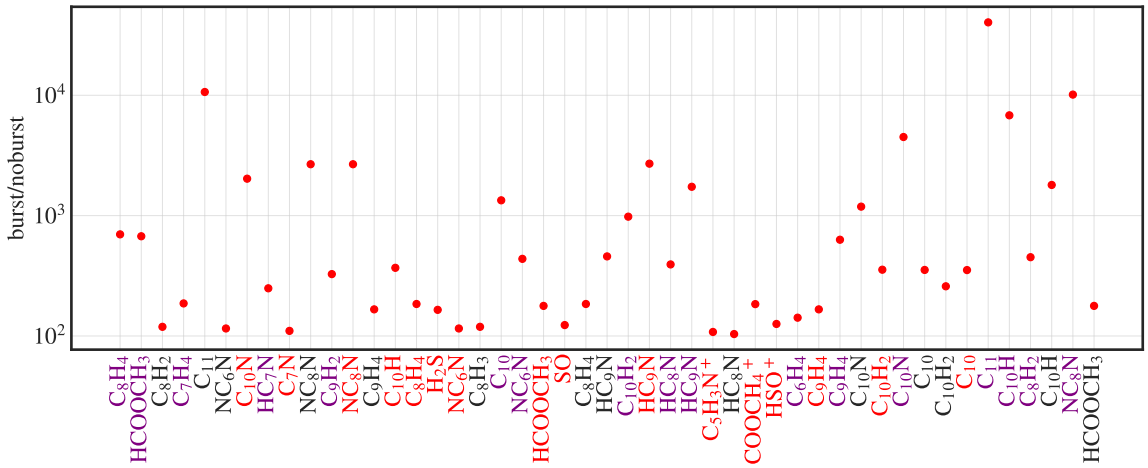

Figure 29: Ratio of the end-time abundances between simulation with and without luminosity bursts. Species in the gas phase, surface layer and mantle are labeled with red, black and purple colours, respectively. We focus on species that have a ratio bigger than 100 and that reach a relative abundance higher than 10^{-14} in the simulation with episodic accretion.

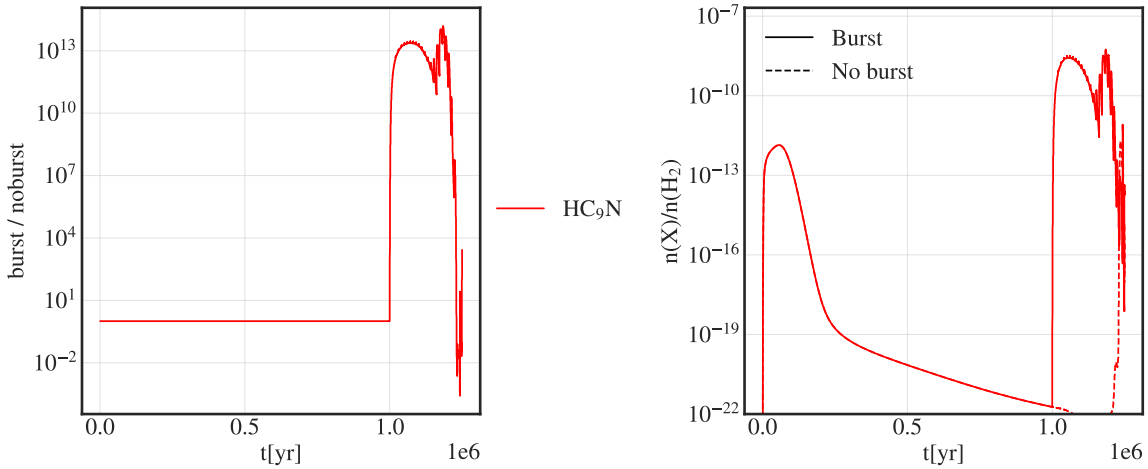

Figure 30: **Left:** Ratio of the abundance of HC_9N in simulation with and without luminosity bursts. **Right:** relative abundance of HC_9N with respect to H_2. Its relative abundance only have the observed values of $10^{-9} - 10^{-8}$ (Gratier et al. 2016; Truong-Bach et al. 1993) in the model with episodic accretion in the, approximately, first half a million years after star formation.

Other then using the end-time abundance ratios between simulations with and without episodic accretion, we also test our models by comparing them with observations of hot corino regions, similarly to what is done in Section 7.2. Relative abundances of O-bearing species are compared to methanol, while N-bearing species are treated with respect to isocyanic acid again. There are a few striking

differences in our results (Figure 31) when compared to our previous predictions shown on Figure 26. Firstly, the end-time abundances are increased for all species in the model without episodic accretion. This is most likely due to the longer simulation time. Additionally, end-time abundances in the non-burst model also grow over the abundances retrieved from the episodic accretion model, except for acetaldehyde and methyl formate. In the case of CH_3CN and CH_2CHCN, the non-burst model results in values that exceed even the observational values by around one order of magnitude. In general, the episodic accretion model seems to better reproduce the relative abundance of most of the studied species with methyl formate only being produced enough in this model, again. N-bearing species now have a much better agreement, too, than they did in our previous predictions. However, neither of our models succeed in forming a sufficient amount of acetaldehyde. This disagreement along with the other good matches suggests an underproduction of acetaldehyde with our chemical network.

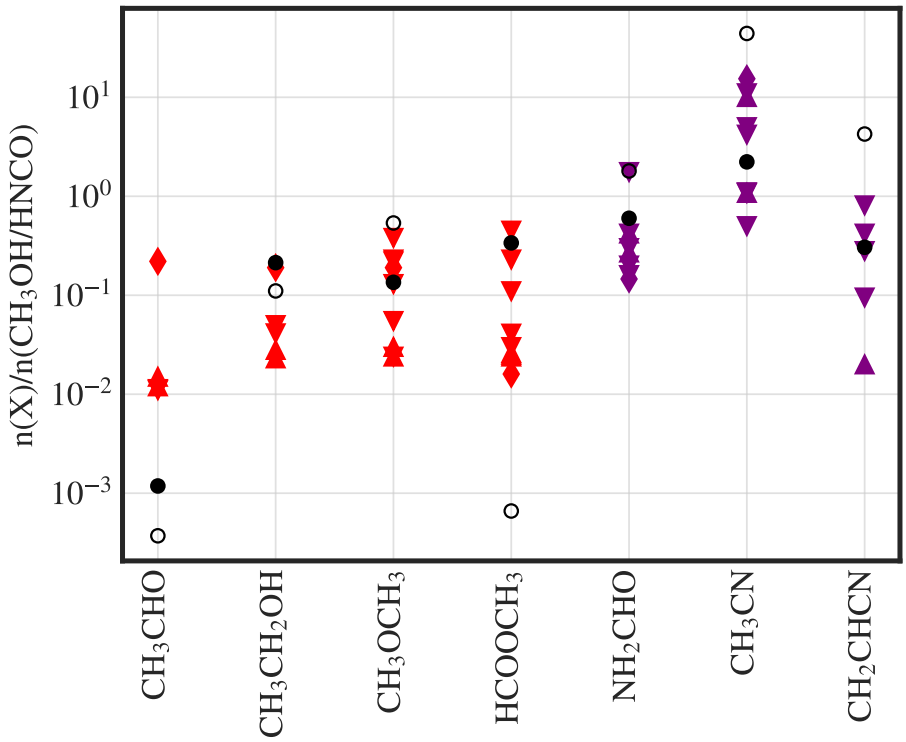

Figure 31: Fractional abundances with respect to methanol (red) or isocyanic acid (purple) for various species. Observational values are represented with down facing triangles for hot corino regions around low-mass protostars, up facing triangles for hot corino regions around low-mass protostars and diamonds for comets as tabulated in Jørgensen et al. (2020). Full circles denote end-time values in our model with episodic accretion, while empty circles do the same for the model without luminosity bursts.

8.3 Summary

We extended our models with an infalling motion in order to make more realistic comparisons with observations of hot corino regions. Our new physical model consisted of two phases: a static prestellar phase and a free-fall phase in which we follow the volume of interest on its journey from the edges of a protostellar envelope (10000 AU) through a general free-fall envelope to the hot inner regions (10 AU). After deriving the physical structure, we compared our models with and without episodic accretion to each other as well as to observations. The end-time abundances between the two models did not exhibit as high ratios as $\sim 10^6$ like in our models without infall (see on Figure 15). However, ratios of $\sim 10^3$ were still

present, for example in the case of HC_9N. Additionally, HC_9N only reached observed relative abundances with respect to H2 in the episodic accretion model. We predicted in Section 7.3 that a coupled model of infall and episodic accretion might better reproduce the fractional abundances of O-bearing and N-bearing species. The results shown on Figure 31 exceeded our expectations as almost all studied species gave better agreements with observations using our new model, even the N-bearing species. We conclude that our general results suggest that episodic accretion does have important effects on the chemistry. What is more, it reproduces observations better with our chemical network.

9 Discussion

Complexity and abundance of molecules carry vital information on the physical environment of the ISM. More and more molecules are being detected that could serve as tracers of the on-going physical processes. Molecular astrophysics is trying to untangle the interplay between the physical environment and chemistry. Star forming regions are of particular interest as many complex species have been detected towards such regions (van Dishoeck 2017). Due to observed patterns in the spatial distribution of different species (see in, for example, Frimann et al. (2017) and Jørgensen et al. (2020, 2015)) and the luminosity problem (see in Evans et al. (2009) and Kenyon et al. (1990)), a new picture of star formation has appeared in the past decades: episodic accretion. This theory suggests that the emerging protostar spends most of its lifetime accreting material with a really low and decreasing rate, with additional short and episodic phases of high accretion rate. During such a phase, the luminosity of the protostar increases thus heating up the surrounding envelope and disk. The temperature of these regions drops after the protostar returns to the quiescent phase. Such variation in temperature might affect the on-going chemical processes and composition. In this thesis, we unraveled the possible astrochemical effects of episodic accretion. We did so by running single-point chemical simulations with various physical models using the Pnautilus software (Ruaud et al. 2016).

First, we were in need of a physical model and a good chemical network. In **Chapter 4**, we started in the footsteps of Visser et al. (2012) and investigated how five prominent and well studied species (CO, N_2, H_3^+, HCO^+ and NH_2^+) reacted to changes in temperature due to episodic accretion. The temperature range was chosen in a way that CO and N_2 would freeze-out onto the grain surfaces during the quiescent phases but they would be evaporated during luminosity bursts. The abundances of the other three species are highly dependent on how much CO and N_2 are present in the system, making this set up a good test for the effects of episodic accretion. Comparing our results with that of Visser et al. (2012) helped us

in choosing a chemical database to be used in our study. We chose KIDA (Wakelam et al. 2012) as it contains more information on grain surface reactions and freeze-out and evaporation processes than UMIST (McElroy et al. 2013) does.

In **Chapter 5**, we put our chemical network to a statistical test before investigating the importance of density and other physical parameters. We aimed to obtain the uncertainty on the abundances caused by the uncertainties on the reaction rates. We approached this problem with a Monte Carlo method and ran 2000 different simulations with the same underlying physical environment but with different reaction rates for all reactions drawn from corresponding distributions. By comparing the end-time abundances we found that the median 1σ uncertainty of our simulations is less than one order of magnitude. The species of interest throughout our project had uncertainties below or around this mean value.

Even though the five main species, that we started our study with, are important and the variation in their abundances could explain the snowline problem, we turned our attention towards other molecules, especially COMs, in **Sections 6.1 and 6.2**. Such molecules could be important in the formation of life as they are precursors of prebiotic molecules (Coutens et al. 2018). The simplest COM is methanol that mainly forms on grain surfaces (Garrod et al. 2006; Watanabe et al. 2002). We started our analyses with this species and found that episodic accretion accelerates its early formation, however the varying temperature seemed to favour its destruction and consequently the formation of other complex organics, such as methyl formate, in the long run. Methyl formate is mainly formed from the reaction of two members of the methanol chain: CH_3O and HCO. We found that our model with episodic accretion produced $\sim 10^6$ times more methyl formate than the model without luminosity bursts, indicating the significance of episodic accretion. There was also another species, formamide, that has gone through a similar experience. In **Section 6.3**, we ran models with different densities, burst temperatures, burst frequencies and prestellar phases in order to understand how different physical parameters affect the chemistry. The main parameters of our fiducial model were $n = 10^5$ cm^{-3}, $T_b = 30$ K, $\tau_q = 10^4$ yr and it was without a prestellar phase. The

freeze-out processes mainly depend on the density and burst frequency. A higher density accelerates the freezing-out of the molecules while rarer bursts offer more time for the gas phase species to freeze-out. The abundance ratios of solid phase methanol and other members of the methanol chain were affected by these two parameters in a similar way. The prestellar phase also altered the aforementioned ratios by decreasing them with increasing prestellar phase duration. Besides that, we noted that formic acid could be a good tracer of the prestellar duration as its ratios with methyl formate and formamide grew above unity with longer prestellar phases. The temperature of bursts affected methyl formate and formamide the most. This is due to the fact that the formation of these species kicks in at temperatures around $13 - 15$ K (Chuang et al. 2016). The methanol chain was not affected as much as methyl formate. We argue that the most important parameters of episodic accretion are the burst temperature and frequency. A parallel study of the two parameters might shed more light on their relation and significance, however that is up for future works as we decided to compare our models with simulations and to improve our model with infalling motion instead.

Subsequently, we compared our models with and without episodic accretion to observations in **Chapter 7**. Our standard model placed the volume of interest in the outskirts of a general protostellar envelope. In such regions, most neutral species stay on the grain surfaces. Observing solid phase molecules in the ISM is demanding as one cannot rely on rotational transitions. However, there are a few observations that have been made towards star forming regions with bright background sources (Boogert et al. 2015; Perotti 2021). The most complex species that has securely been identified is methanol. We showed that our model with episodic accretion gave, in general, a better agreement with ice observations. Especially for the abundance ratios of H_2CO to water ice, CO gas to CO ice and methanol ice to CO ice. In a few other cases, the burst model had similar or worse matches with observations than the non-burst model. Both of our models failed to reproduce the methanol gas-to-ice ratio suggesting that our model did not produce enough gas phase methanol. As our maximum temperature is below the evaporation temper-

ature of methanol, this is somewhat expected. In order to increase the methanol gas-to-ice ratio, some kind of desorption mechanism needed to be enhanced. This could happen due to a chock wave, an outflow or an enhanced irradiation fields as observed by Perotti (2021). We tested this idea by increasing the burst temperature, i.e. enhancing the thermal evaporation rate during bursts, that resulted in a higher methanol gas-to-ice ratio. In order to compare our results with observations of hot corino regions we assumed that the overall ratios of related species do not change during the infalling motion. In general, we concluded again that the model with episodic accretion gave better agreements with observations. Some N-bearing species, however, seemed to show an opposing behaviour. Increasing the burst temperature or density improved the matches with observations which suggested that a model that couples infall and episodic accretion would reproduce observational values even better.

Finally, in **Chapter 8**, we extended our model by introducing a simple infalling motion. After a prestellar phase, we assumed that the volume of interest would free-fall towards the protostar through a general free-fall envelope. We again had two models: one with and another one without episodic accretion. The end-time abundances did not show as large differences between the two models as in Section 6.2, however there were still some remarkable results. A previously not considered molecule, HC_9N, seemed to only reach observed abundances in the model with episodic accretion. Though this does not necessarily mean that our episodic accretion model mirrors reality as another chemical network might produce enough HC_9N without accretion bursts. However, most of the relative abundances of other species showed better agreements with observations as well, suggesting that the episodic accretion model is indeed better than the non-episodic accretion model. The matches were even better than what we had predicted from our models without infall as the previously mismatching N-bearing species were also well in the observed ranges for the bursting model.

In **conclusion**, we explored different physical models of star formation in order to shed light on the possible chemical effects of episodic accretion. We showed that

a varying temperature could affect the gas phase abundance of simple molecules as CO and N_2 by evaporating them from the grain surfaces, and how this affected the abundance of related species. These changes in relative abundances are often used as direct or indirect chemical tracers of episodic accretion (Jørgensen et al. 2020, 2015). We also demonstrated how significantly episodic accretion changed the abundance of more complex molecules, e.g. methyl formate and formamide, resulting in better agreements with observations. Further studies of other COMs suggested that our episodic accretion model, with the chemical network of our choice, was more likely to reproduce observations, especially if an infalling motion was included in the model. However, we note that the chemical network we used lacked certain reactions and species, for example conformers of methyl formate.

We conclude that the magnitude and frequency of accretion burst are the two most important parameters of episodic accretion. We recommend studying the importance of these parameters in **future works** as well as considering the expansion of the chemical network we used. So far, only a few sources have fully been characterised in terms of their gas phase inventories by observations (Jørgensen et al. 2020). This has been a limitation in this study as it restricted the number of molecules and measurements that we were able to use for comparing model and real life values. Therefore, future observations of multiple new sources – by, for example, the recently launched and soon operational James Webb Space Telescope – will potentially help to overcome the challenges faced in this study, and help us further understanding of star formation.

References

El-Abd, Samer J. et al. (Sept. 2019). "Interstellar Glycolaldehyde, Methyl Formate, and Acetic Acid. I. A Bimodal Abundance Pattern in Star-forming Regions". In: *The Astrophysical Journal* 883.2, p. 129. ISSN: 1538-4357. DOI: 10.3847/1538-4357/ab3646. URL: http://dx.doi.org/10.3847/1538-4357/ab3646 (cit. on pp. 7, 19, 52, 67).

Agúndez, M. et al. (May 2019). "A sensitive λ 3 mm line survey of L483. A broad view of the chemical composition of a core around a Class 0 object". In: 625, A147, A147. DOI: 10.1051/0004-6361/201935164. arXiv: 1904.06565 [astro-ph.GA] (cit. on p. 58).

ALMA Partnership et al. (July 2015). "The 2014 ALMA Long Baseline Campaign: First Results from High Angular Resolution Observations toward the HL Tau Region". In: 808.1, L3, p. L3. DOI: 10.1088/2041-8205/808/1/L3. arXiv: 1503.02649 [astro-ph.SR] (cit. on p. 11).

Alves, Felipe O. et al. (Nov. 2020). "A Case of Simultaneous Star and Planet Formation". In: 904.1, L6, p. L6. DOI: 10.3847/2041-8213/abc550. arXiv: 2010.15135 [astro-ph.EP] (cit. on p. 11).

An, Deokkeun et al. (July 2017). "Abundant Methanol Ice toward a Massive Young Stellar Object in the Central Molecular Zone". In: 843.2, L36, p. L36. DOI: 10.3847/2041-8213/aa7cfe. arXiv: 1707.03120 [astro-ph.GA] (cit. on pp. 63, 64).

Arce, Héctor G. et al. (Sept. 2013). "ALMA Observations of the HH 46/47 Molecular Outflow". In: 774.1, 39, p. 39. DOI: 10.1088/0004-637X/774/1/39. arXiv: 1304.0674 [astro-ph.SR] (cit. on p. 16).

Bacmann, A. et al. (May 2012). "Detection of complex organic molecules in a prestellar core: a new challenge for astrochemical models". In: 541, L12, p. L12. DOI: 10.1051/0004-6361/201219207 (cit. on p. 58).

Ballesteros-Paredes, Javier et al. (June 2020). "From Diffuse Gas to Dense Molecular Cloud Cores". In: 216.5, 76, p. 76. DOI: 10.1007/s11214-020-00698-3. arXiv: 2006.01326 [astro-ph.GA] (cit. on p. 10).

Boogert, A. C. Adwin, Perry A. Gerakines, and Douglas C. B. Whittet (Aug. 2015). "Observations of the icy universe." In: 53, pp. 541–581. DOI: 10.1146/annurev-astro-082214-122348. arXiv: 1501.05317 [astro-ph.GA] (cit. on pp. 8, 62–64, 70, 83).

Chacón-Tanarro, A. et al. (Mar. 2019). "Dust opacity variations in the pre-stellar core L1544". In: 623, A118, A118. DOI: 10.1051/0004-6361/201833385. arXiv: 1901.02476 [astro-ph.GA] (cit. on p. 59).

Chen, Joseph C. Y. (Apr. 1967). "Theory of Atomic Collisions with Negative Ions: Associative Detachment". In: *Phys. Rev.* 156 (1), pp. 12–25. DOI: 10.1103/PhysRev.156.12. URL: https://link.aps.org/doi/10.1103/PhysRev.156.12 (cit. on p. 17).

Chu, Laurie E. U., Klaus Hodapp, and Adwin Boogert (Dec. 2020). "Observations of the Onset of Complex Organic Molecule Formation in Interstellar Ices". In: 904.2, 86, p. 86. DOI: 10.3847/1538-4357/abbfa5. arXiv: 2010.05917 [astro-ph.GA] (cit. on pp. 63, 64, 66, 70).

Chuang, K. -J. et al. (Jan. 2016). "H-atom addition and abstraction reactions in mixed CO, H_2CO and CH_3OH ices - an extended view on complex organic molecule formation". In: 455.2, pp. 1702–1712. DOI: 10.1093/mnras/stv2288. arXiv: 1606.01049 [astro-ph.GA] (cit. on pp. 56, 83).

Chuang, K. -J. et al. (Feb. 2018). "Reactive Desorption of CO Hydrogenation Products under Cold Pre-stellar Core Conditions". In: 853.2, 102, p. 102. DOI: 10.3847/1538-4357/aaa24e. arXiv: 1806.06215 [astro-ph.GA] (cit. on pp. 19, 32, 45).

Coutens, A. et al. (Apr. 2015). "Detection of glycolaldehyde toward the solar-type protostar NGC 1333 IRAS2A". In: 576, A5, A5. DOI: 10.1051/0004-6361/201425484. arXiv: 1502.00896 [astro-ph.SR] (cit. on pp. 8, 52).

Coutens, A. et al. (Apr. 2018). "Chemical modelling of glycolaldehyde and ethylene glycol in star-forming regions". In: 475.2, pp. 2016–2026. DOI: 10.1093/mnras/stx3335. arXiv: 1712.08778 [astro-ph.SR] (cit. on pp. 6, 82).

Doty, Steven D. and David A. Neufeld (Nov. 1997). "Models for Dense Molecular Cloud Cores". In: 489.1, pp. 122–142. DOI: 10.1086/304764. arXiv: astro-ph/9707171 [astro-ph] (cit. on p. 74).

Draine, B.T. (2003). "Interstellar Dust Grains". In: *Annual Review of Astronomy and Astrophysics* 41.1, pp. 241–289. DOI: 10.1146/annurev.astro.41.011802.094840. URL: https://doi.org/10.1146/annurev.astro.41.011802.094840 (cit. on pp. 28, 31).

Drozdovskaya, Maria N. et al. (Nov. 2019). "Ingredients for solar-like systems: protostar IRAS 16293-2422 B versus comet 67P/Churyumov-Gerasimenko". In: 490.1, pp. 50–79. DOI: 10.1093/mnras/stz2430. arXiv: 1908.11290 [astro-ph.SR] (cit. on p. 6).

Evans Neal J., II et al. (Apr. 2009). "The Spitzer c2d Legacy Results: Star-Formation Rates and Efficiencies; Evolution and Lifetimes". In: 181.2, pp. 321–350. DOI: 10.1088/0067-0049/181/2/321. arXiv: 0811.1059 [astro-ph] (cit. on pp. 8, 11, 13, 81).

Ferrero, Stefano et al. (Nov. 2020). "Binding Energies of Interstellar Molecules on Crystalline and Amorphous Models of Water Ice by Ab Initio Calculations". In: 904.1, 11, p. 11. DOI: 10.3847/1538-4357/abb953. arXiv: 2009.09763 [astro-ph.GA] (cit. on p. 20).

Frimann, Søren et al. (2016). "Protostellar accretion traced with chemistry - Comparing synthetic C18O maps of embedded protostars to real observations". In: *A&A* 587, A60. DOI: 10.1051/0004-6361/201527622. URL: https://doi.org/10.1051/0004-6361/201527622 (cit. on p. 14).

Frimann, Søren et al. (June 2017). "Protostellar accretion traced with chemistry. High-resolution $C^{18}O$ and continuum observations towards deeply embedded protostars in Perseus". In: 602, A120, A120. DOI: 10.1051/0004-6361/201629739. arXiv: 1703.10225 [astro-ph.SR] (cit. on pp. 14, 15, 44, 81).

Garrod, Robin T. (Mar. 2013). "A Three-phase Chemical Model of Hot Cores: The Formation of Glycine". In: 765.1, 60, p. 60. DOI: 10.1088/0004-637X/765/1/60. arXiv: 1302.0688 [astro-ph.GA] (cit. on p. 67).

Garrod, Robin T. et al. (Jan. 2006). "Are gas-phase models of interstellar chemistry tenable? The case of methanol". In: *Faraday Discussions* 133, p. 51. DOI: 10.1039/b516202e (cit. on pp. 19, 32, 45, 82).

Gratier, P. et al. (Aug. 2016). "A New Reference Chemical Composition for TMC-1". In: 225.2, 25, p. 25. DOI: 10.3847/0067-0049/225/2/25. arXiv: 1610.00524 [astro-ph.GA] (cit. on pp. 76, 77).

Güver, Tolga and Feryal Özel (Dec. 2009). "The relation between optical extinction and hydrogen column density in the Galaxy". In: 400.4, pp. 2050–2053. DOI: 10.1111/j.1365-2966.2009.15598.x. arXiv: 0903.2057 [astro-ph.GA] (cit. on p. 73).

Hartmann, Lee (2008). *Accretion Processes in Star Formation*. 2nd ed. Cambridge Astrophysics. Cambridge University Press. DOI: 10.1017/CBO9780511552090 (cit. on pp. 10–12, 72–74).

Henning, Thomas (Sept. 2010). "Cosmic Silicates". In: 48, pp. 21–46. DOI: 10.1146/annurev-astro-081309-130815 (cit. on p. 10).

Herbst, Eric and Ewine F. van Dishoeck (Sept. 2009). "Complex Organic Interstellar Molecules". In: 47.1, pp. 427–480. DOI: 10.1146/annurev-astro-082708-101654 (cit. on p. 10).

Hsieh, Tien-Hao et al. (Oct. 2019). "Chronology of Episodic Accretion in Protostars—An ALMA Survey of the CO and H_2O Snowlines". In: 884.2, 149, p. 149. DOI: 10.3847/1538-4357/ab425a. arXiv: 1909.02706 [astro-ph.GA] (cit. on pp. 41, 44).

Jiménez-Serra, Izaskun et al. (Oct. 2016). "The Spatial Distribution of Complex Organic Molecules in the L1544 Pre-stellar Core". In: 830.1, L6, p. L6. DOI: 10.3847/2041-8205/830/1/L6. arXiv: 1609.05045 [astro-ph.SR] (cit. on p. 58).

Jiménez-Serra, Izaskun et al. (Aug. 2021). "The Complex Organic Molecular Content in the L1498 Starless Core". In: 917.1, 44, p. 44. DOI: 10.3847/1538-4357/ac024c. arXiv: 2105.08363 [astro-ph.SR] (cit. on p. 58).

Johnstone, Doug et al. (Mar. 2013). "Continuum Variability of Deeply Embedded Protostars as a Probe of Envelope Structure". In: 765.2, 133, p. 133. DOI: 10.1088/0004-637X/765/2/133. arXiv: 1301.7341 [astro-ph.SR] (cit. on p. 15).

Jørgensen, J. K., Arnaud Belloche, and Robin T. Garrod (Aug. 2020). "Astrochemistry During the Formation of Stars". In: 58, pp. 727–778. DOI: 10.1146/annurev-astro-032620-021927. arXiv: 2006.07071 [astro-ph.SR] (cit. on pp. 6, 8, 10, 16, 67–69, 79, 81, 85).

Jørgensen, J. K. et al. (Apr. 2006). "The effect of a strong external radiation field on protostellar envelopes in Orion". In: 449.2, pp. 609–619. DOI: 10.1051/0004-6361:20053011. arXiv: astro-ph/0512314 [astro-ph] (cit. on p. 74).

Jørgensen, J. K. et al. (July 2015). "Molecule sublimation as a tracer of protostellar accretion. Evidence for accretion bursts from high angular resolution $C^{18}O$ images". In: 579, A23, A23. DOI: 10.1051/0004-6361/201425317. arXiv: 1504.02974 [astro-ph.SR] (cit. on pp. 8, 14, 15, 44, 81, 85).

Jørgensen, J. K. et al. (Dec. 2018). "The ALMA-PILS survey: isotopic composition of oxygen-containing complex organic molecules toward IRAS 16293-2422B". In: 620, A170, A170. DOI: 10.1051/0004-6361/201731667. arXiv: 1808.08753 [astro-ph.SR] (cit. on p. 50).

Kenyon, Scott J. et al. (Mar. 1990). "An IRAS Survey of the Taurus-Auriga Molecular Cloud". In: 99, p. 869. DOI: 10.1086/115380 (cit. on pp. 8, 13, 81).

Koumpia, E. et al. (July 2017). "The chemical structure of the Class 0 protostellar envelope NGC 1333 IRAS 4A". In: 603, A88, A88. DOI: 10.1051/0004-6361/201630160. arXiv: 1705.00908 [astro-ph.GA] (cit. on p. 41).

López-Sepulcre, Ana et al. (Oct. 2019). "Interstellar Formamide (NH2CHO), a Key Prebiotic Precursor". In: *ACS Earth and Space Chemistry* 3.10, pp. 2122–2137. DOI: 10.1021/acsearthspacechem.9b00154. arXiv: 1909.11770 [astro-ph.SR] (cit. on p. 52).

McElroy, D. et al. (2013). "The UMIST database for astrochemistry 2012". In: *A&A* 550, A36. DOI: 10.1051/0004-6361/201220465. URL: https://doi.org/10.1051/0004-6361/201220465 (cit. on pp. 22, 27, 28, 82).

McKellar, A. (June 1940). "Evidence for the Molecular Origin of Some Hitherto Unidentified Interstellar Lines". In: 52.307, p. 187. DOI: 10.1086/125159 (cit. on p. 16).

Neralwar, K. R. et al. (May 2022). "The SEDIGISM survey: Molecular cloud morphology. II. Integrated source properties". In: *arXiv e-prints*, arXiv:2205.02253, arXiv:2205.02253. arXiv: 2205.02253 [astro-ph.GA] (cit. on p. 10).

Perotti, Giulia (Apr. 2021). "Ice and Gas - Linking Infrared and Millimetric Observations towards young Solar-type Stars". PhD thesis. University of Copenhagen, Denmark (cit. on pp. 35, 62–66, 70, 75, 83, 84).

Perotti, Giulia et al. (Nov. 2020). "Linking ice and gas in the Serpens low-mass star-forming region". In: 643, A48, A48. DOI: 10.1051/0004-6361/202038102. arXiv: 2008.02827 [astro-ph.SR] (cit. on p. 63).

Plunkett, Adele L. et al. (Nov. 2015). "Episodic molecular outflow in the very young protostellar cluster Serpens South". In: 527.7576, pp. 70–73. DOI: 10.1038/nature15702. arXiv: 1511.01100 [astro-ph.SR] (cit. on p. 16).

Pontoppidan, K. M., E. F. van Dishoeck, and E. Dartois (Nov. 2004). "Mapping ices in protostellar environments on 1000 AU scales. Methanol-rich ice in the envelope of Serpens SMM 4". In: 426, pp. 925–940. DOI: 10.1051/0004-6361:20041276. arXiv: astro-ph/0407316 [astro-ph] (cit. on pp. 63, 64).

Quénard, David et al. (Feb. 2018). "Chemical modelling of complex organic molecules with peptide-like bonds in star-forming regions". In: 474.2, pp. 2796–2812. DOI: 10.1093/mnras/stx2960. arXiv: 1711.05184 [astro-ph.SR] (cit. on p. 52).

Raghavan, Deepak et al. (Sept. 2010). "A Survey of Stellar Families: Multiplicity of Solar-type Stars". In: 190.1, pp. 1–42. DOI: 10.1088/0067-0049/190/1/1. arXiv: 1007.0414 [astro-ph.SR] (cit. on p. 16).

Reboussin, L. et al. (June 2014). "Grain-surface reactions in molecular clouds: the effect of cosmic rays and quantum tunnelling". In: 440.4, pp. 3557–3567. DOI: 10.1093/mnras/stu462. arXiv: 1403.5189 [astro-ph.GA] (cit. on p. 24).

Ruaud, Maxime, Valentine Wakelam, and Franck Hersant (Apr. 2016). "Gas and grain chemical composition in cold cores as predicted by the Nautilus three-phase model". In: *Monthly Notices of the Royal Astronomical Society* 459.4, pp. 3756–3767. ISSN: 0035-8711. DOI: 10.1093/mnras/stw887. URL: https://doi.org/10.1093/mnras/stw887 (cit. on pp. 19–21, 23, 25, 27, 29, 43, 81).

Ruaud, Maxime et al. (Jan. 2015). "Modelling complex organic molecules in dense regions: Eley–Rideal and complex induced reaction". In: *Monthly Notices of the Royal Astronomical Society* 447.4, pp. 4004–4017. ISSN: 0035-8711. DOI: 10.1093/mnras/stu2709. URL: https://doi.org/10.1093/mnras/stu2709 (cit. on pp. 19, 24, 27).

Shu, F. H. (June 1977). "Self-similar collapse of isothermal spheres and star formation." In: 214, pp. 488–497. DOI: 10.1086/155274 (cit. on pp. 8, 11, 14).

Simons, M. A. J., T. Lamberts, and H. M. Cuppen (Feb. 2020). "Formation of COMs through CO hydrogenation on interstellar grains". In: 634, A52, A52. DOI: 10.1051/0004-6361/201936522. arXiv: 2001.04895 [astro-ph.SR] (cit. on pp. 32, 45, 47, 48, 51).

Stahler, Steven W. and Francesco Palla (2004). *The Formation of Stars* (cit. on pp. 11, 73).

Swings, P. and L. Rosenfeld (Nov. 1937). "Considerations Regarding Interstellar Molecules". In: 86, pp. 483–486. DOI: 10.1086/143880 (cit. on p. 16).

Truong-Bach, D. Graham, and Nguyen-Q-Rieu (Sept. 1993). "HC9N from the envelopes of IRC +10216 and CRL 2688." In: 277, pp. 133–138 (cit. on pp. 76, 77).

van Dishoeck, Ewine F. (1988). "Molecular Cloud Chemistry". In: *Millimetre and Submillimetre Astronomy: Lectures Presented at a Summer School Held in Stirling, Scotland, June 21–27, 1987*. Ed. by R. D. Wolstencroft and W. B. Burton. Dordrecht: Springer Netherlands, pp. 117–164. ISBN: 978-94-009-3019-3. DOI: 10.1007/978-94-009-3019-3_4. URL: https://doi.org/10.1007/978-94-009-3019-3_4 (cit. on pp. 17–19).

— (2017). "Astrochemistry: overview and challenges". In: *Proceedings of the International Astronomical Union* 13.S332, pp. 3–22. DOI: 10.1017/S1743921317011528 (cit. on pp. 6, 7, 11, 16, 20, 81).

Visser, Ruud and Edwin A. Bergin (July 2012). "FUNDAMENTAL ASPECTS OF EPISODIC ACCRETION CHEMISTRY EXPLORED WITH SINGLE-POINT MODELS". In: *The Astrophysical Journal* 754.1, p. L18. ISSN: 2041-8213. DOI: 10.1088/2041-8205/754/1/l18. URL: http://dx.doi.org/10.1088/2041-8205/754/1/L18 (cit. on pp. 28, 29, 31, 32, 40, 58, 74, 81).

Viti, Serena et al. (Nov. 2004). "Evaporation of ices near massive stars: models based on laboratory temperature programmed desorption data". In: 354.4, pp. 1141–1145. DOI: 10.1111/j.1365-2966.2004.08273.x. arXiv: astro-ph/0406054 [astro-ph] (cit. on p. 12).

Vorobyov, Eduard I. et al. (Aug. 2013). "The effect of episodic accretion on the phase transition of CO and CO2 in low-mass star formation". In: *A&A* 557, A35. DOI: 10.1051/0004-6361/201321775. URL: https://doi.org/10.1051/0004-6361/201321775 (cit. on p. 16).

Wakelam, V., E. Herbst, and F. Selsis (May 2006). "The effect of uncertainties on chemical models of dark clouds". In: 451.2, pp. 551–562. DOI: 10.1051/0004-6361:20054682. arXiv: astro-ph/0601611 [astro-ph] (cit. on pp. 33, 34).

Wakelam, V. et al. (Mar. 2012). "A KINETIC DATABASE FOR ASTROCHEMISTRY (KIDA)". In: *The Astrophysical Journal Supplement Series* 199.1, p. 21. ISSN: 1538-4365. DOI: 10.1088/0067-0049/199/1/21. URL: http://dx.doi.org/10.1088/0067-0049/199/1/21 (cit. on pp. 20, 22, 23, 25–27, 31, 82).

Watanabe, Naoki and Akira Kouchi (June 2002). "Efficient Formation of Formaldehyde and Methanol by the Addition of Hydrogen Atoms to CO in H_2O-CO Ice at 10 K". In: 571.2, pp. L173–L176. DOI: 10.1086/341412 (cit. on pp. 8, 19, 32, 45, 82).

Yamamoto, Satoshi (2017). *Introduction to Astrochemistry: Chemical Evolution from Interstellar Clouds to Star and Planet Formation*. DOI: 10.1007/978-4-431-54171-4 (cit. on pp. 18–20).

Zakri, Wafa et al. (Jan. 2022). "The Rate, Amplitude, and Duration of Outbursts from Class 0 Protostars in Orion". In: *The Astrophysical Journal Letters* 924.2, p. L23. DOI: 10.3847/2041-8213/ac46ae. URL: https://doi.org/10.3847%2F2041-8213%2Fac46ae (cit. on p. 15).

Appendices

A 2 vs 3 phase model

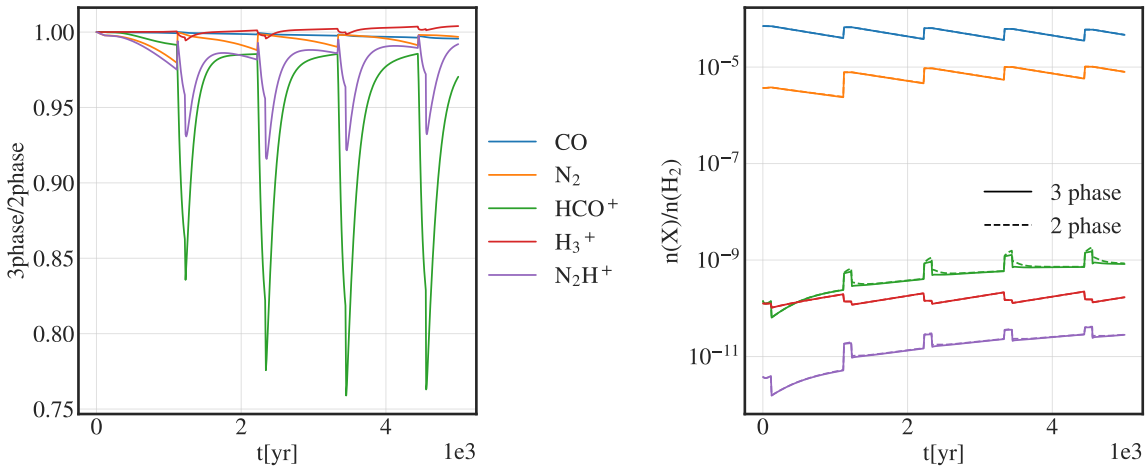

Figure 32: $n = 10^6$ cm^{-3}, $\tau_q = 10^3$yr;

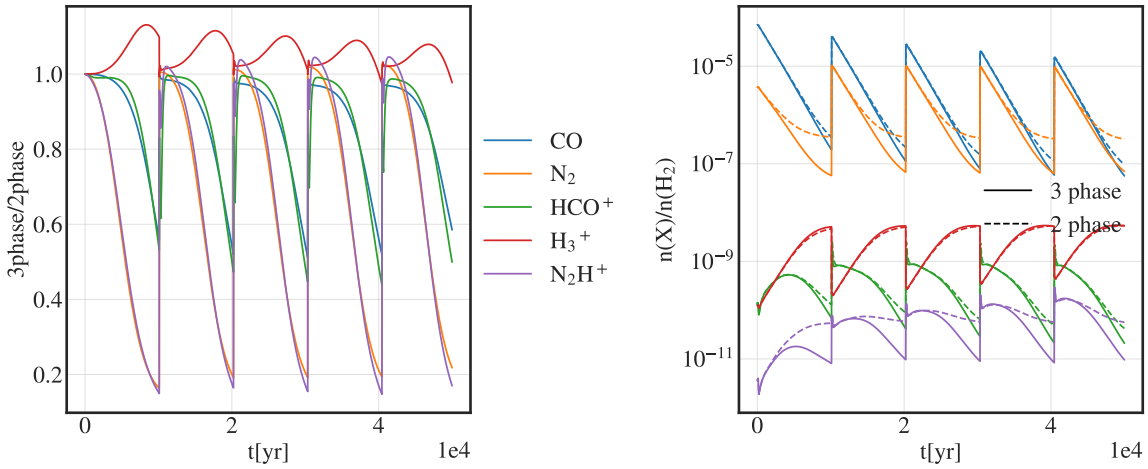

Figure 33: $n = 10^6$ cm^{-3}, $\tau_q = 10^4$yr;

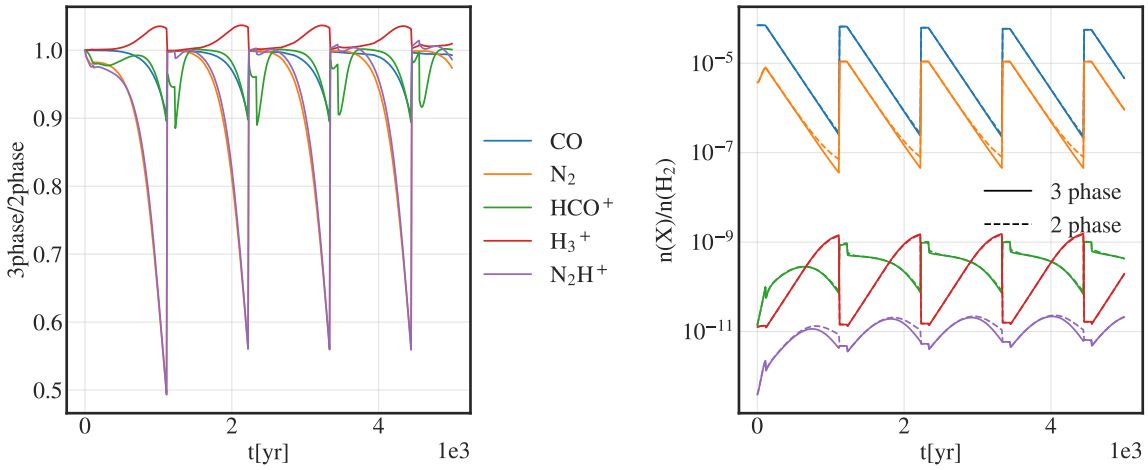

Figure 34: $n = 10^7$ cm^{-3}, $\tau_q = 10^3$yr;

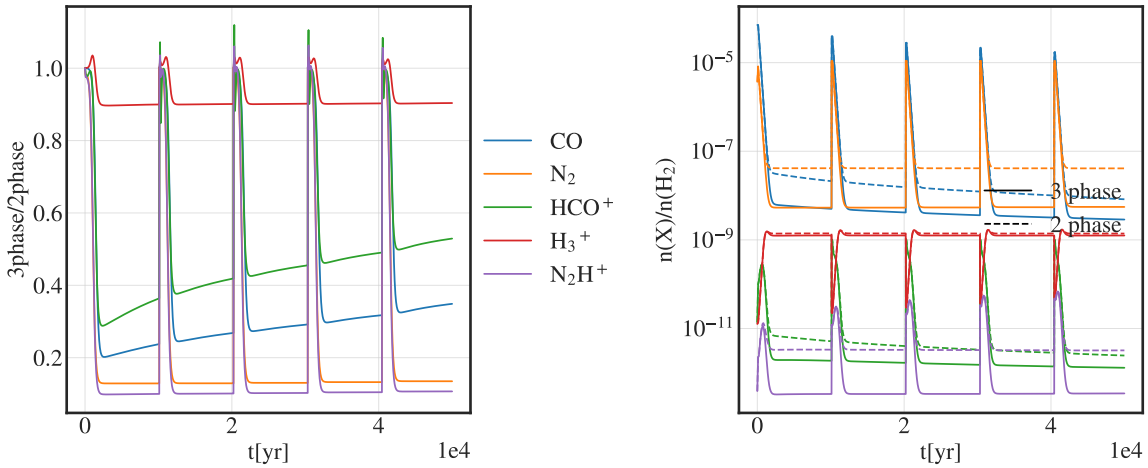

Figure 35: $n = 10^7$ cm^{-3}, $\tau_q = 10^4$yr;

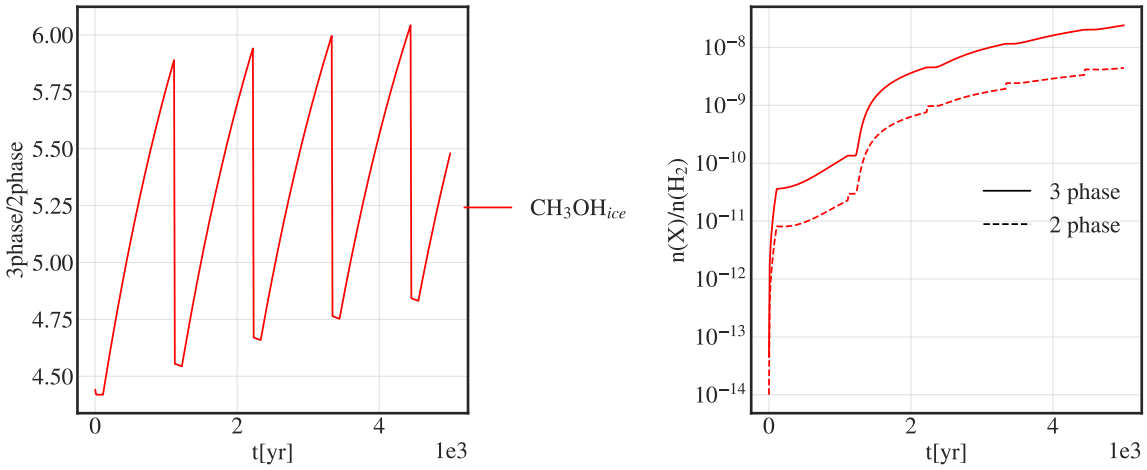

Figure 36: $n = 10^6$ cm^{-3}, $\tau_q = 10^3$yr;

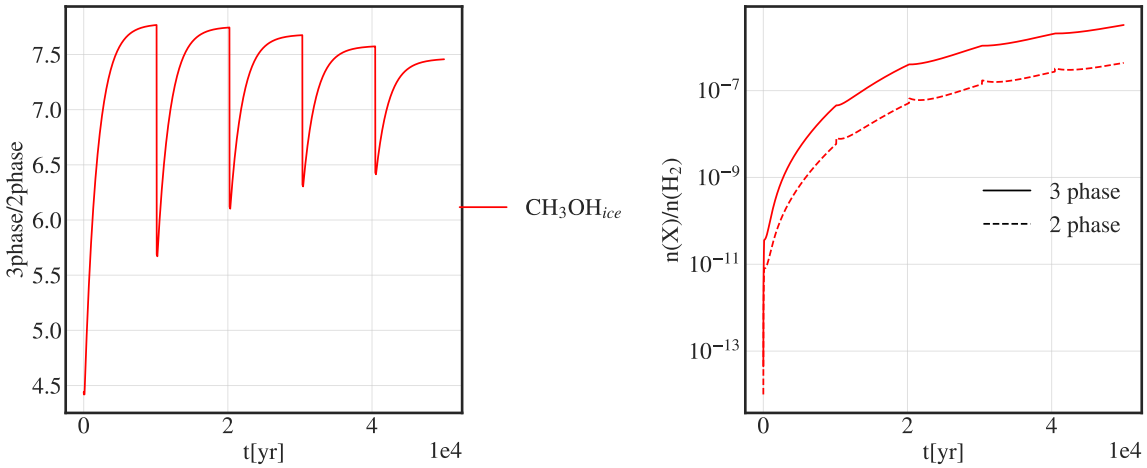

Figure 37: $n = 10^6$ cm^{-3}, $\tau_q = 10^4$yr;

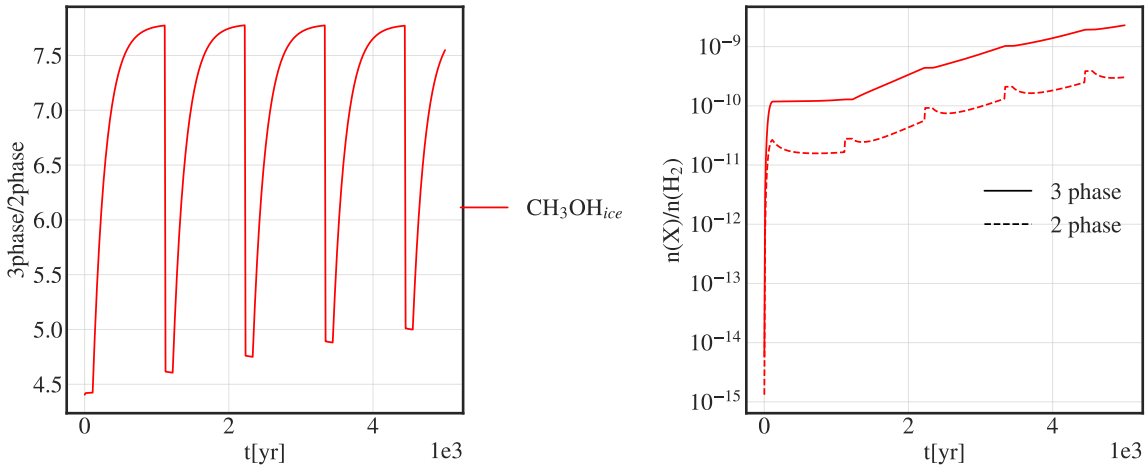

Figure 38: $n = 10^7$ cm^{-3}, $\tau_q = 10^3$yr;

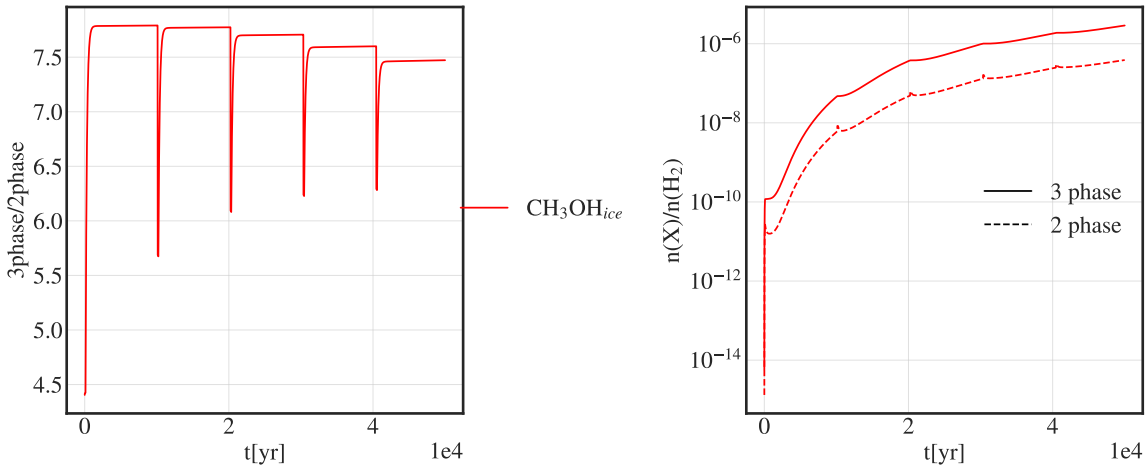

Figure 39: $n = 10^7$ cm^{-3}, $\tau_q = 10^4$yr;

B Methanol chain detailed production and destruction rates

For an easier overview, we only show how the bursts change the rates and do not plot the non-burst reaction rates. Every reaction has its own ID that is used to label them. The reactions with their corresponding IDs are listed below. Only reactions that reaches a minimum of 5% relative rate are shown. We restrain ourselves to plot reactions that have surface layer reactants or products (denoted by an s subscript) since the rates are, in general, significantly higher for such species compared to the mantle layer.

CO_s:

- 7525: $O_s + HCO_s \rightarrow CO_s + OH_s$
- 10899: $H_s + HCO_s \rightarrow CO_s + H_{2s}$
- 9817: $CO \rightarrow CO_s$
- 7345: $H_s + CO_s \rightarrow HCO_s$
- 7773: $CO_s \rightarrow CO$

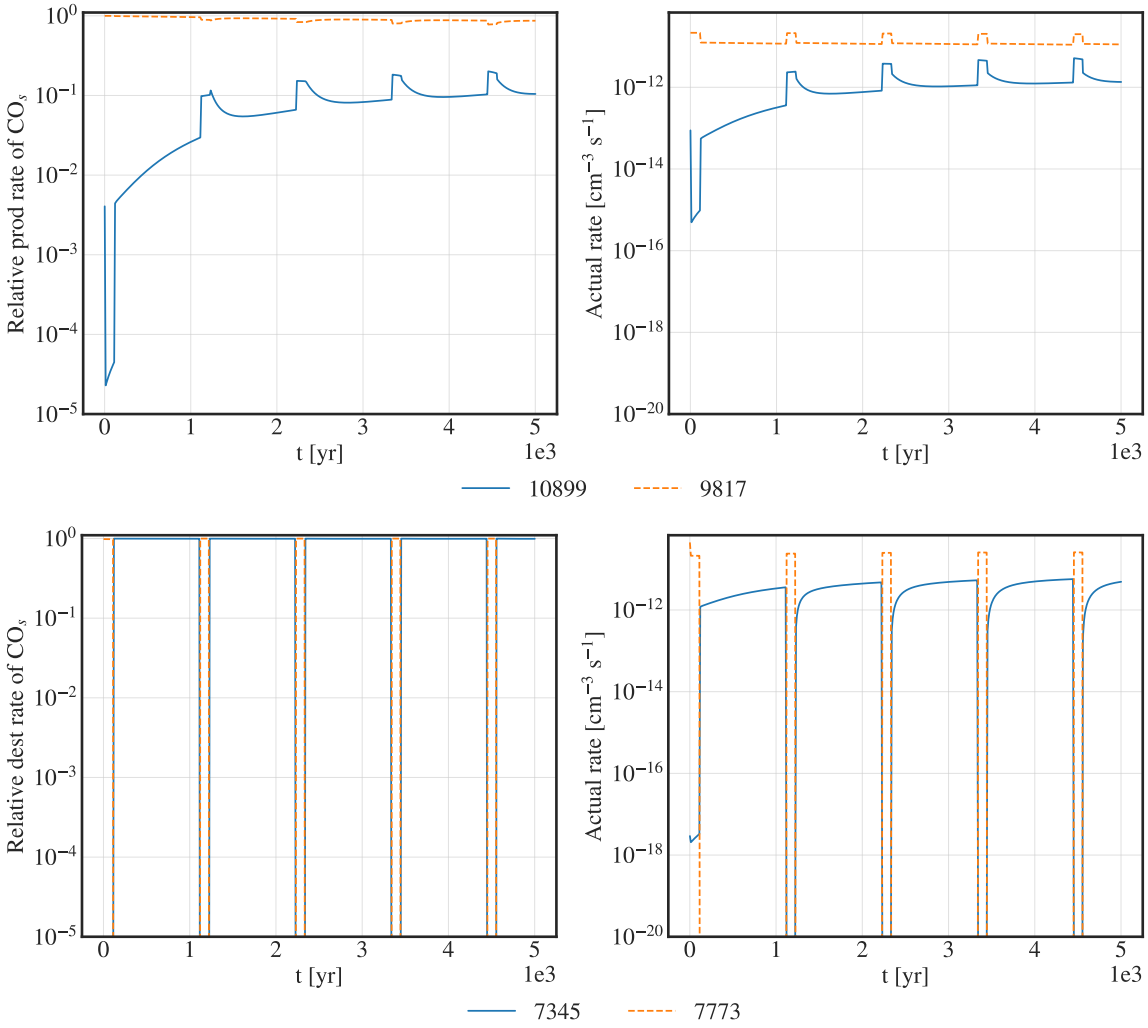

Figure 40: CO_s production (**Top**) and destruction (**Bottom**) rate for $n = 10^5$ cm^{-3} and $\tau_q = 10^3$ yr.

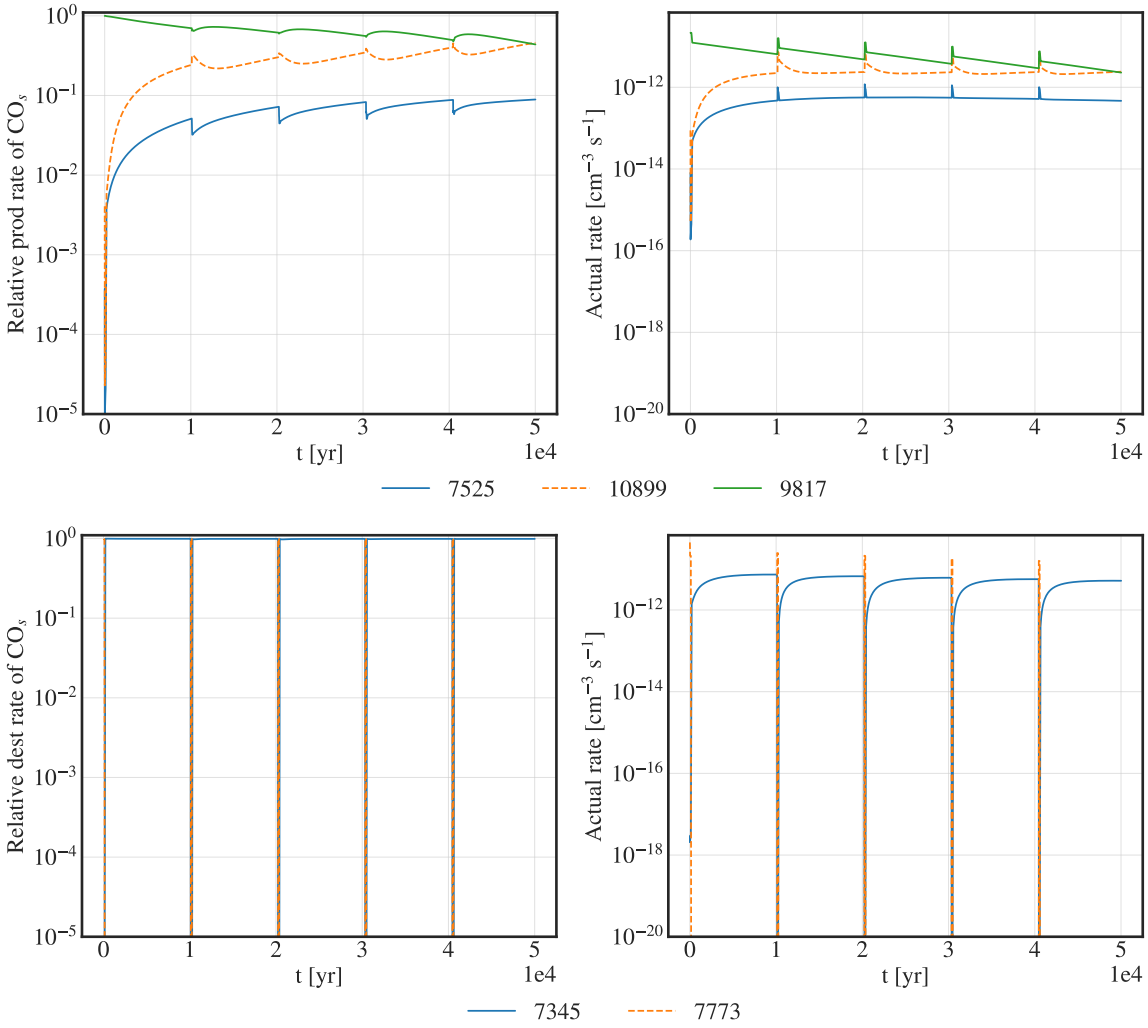

Figure 41: CO_s production (**Top**) and destruction (**Bottom**) rate for $n = 10^5$ cm^{-3} and $\tau_q = 10^4$ yr.

HCO_s:

- 7345: $H_s + CO_s \rightarrow HCO_s$
- 7553: $OH_s + H2CO_s \rightarrow HCO_s + H_2O_s$
- 7585: $H_s + H_2CO_s \rightarrow HCO_s + H_{2s}$
- 8275: $NH_2CHO_s \rightarrow NH_2s + HCO_s$

- 8333: $HCOOCH_{3s} \rightarrow HCO_s + CH_2OH_s$
- 9842: $HCO \rightarrow HCO_s$
- 7361: $H_s + HCO_s \rightarrow H_2CO_s$
- 7505: $NH_{2s} + HCO_s \rightarrow NH_2CHO_s$
- 7523: $O_s + HCO_s \rightarrow CO_{2s} + H_s$
- 7525: $O_s + HCO_s \rightarrow CO_s + OH_s$
- 7555: $OH_s + HCO_s \rightarrow HCOOH_s$
- 10899: $H_s + HCO_s \rightarrow CO_s + H_{2s}$
- 7798: $HCO_s \rightarrow HCO$

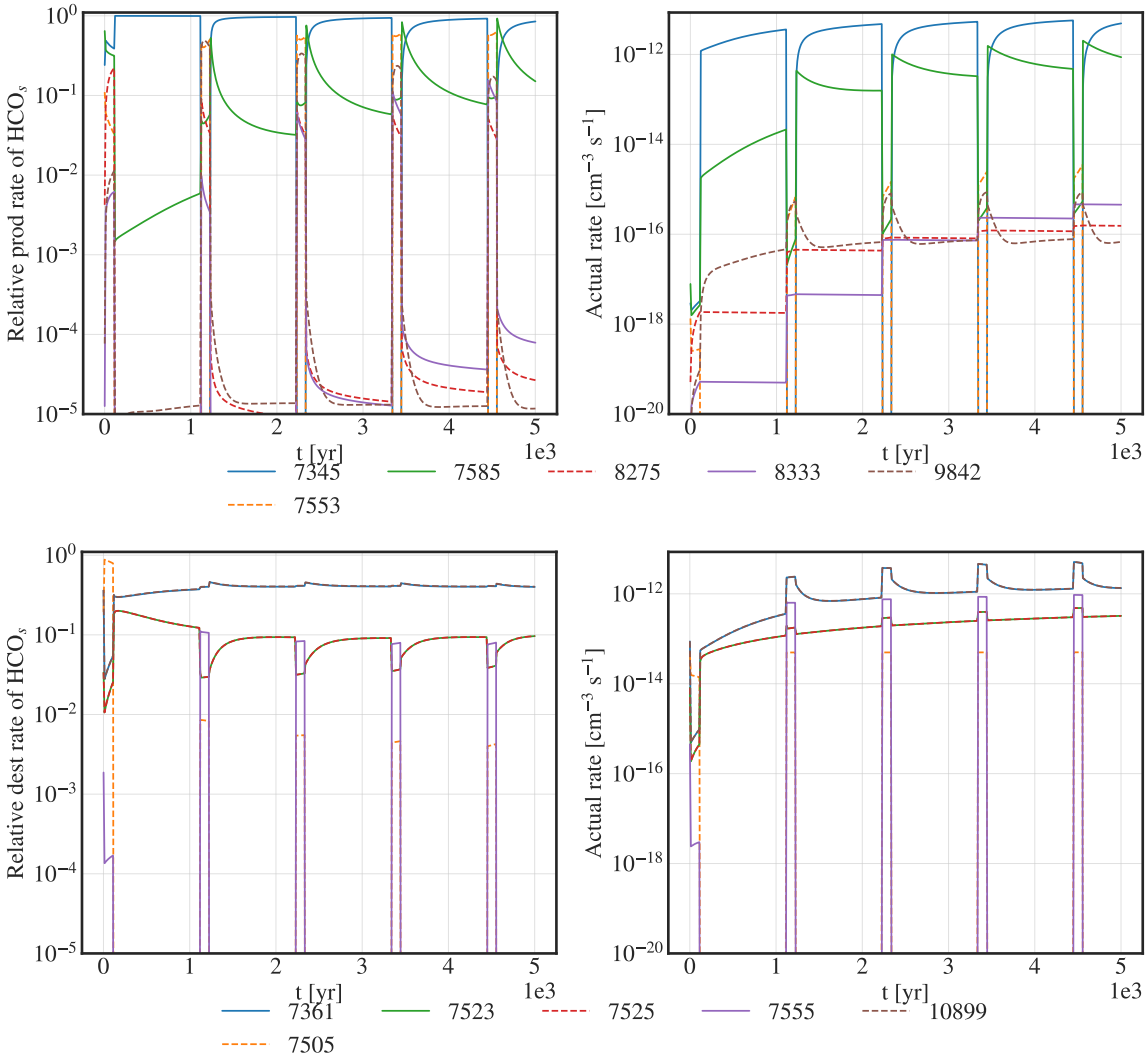

Figure 42: HCO_s production (**Top**) and destruction (**Bottom**) rate for $n = 10^5$ cm^{-3} and $\tau_q = 10^3$ yr.

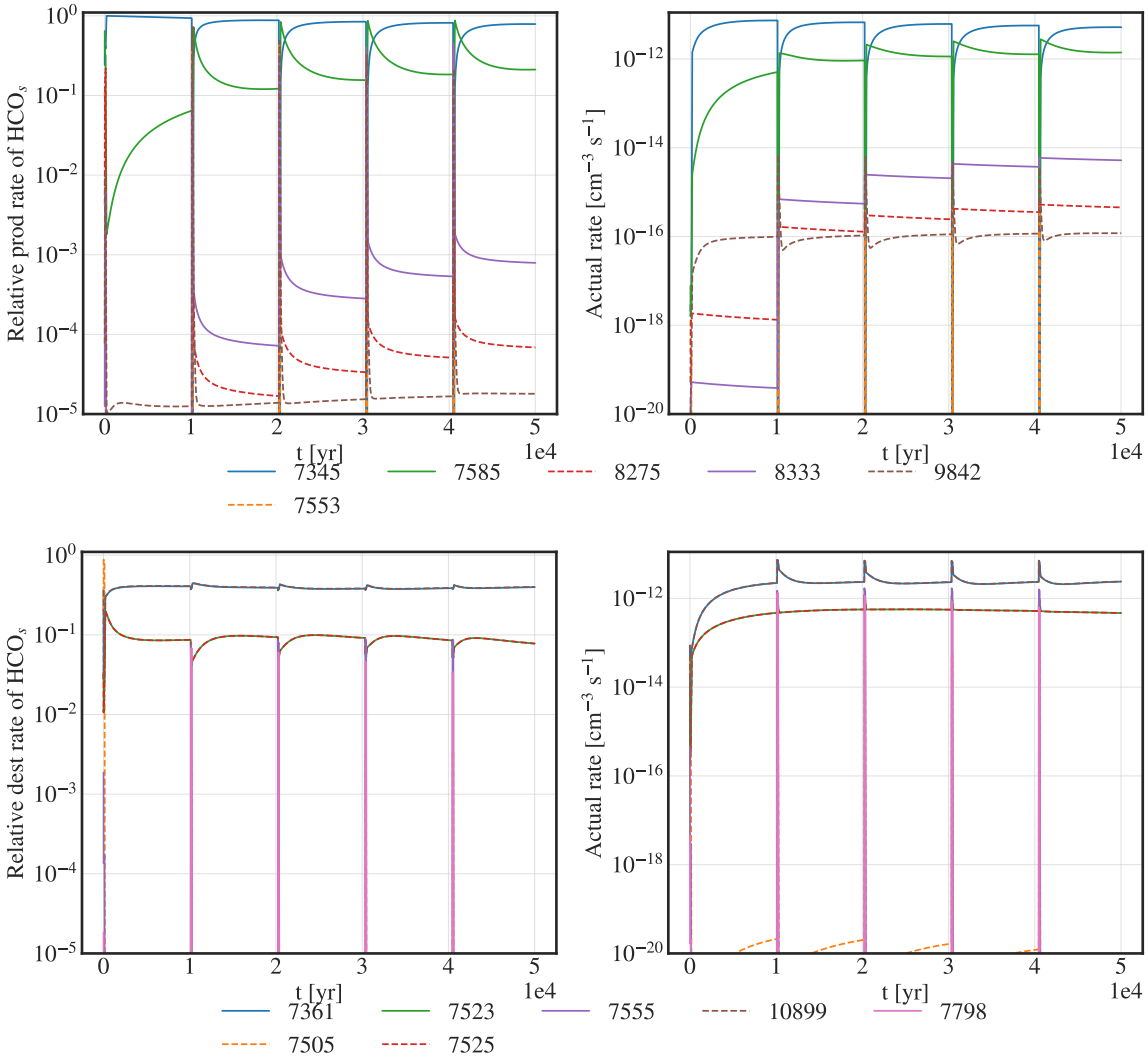

Figure 43: HCO_s production (**Top**) and destruction (**Bottom**) rate for $n = 10^5$ cm^{-3} and $\tau_q = 10^4$ yr.

H_2CO_s:

- 7361: $H_s + HCO_s \rightarrow H_2CO_s$
- 10903: $H_s + CH_3O_s \rightarrow H_2CO + H_{2s}$
- 7553: $OH_s + H_2CO_s \rightarrow HCO_s + H_2O_s$

- 7583: $H_s + H_2CO_s \rightarrow CH_3O_s$
- 7585: $H_s + H_2CO_s \rightarrow HCO_s + H_{2s}$
- 8240: $H_2CO_s \rightarrow CO_s + H_{2s}$

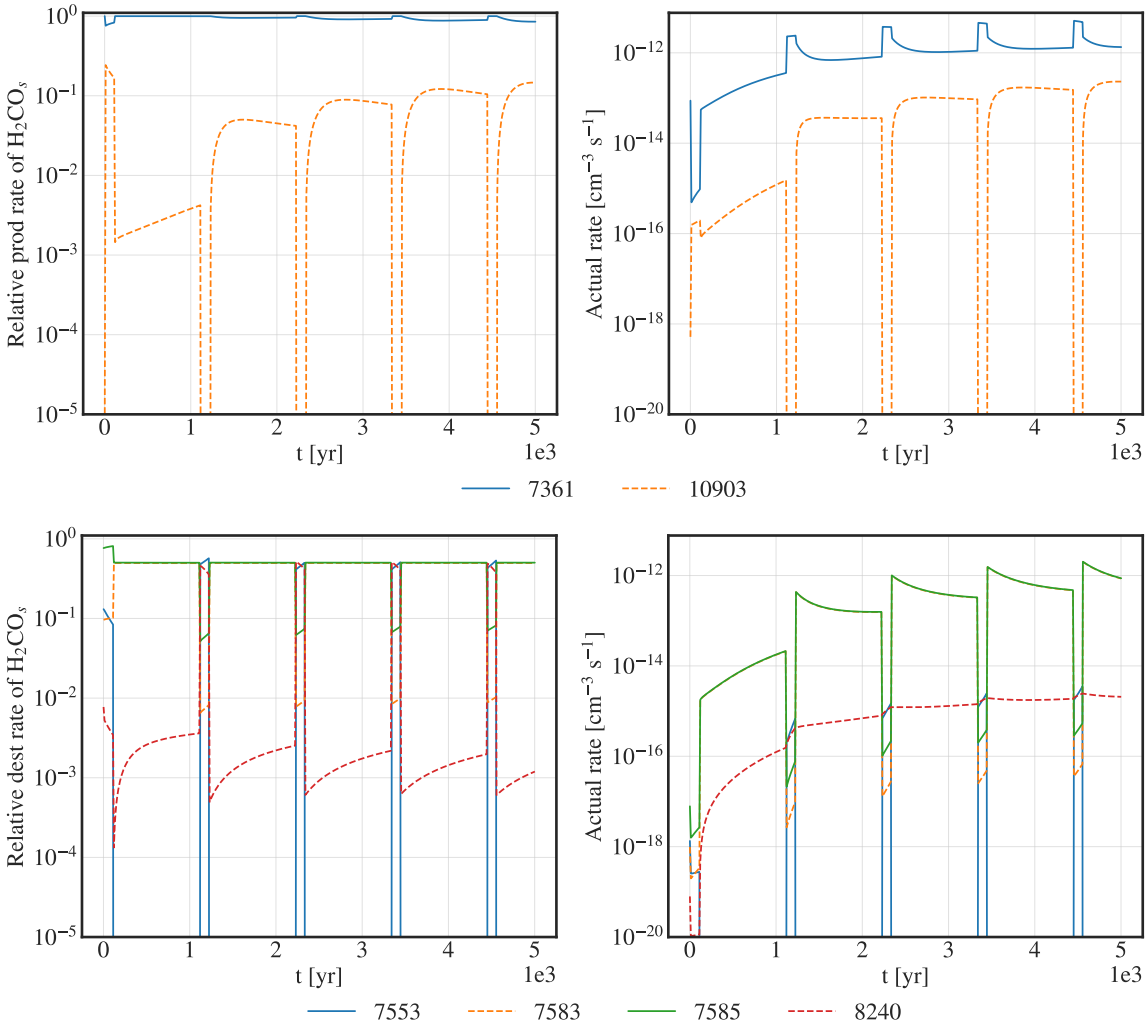

Figure 44: H_2CO_s production (**Top**) and destruction (**Bottom**) rate for $n = 10^5$ cm^{-3} and $\tau_q = 10^3$ yr.

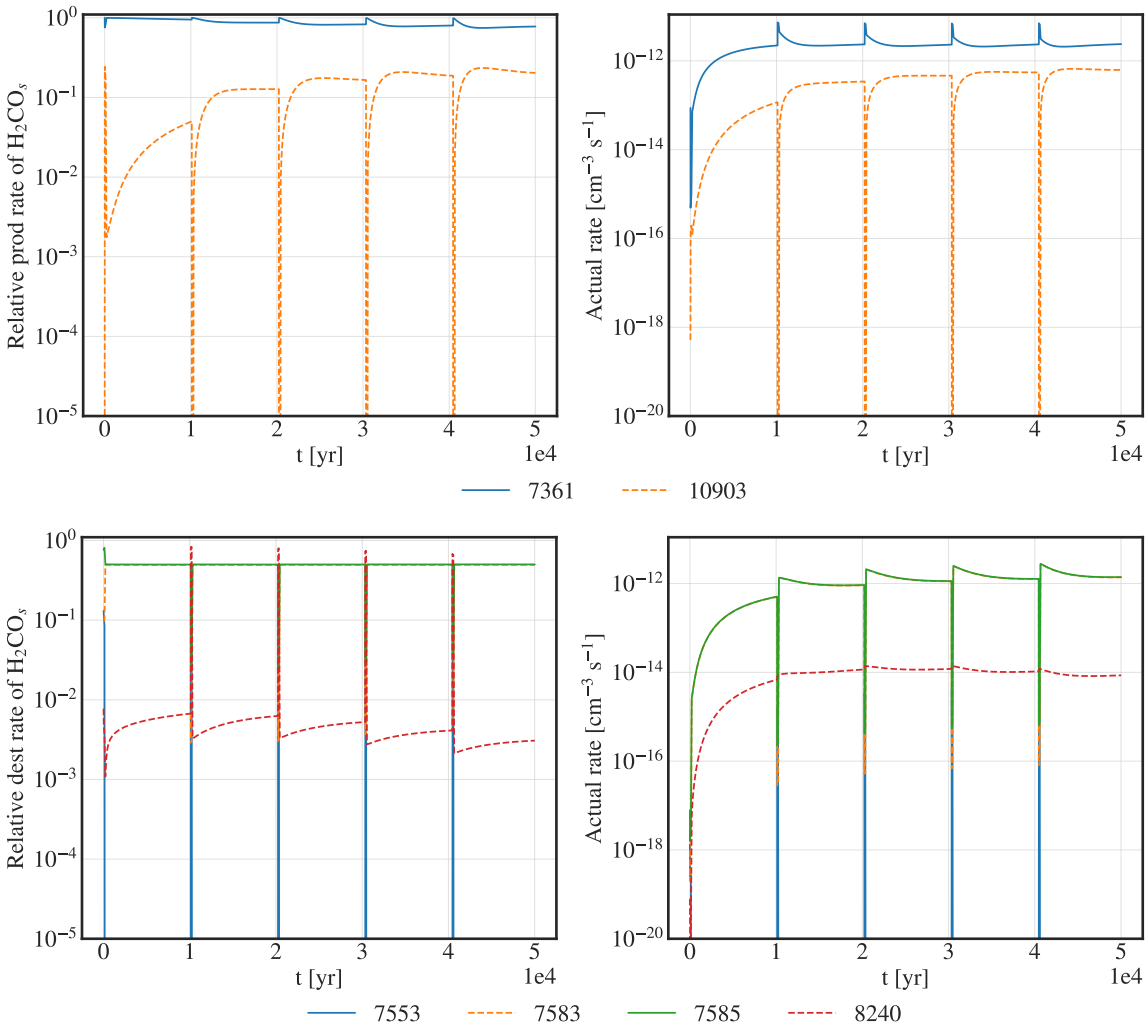

Figure 45: H_2CO_s production (**Top**) and destruction (**Bottom**) rate for $n = 10^5$ cm^{-3} and $\tau_q = 10^4$ yr.

CH_3O_s:

- 7583: H_s + H2CO_s → CH_3O_s
- 7591: O_s + CH_{3s} → CH_3O_s
- 7575: CH_{3s} + CH_3O_s → CH_3OCH_{3s}

- 7579: $H_s + CH_3O_s \rightarrow CH_3OH_s$
- 7587: $HCO_s + CH_3O_s \rightarrow HCOOCH_{3s}$
- 10903: $H_s + CH_3O_s \rightarrow H_2CO_s + H_{2s}$

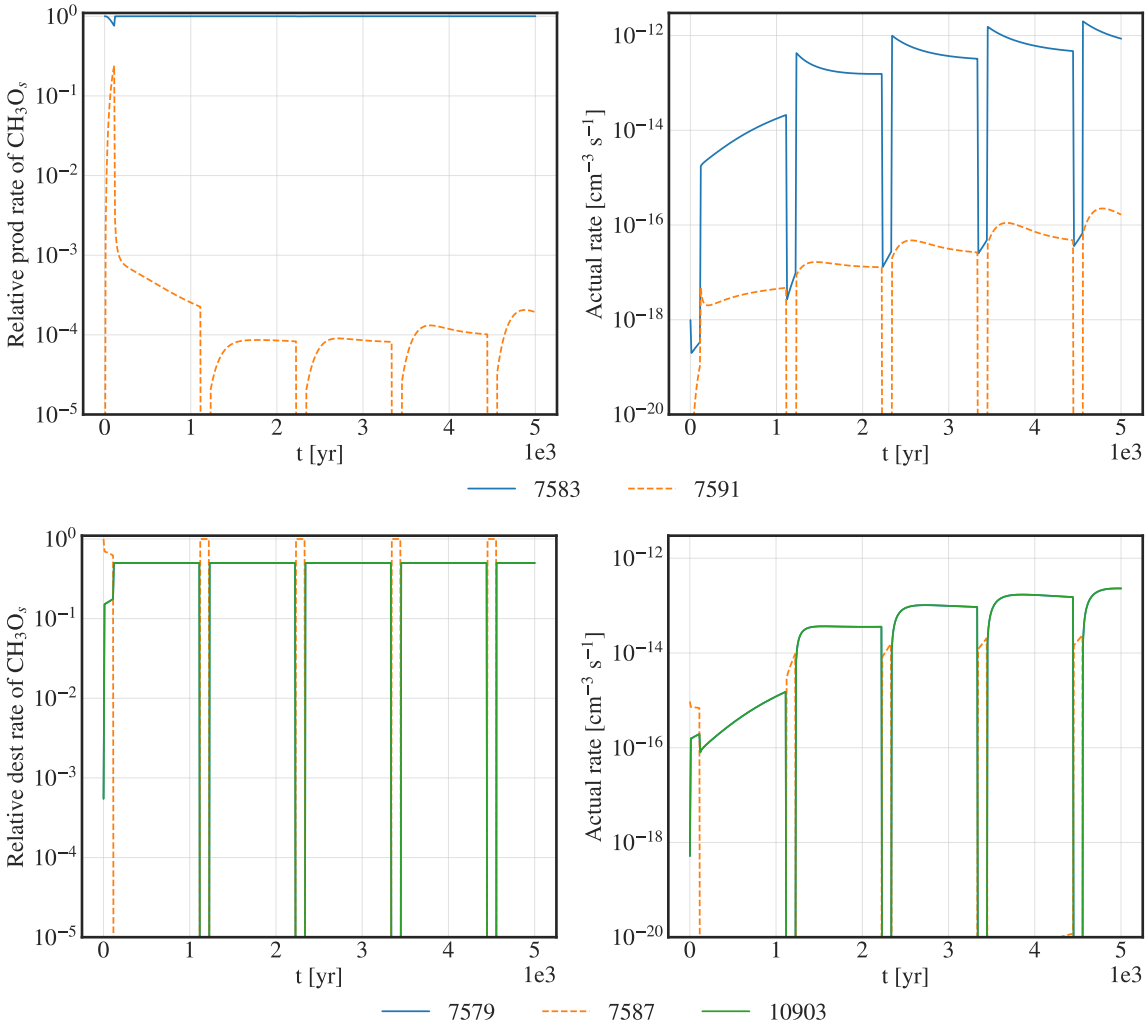

Figure 46: CH_3O_s production (**Top**) and destruction (**Bottom**) rate for $n = 10^5$ cm^{-3} and $\tau_q = 10^3$ yr.

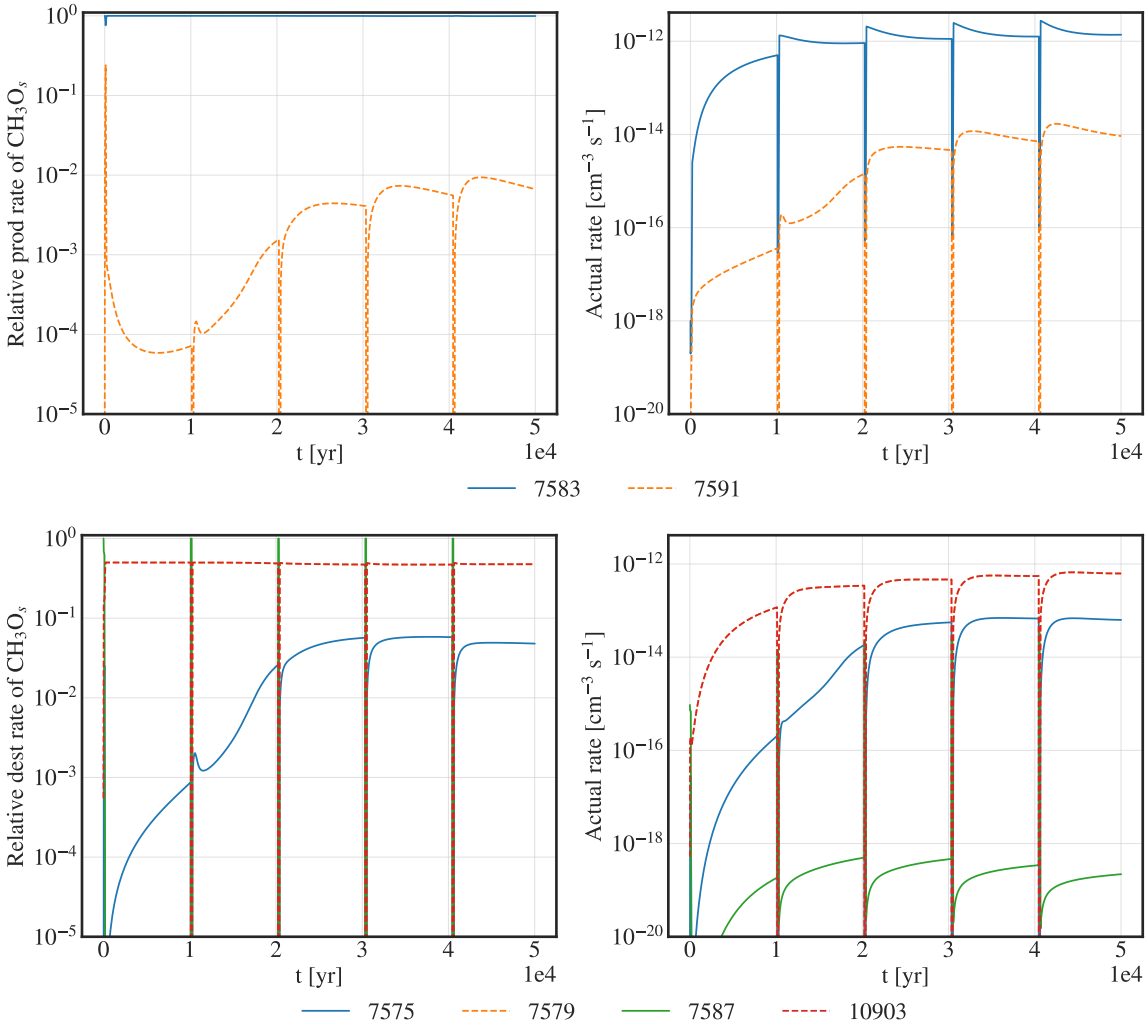

Figure 47: CH_3O_s production (**Top**) and destruction (**Bottom**) rate for $n = 10^5$ cm^{-3} and $\tau_q = 10^4$ yr.

CH_2OH_s:

- 7581: $H_s + H_2CO_s \rightarrow CH_2OH_s$
- 7593: $OH_s + CH_{2s} \rightarrow CH_2OH_s$
- 10905: $H_s + CH_3OH_s \rightarrow CH_2OH_s + H_{2s}$

- 8333: $HCOOCH_{3s} \rightarrow HCO_s + CH_2OH_s$
- 7577: $H_s + CH_2OH_s \rightarrow CH_3OH_s$
- 7670: $O_s + CH_2OH_s \rightarrow HCOOH_s + H_s$
- 10901: $H_s + CH_2OH_s \rightarrow H_2CO_s\ H_{2s}$

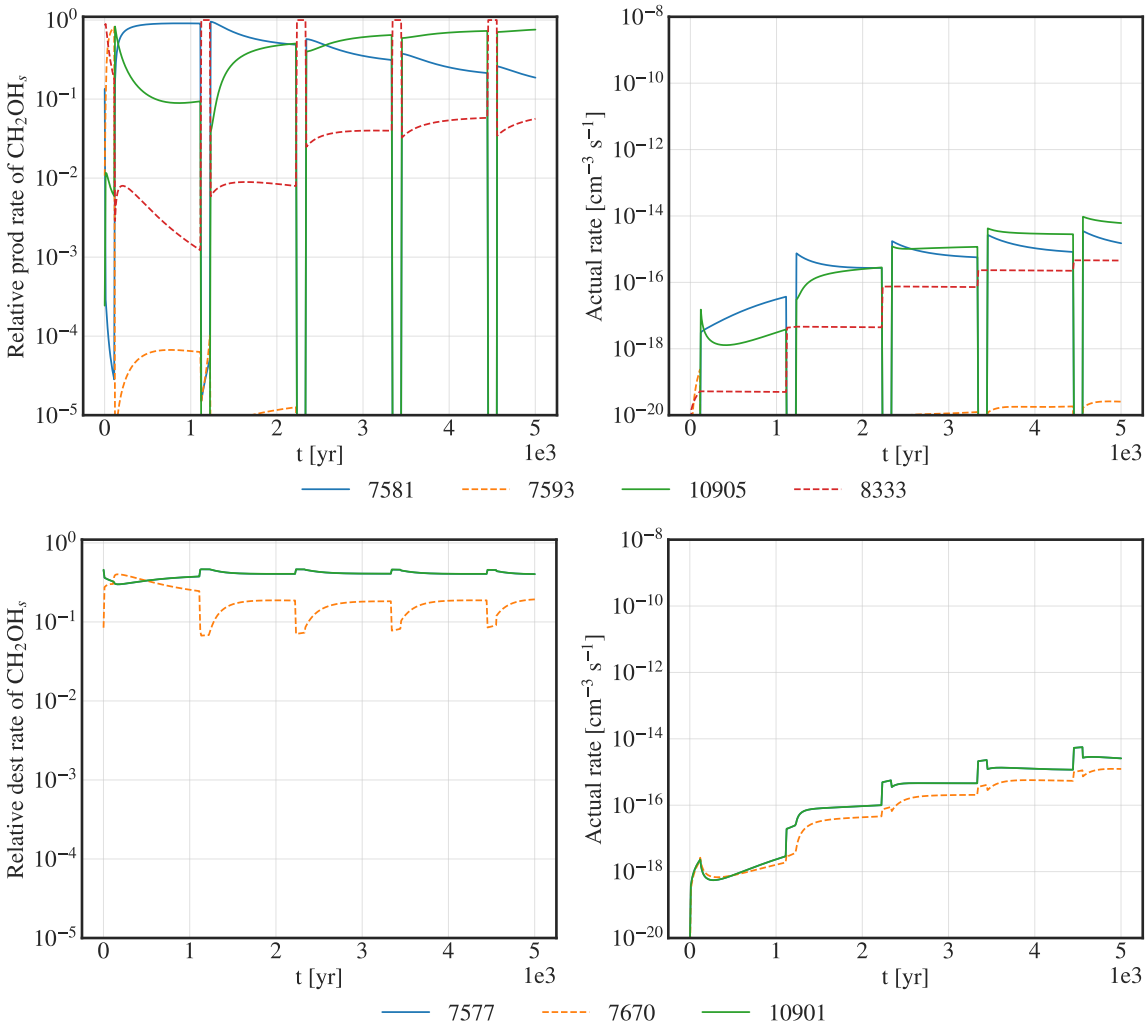

Figure 48: CH_2OH_s production (**Top**) and destruction (**Bottom**) rate for $n = 10^5$ cm^{-3} and $\tau_q = 10^3$ yr.

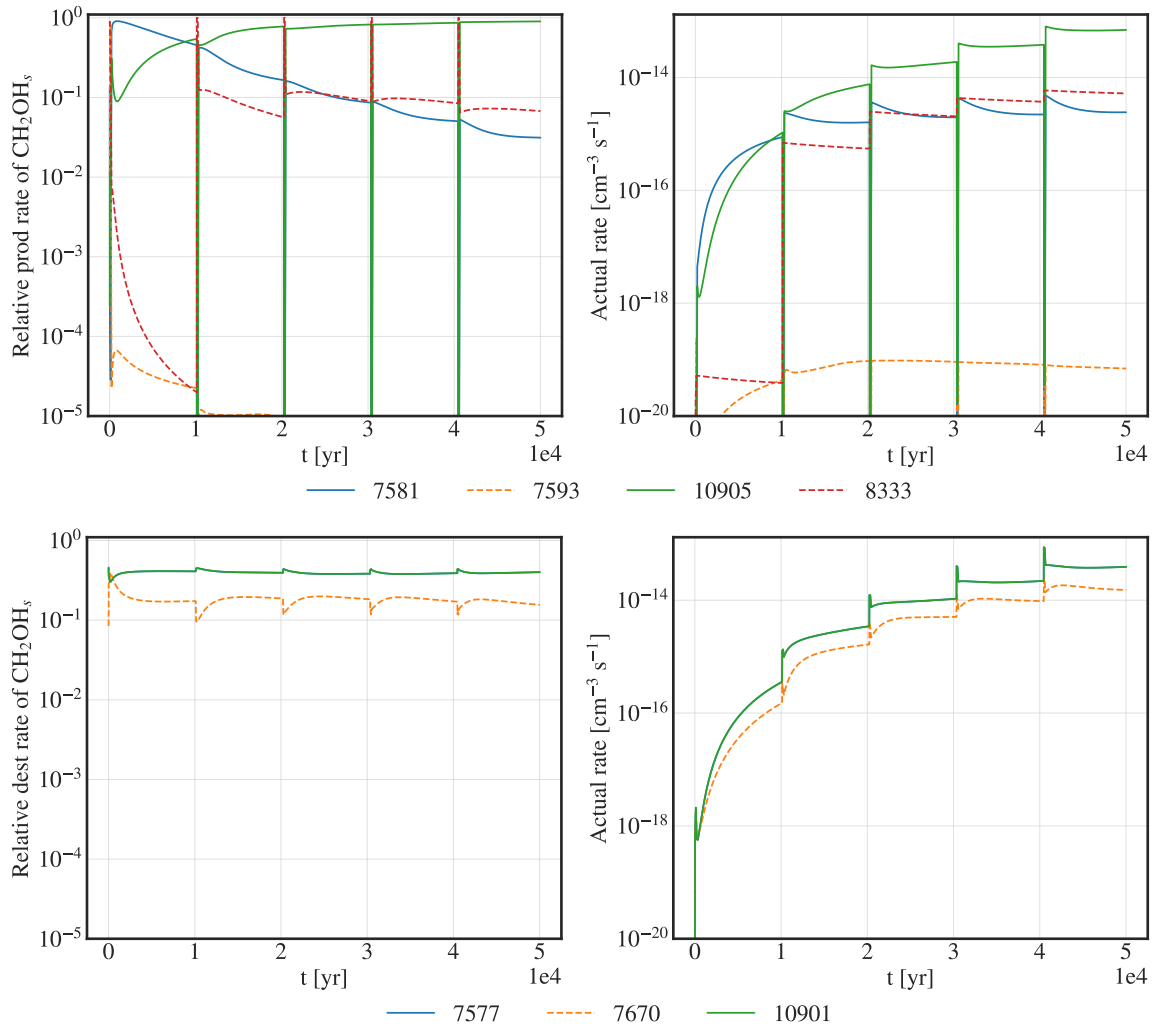

Figure 49: CH_2OH_s production (**Top**) and destruction (**Bottom**) rate for $n = 10^5$ cm^{-3} and $\tau_q = 10^4$ yr.

CH_3OH_s:

- 7577: $H_s + CH_2OH_s \rightarrow CH_3OH_s$
- 7579: $H_s + CH_3O_s \rightarrow CH_3OH_s$
- 10905: $H_s + CH_3OH_s \rightarrow CH_2OH_s + H_{2s}$
- 8228: $CH_3OH_s \rightarrow CH_{3s} + OH_s$

- 8229: $CH_3OH_s \rightarrow H_2CO_s + H_{2s}$
- 8384: $CH_3OH_s \rightarrow CH_{3s} + OH_s$
- 8385: $CH_3OH_s \rightarrow H_2CO_s + H_{2s}$

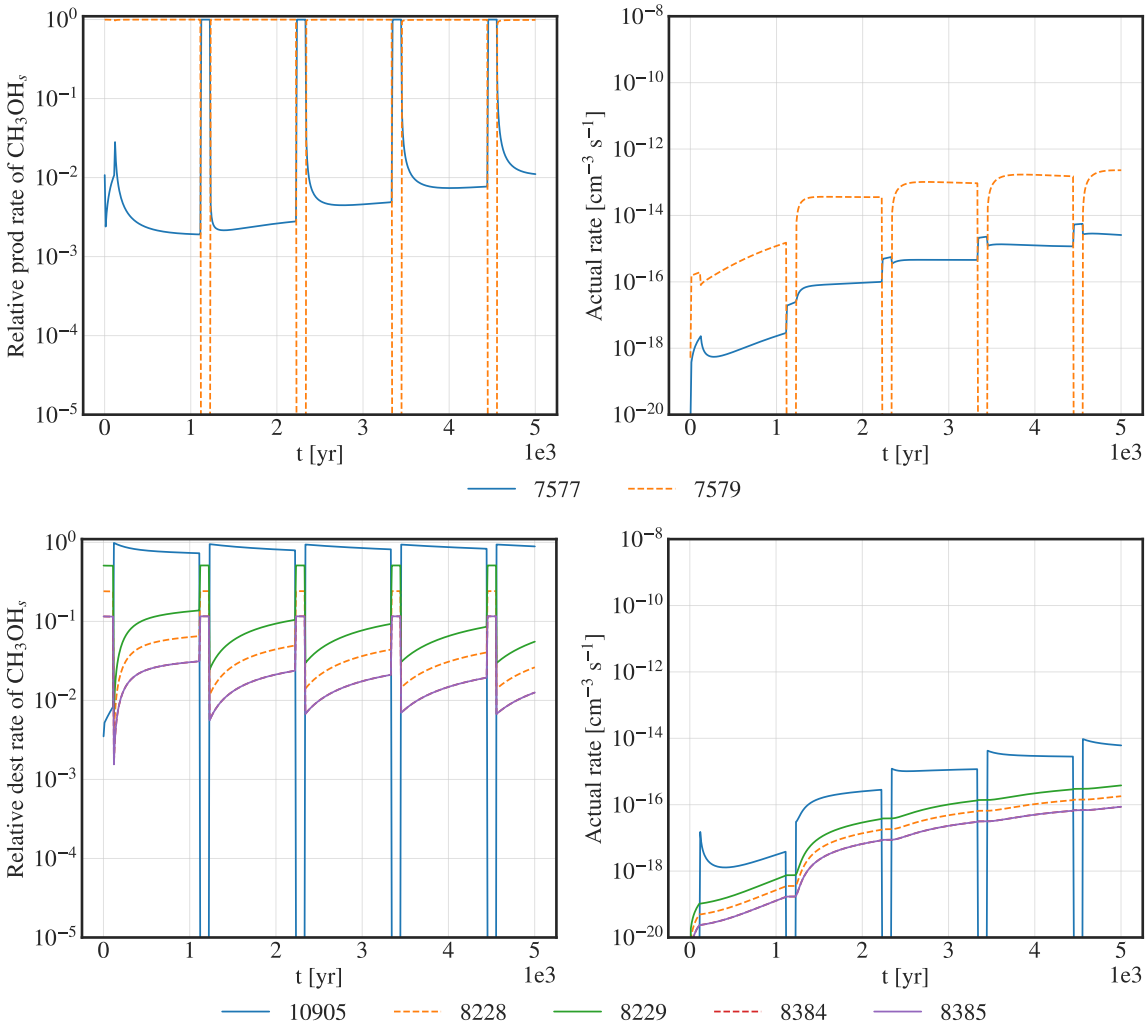

Figure 50: CH_3OH_s production (**Top**) and destruction (**Bottom**) rate for $n = 10^5$ cm^{-3} and $\tau_q = 10^3$ yr.

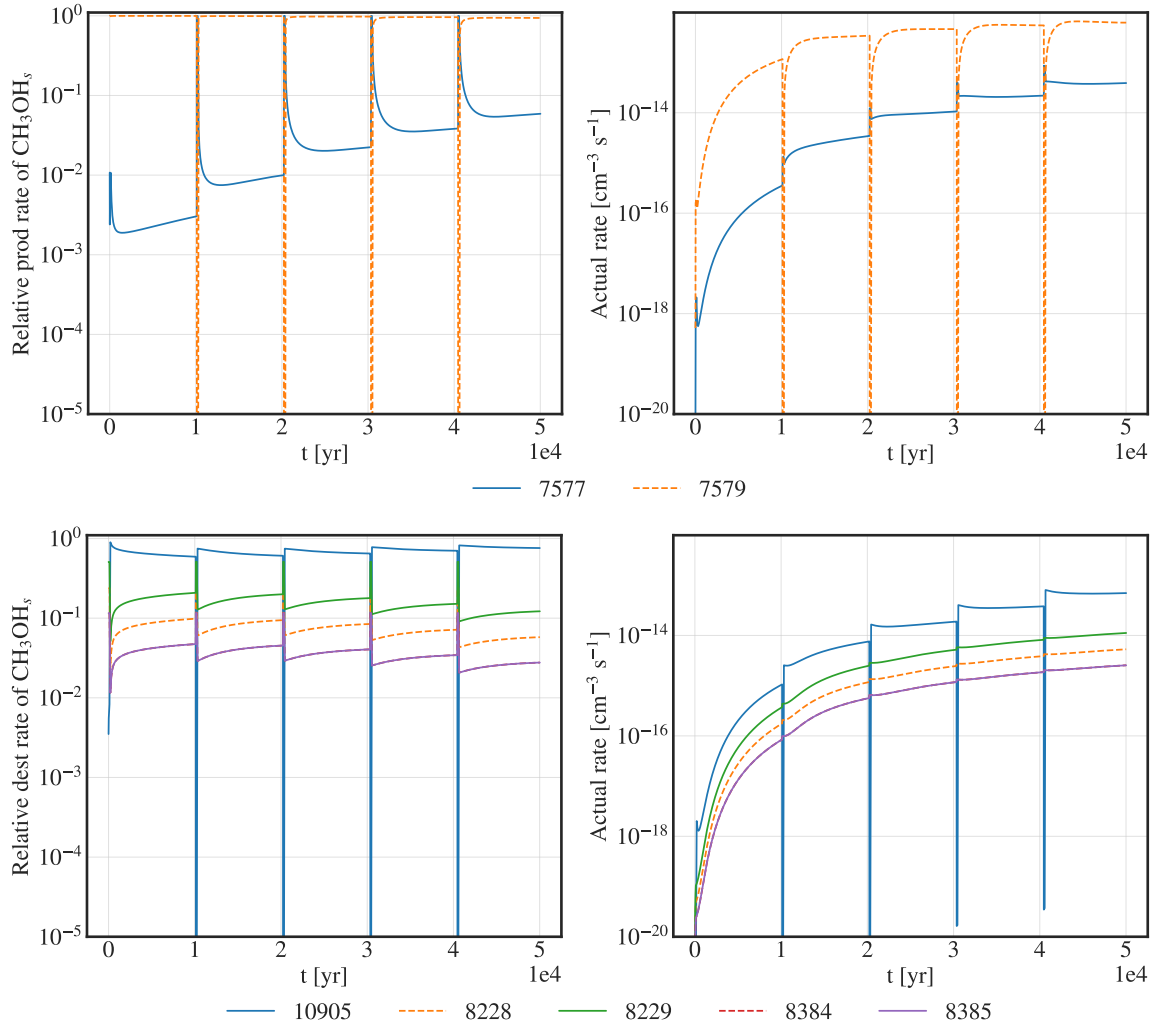

Figure 51: CH_3OH_s production (**Top**) and destruction (**Bottom**) rate for $n = 10^5$ cm^{-3} and $\tau_q = 10^4$ yr.